Mars Surface Stress Modeling

Investigation on the Crustal Structure of Mars with Finite Element Method

Weilun Qin

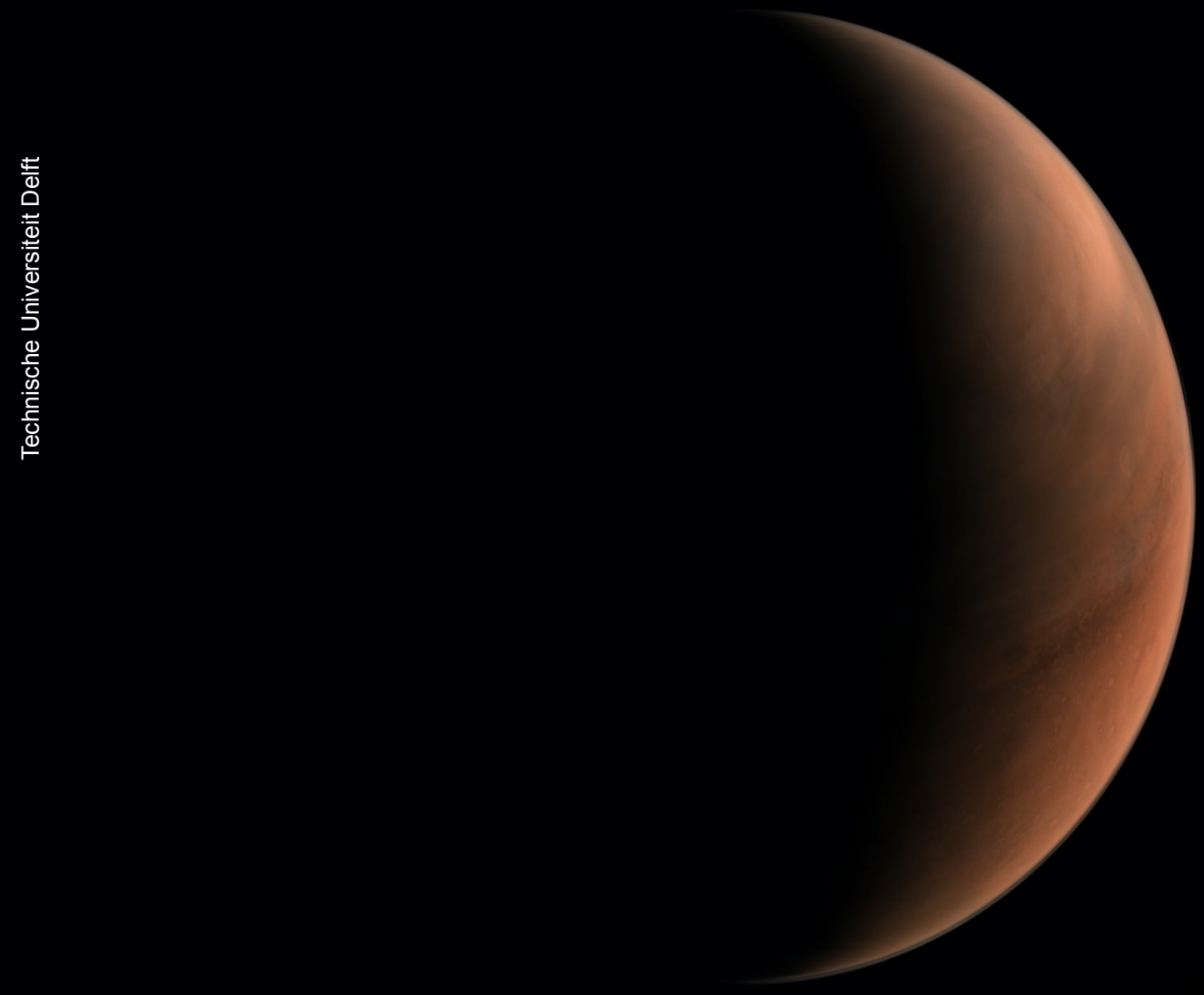

Technische Universiteit Delft

TU Delft

Mars Surface Stress Modeling

Investigation on the Crustal Structure of Mars with Finite Element Method

by

Weilun Qin

to obtain the degree of Master of Science
at the Delft University of Technology,
to be defended publicly on Monday August 23rd, 2021 at 10:00 AM.

Student number:	4931653	
Project duration:	January 1, 2021 – August 23, 2021	
Thesis committee:	Dr. ir. B. C. Root,	TU Delft, Supervisor
	Dr. ir. W. van der Wal,	TU Delft, Chair
	Dr. S. Speretta,	TU Delft

Front image: the Northern Hemisphere of Mars by Tianwen-1 orbiter (CNSA)

An electronic version of this thesis is available at http://repository.tudelft.nl/.

TU Delft

Abstract

In 2021, the interior structure of Mars is revealed for the first time with seismic data from InSight mission. The red planet is found to have a liquid core, a 500-km lithosphere, and an average crustal thickness ranges from 24 km to 72 km (Khan et al., 2021, Knapmeyer-Endrun et al., 2021, Stähler et al., 2021). Before reliable seismic measurements from the ground are available, the proper method to investigate the interior of a terrestrial planet is to study its topography and gravity. By modeling the relationship between the topography and gravity and comparing it to the observations, important information about a planet's interior structure can be learned. Stress state, which can be inferred from observed surface faults, provides more information about the formation and evolution of major features on a planet. The finite element method (FEM) can be used to compute the state of stress in the planet with a given model.

This work contributes to understand the interior of Mars by developing a new 3D flat FEM model. The performance of the FEM model is evaluated by comparing the calculated lithospheric stresses (and strains) to observed faults on the surface of Mars. To improve the accuracy of the FEM model, various crustal profiles are incorporated and the effect of a mantle plume is considered. The main research question of this study is: *What information about the subsurface crustal structure of Mars can be revealed from the surface faults?*

To obtain a realistic crustal profile for Mars, different crustal models are investigated. These models come from the theories of both classic isostasy (Airy and Pratt) and flexural isostasy (infinite plate and thin shell). In order to evaluate these crustal models, the power spectra of the spherical harmonic expansions of Martian gravity anomaly and the gravity effect of topography with different compensations are compared. For $2 \leqq n \leqq 90$, the thin shell model with an elastic thickness of the lithosphere (T_e) of 158 km fits the observation best. But the infinite plate model outperforms the thin shell model for $5 \leqq n \leqq 90$ with a T_e of 136 km. Varying the Young's modulus in the thin shell model from 100 GPa to 1 GPa changes the best-fitting T_e from 120 km to 580 km.

The 3D flat FEM Mars model is made with the commercial software package Abaqus. In order to simulate the effects of varying crustal thickness (or density) from the crustal models, a deviatoric buoyancy approach is proposed. This approach neglects the gravity in the crust and mantle, and it only considers the effects of the surface loads and the corresponding buoyancy. The boundary effect in the flat model is reduced by extending the model size. A series of simple loads, which simulate different types (positive, negative, and hybrid) of topography, have been generated to verify the performance of the FEM model.

Three regions are selected as the regions of interest: Tharsis Rise, which represents large volcanic mountains; Hellas Basin, which represents impact craters; and Utopia Basin, where both volcanic mountain and impact basins coexist. The topography of these regions is loaded into the FEM model, and the predictions from the model are compared to the observations. The stress and strain analyses for the Tharsis Rise suggest that the formation of the bulge and the surface faults are affected by both the volcanic constructed lithosphere and the dynamic support from the deep mantle plume. The plume underneath Tharsis is likely to experience a reversal from upwelling to downwelling. Such a reversal from the bottom changes the property of the surface stress and results in the current faults distribution. The Hellas Basin is found to be in isostatic equilibrium, while the Utopia Basin is not.

Although the FEM model could not explain the direction and location of all faults in the regions of interest, it gives insights into whether the target region is in isostatic equilibrium. By further including the effect of mantle plume (as done for Tharsis), it can make a more realistic prediction on the formation and evolution of target regions. The main recommendation from this study is to construct a spherical FEM model for Mars and incorporate the crustal profile in it. Future studies could also investigate the effects of spatial variations in crustal thickness and density on Mars.

Preface

This thesis marks the end of my life as a student in the faculty of Aerospace Engineering at Delft University of Technology. I came here three years ago as an exchange student. The spaceflight minor I took at that time inspired me to explore more about space. Later, the two-year Master's program in space exploration made me realize how small we (humanity) are in the universe, and yet how great we are to reach and explore places where are far beyond the distance between our footsteps. I believe the Earth would not be the only harbor for humanity, and we will set foot on the Moon and Mars in the foreseeable future. I spend my time and effects in this thesis to contribute to our understanding of Mars.

I was very lucky to meet Bart Root and had him as my daily supervisor. He guided me throughout the whole thesis and provided a huge support. I am always looking forward to discussing my results with him during our weekly meeting. I would like to show my appreciations to Jesse, Youandi, Joana, and Bodjie who read my draft thesis and provided constructive feedback for me. It's so nice to work with people sharing the same passions. I would also like to thank all fellow students: Emilie, Gèmo and Joël from the Master online thesis supporting team, and Aaron, Marijn, Maxime, Nynke, Stan and Vivian from the Planetary Interior and Gravity Modeling group. Your accompany made this journey wonderful. Lastly, I would like to express gratitude to my family and friends. Especially my parents who provide unconditional support and love. Hope to see you soon!

Weilun Qin
Delft, August 2021

Contents

List of Figures

List of Tables

Nomenclatures

Greeks Symbols

Symbol	*Description*	*Units*
ϵ	Strain	–
γ	Shear strain	–
λ	Wavelength	m
μ	Gravitational parameter	m^3/s^2
ν	Poisson's ratio	–
Φ	Flexural response function	–
ϕ	Longitude	°
ρ	Density	kg/m^3
ρ_c	Density of the crust	kg/m^3
ρ_m	Density of the mantle	kg/m^3
ρ_0	Mean density	kg/m^3
σ	Stress	Pa
σ^2	Power spectrum (or degree variance)	–
τ	Shear stress	Pa
θ	Colatitude	°
θ_P	Angle of the principal plane	°

Roman Symbols

Symbol	*Description*	*Units*
C_{nm}	Spherical harmonic coefficients	–
D	Flexural rigidity	$N \cdot m^2$
D_c	Depth of compensation	km
dP	Deviatoric buoyancy	Pa
E	Young's Modulus	Pa
G	Gravitational constant	$m^3/kg/s^2$
g	Gravitational acceleration	m/s^2
g_B	Bouguer gravity anomaly	m/s^2
g_F	Free air anomaly	m/s^2
g_r	Radial component of the gravitational field	m/s^2
h	Height	m
M	Mass	kg
m	Spherical harmonic order	–
n	Spherical harmonic degree	–
p	Loading pressure	Pa
R	Radius of a planet	km
r	Radius of a thin shell	km
r	Root of compensation in Airy's isostasy	m
S_{nm}	Spherical harmonic coefficients	–
T_c	Crustal thickness	km
T_e	Effective elastic thickness of the lithosphere	km
u	Displacement or deflection	m
w	Displacement or deflection	m

Abbreviations

CAD	Computer-Aided Design
CAE	Complete Abaqus Environment
FAA	Free-Air Anomaly
FEM	Finite Element Method
GMM-3	Goddard Mars Model-3
GSHA	Global Spherical Harmonic Analysis
GSHS	Global Spherical Harmonic Synthesis
HDB	High Degree Band
LDB	Low Degree Band
LDP	Large-Dual-Positive
MGS	Mars Global Surveyor
MODY	Mars Odyssey
MOLA	Mars Orbiter Laser Altimeter
MRO	Mars Reconnaissance Orbiter
NASA	National Aeronautics and Space Administration
PDS	Planetary Data System
PN	Positive and Negative
RET	Rock Equivalent Topography
RMS	Root Mean Square

1 Introduction

Mars, the “Red Planet”, is the fourth inner planet in the solar system. As a neighbour of the Earth, Mars is also a terrestrial planet but with a much thinner atmosphere. It has a mean radius of about 3389.5 km (Seidelmann et al., 2002), which is about half of the size of the Earth. Mars is similar to the Earth in terms of the tilt of the rotational spin axis and rotational period (Laskar et al., 2004), which result in comparable daily and seasonal features to Earth. The red planet has been a destination for space exploration not only because it is close and similar to Earth, but also for scientific goals like searching for life and preparing for human exploration[1]. Another important scientific aim is to discover the subsurface and evolution of the planet.

In this thesis, a completed introduction consists of both chapter 1 and chapter 2. This chapter only provides a brief introduction on Mars (section 1.1) and literature reviews (section 1.2) about the interior structure modeling of Mars as well as stress state estimation. The research questions (section 1.3) are presented at the end of this chapter. Detailed introductions of topography, gravity, faults and stresses can be found in chapter 2.

1.1. Mars and Its History

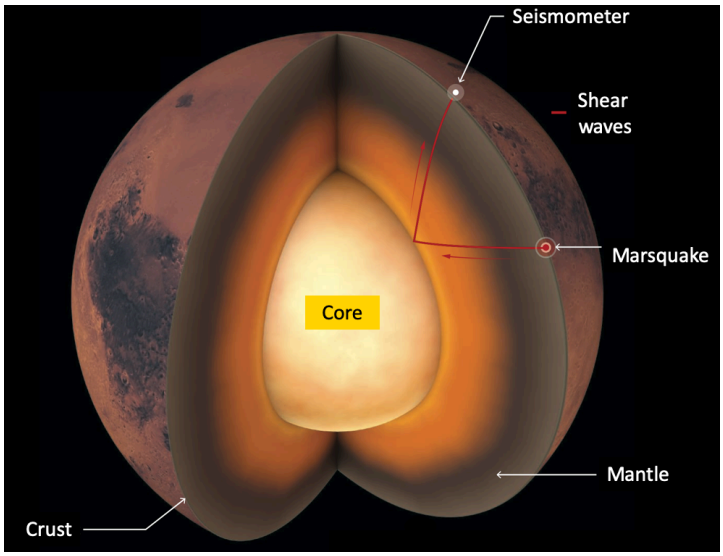

Figure 1.1: Impression of the interior of Mars (Cottaar and Koelemeijer, 2021). Mars differentiated into crust, mantle and core. Shear waves induced by a marsquake can reflect on the boundary of the core and be detected by the seismometer.

[1] https://www.esa.int/Science_Exploration/Human_and_Robotic_Exploration/Exploration/Why_go_to_Mars [15-01-2021]

The interior of Mars can be divided into three layers: the crust, the mantle, and the core. Recent studies have revealed the interior structure of Mars with seismic observations from the InSight mission. The average crustal thickness for Mars is estimated between 24 km and 72 km (Knapmeyer-Endrun et al., 2021). The lithospheric thickness is found to be around 500 km (Khan et al., 2021), and the core of Mars is discovered to be liquid with a radius of about 1830 km (Stähler et al., 2021).

Figure 1.1 shows a impression of the interior of Mars. The crust is an outer thin shell wrapping around the planet. Underneath the crust is the thick mantle. The lithosphere consists of the crust and the uppermost mantle. The liquid metal core lies deep down into the red planet. A path of the shear waves is highlighted in Figure 1.1. The shear waves origin from a Marsquake, bounce at the core-mantle boundary, and propagate to the site of the seismometer.

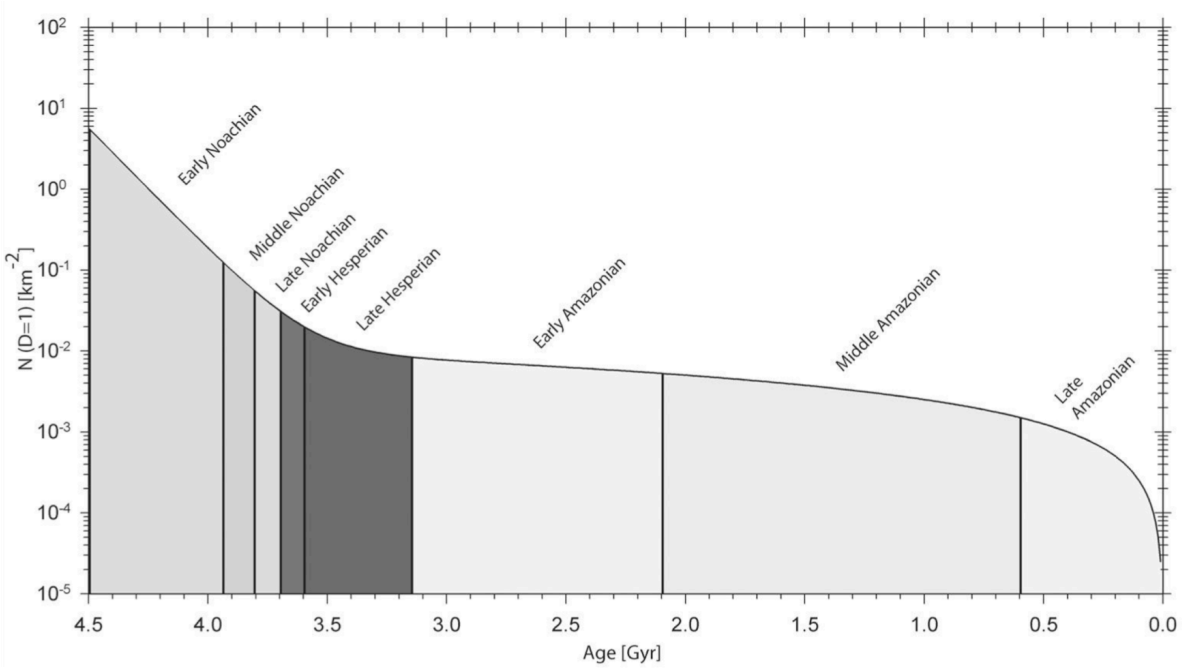

Figure 1.2: Martian cratering chronology model with main Martian eras indicated (Rossi and Gasselt, 2010). N stands for number of impact craters per square kilometers. 1 Gyr = 10^9 years.

The geological history of Mars can be separated into four periods (Carr and Head, 2010, Rossi and Gasselt, 2010): the pre-Noachian (4.6 to 4.1 Gyr), the Noachian (4.1 to 3.7 Gyr), the Hesperian (3.7 to 3.0 Gyr), and the Amazonian (3.0 Gyr to present). Figure 1.2 presents the number of impact craters (radius larger than 1 km) per square kilometers as a function of geological age. The Noachian period is featured with high cratering rates. The speed of the crater formation became stable from the middle of Hesperian period (around 3.5 Gyr) to the end of middle Amazonian period (1 Gyr). The major features on the surface of Mars (as shown in Figure 2.1) were formed in the early stage (before 3.5 Gyr). For instance, the global dichotomy is estimated to form in the pre-Noachian, and the formation of Hellas Basin marked the beginning of the Noachian period. It is also during the Noachian period that most of Tharsis region began to form (Carr and Head, 2010).

1.2. Modeling Mars

Mars has a long geological history (4.6 Gyr). But the exploration of Mars by human-made spacecraft only started over half a century ago. This means that humanity only has close observations on Mars for less than $\frac{1}{90{,}000{,}000}$ of the planet's history. In other words, assuming the total age of Mars is 100 years, the spacecraft only have observed the planet for the last 35 seconds.

With this "35-second" snapshot of Mars, scientists have built different models to simulate Mars. The interior of Mars can be most effectively investigated by seismic measurements. But the data from InSight mission are only available since 2019. Before that, the interior of Mars has been investigated by studying the relationship between the data of topography and gravity. This section reviews how

the interior of Mars was modeled and how the stress state was calculated from other literature. The methodologies used in this study are elaborated in chapter 3 and chapter 4.

1.2.1. Interior Structure

With topography and gravity data, information about the lithosphere (crust and uppermost mantle) of Mars can be revealed. Generally, this can be done by establishing crustal models first. Then, by comparing the modeled relationship (e.g., admittance) between gravity and topography to the observation, geophysical parameters of the lithosphere (e.g., crustal thickness, crustal density, and mantle density) can be derived (Wieczorek, 2015).

Gravitational admittance is a parameter to link topography and gravity data. It is the ratio between gravity anomaly and Fourier transformed topography (Watts, 2001). To calculate admittance, geophysical models which can estimate the gravity anomaly from topography are needed. Since the gravity anomaly depends on parameters like lithospheric thickness, mantle density and crustal density, a realistic estimation of these parameters can be obtained by varying the values of these parameters and finding the best fit admittance. Watts (2001) shows the calculated admittance from different models of isostasy globally. A global admittance study for a planet reveals the characteristic of its lithosphere straightforwardly, but detailed information might be neglected.

For a planet like Mars whose surface is dominated by different topographic features, localized analysis of a certain region may bring more accurate results than a rough global analysis. McGovern et al. (2002) proposed a spherical shell flexure model of the Martian lithosphere considering both surface and subsurface loads. Using the spatial-spectral localization method developed by Simons et al. (1997), they obtained the gravity/topography admittance for several volcanic regions. Estimations of the lithosphere thickness were derived and converted into heat flow to reveal more information about the planet's interior. However, an inconsistency in the use of Martian radius was pointed out by Belleguic et al. (2004), which led to some corrections of original work in a later paper (McGovern et al., 2004).

To investigate the localized admittance of the gravity and topography fields around major Martian volcanoes, Belleguic et al. (2005) used a numerical method with flexure models and a spectral localization algorithm proposed by Wieczorek and Simons (2005). The densities and elastic thickness of major volcanoes, as well as the crustal density, were constrained by Belleguic et al. (2005). They further modeled the subsurface loads and concluded that the load under the Elysium rise and Arisa Mons was more likely to be a mantle plume, which indicated recent volcanism in those areas.

Beuthe et al. (2012) investigated the crustal density and elastic thickness in the Tharsis region by localized admittance study on gravity data from Mars Express and Mars Reconnaissance Orbiter (MRO). The authors predicted the gravity signal in flexural lithosphere models with two loading techniques: one was a common top/bottom loading method, and the other was a new top/top model with loading history. The density and elastic thickness for major volcanoes around the Tharsis province as well as Elysium and Alba Mons have been estimated. But the constraints on the elastic thickness does not improve with better (lower wavelength) gravity data. The reason might be that the gravity signal loses sensitivity on lithosphere thickness as the wavelength decreases.

Instead of directly modeling the relationship between gravity and topography, Watts and Moore (2017) modeled the gravity effects of the topography with different isostatic models and compared the power spectra of outcomes to the observed gravity anomaly. By doing so, Watts and Moore avoided the use of admittance and made the results easier to interpret under geophysical context. In this study, the approach by Watts and Moore (2017) is applied to Mars to find the more realistic crustal models.

1.2.2. Stress State

The stress state in the lithosphere of Mars contains information about tectonics, volcanism, mantle convection, and heat flow (Tenzer et al., 2015), which contributes to the understanding of current state and evolution of Mars. On the surface of Mars, a large number of faults have been observed. The state of the stress which induces a surface fault can be retrieved by examining the direction of the displacement on the fault (Turcotte and Schubert, 2014). The relationship between surface faults and stresses are discussed in chapter 2. The stress modeling is elaborated in chapter 4. This subsection reviews how stress state is modeled by other studies.

The stress state in the lithosphere of Mars can be computed analytically from a thin shell model. The equations to calculate lithospheric stress in thin elastic shell models were derived by Beuthe (2008).

With these equations, it is convenient to construct the stress maps. However, the analytical solution is only valid for a homogeneous thin shell model, which is not a good representation of the reality. To solve the general equations from models with variable thickness, numerical methods are needed.

Numerical approaches like Finite Element Method (FEM) can also calculate the state of stress in the lithosphere. Wu (2004) discussed how to apply commercial FEM software for geophysical problems. Since commercial FEM tools solve the stiffness equation, Wu proposed to modify the stiffness equation and add the terms of isostatic restoring force and self- gravitation. Such modifications as well as related boundary conditions were applied for a flat Earth model without self-gravitation and a spherical earth model with self-gravitation in Wu's paper. Wu emphasized that the output from FEM model should be post-processed before it can be used for interpretation.

Spherical, compressive, self-gravitating and viscoelastic Earth models were built by Wang et al. (2008). Even though these models (Wang et al., 2008) were designed for Earth, Blank (2015) managed to adapt them for Mars and obtain the strain field of Mars from FEM program's output. Blank (2015) showed that commercial FEM packages discussed by Wu (2004) can be used for computing the state of stress and strain for the lithosphere of Mars.

Other techniques are also used to compute the stress state on Mars. Tenzer et al. (2015) used a flexural isostatic model based on a thin plate to estimate the sub-crustal stress and solved the Vening Meinesz-Moritz inverse problem of isostasy to determine the crustal thickness of Mars. They concluded that Martian sub-surface stress was caused by crustal loadings and volcanism-related regional tectonism instead of active global tectonics.

Non-hydrostatic stress states in the Martian interior were calculated by Batov et al. (2019) with different rheological models to investigate the zones with high seismic activity on Mars. Two major types of models were used by Batov's group: one was a flexural lithosphere model and the other one was with extra melting domains. They computed the non-hydrostatic stress by summing up the initial, hydrostatic and additional stresses. Significant shear and tensional stresses were found in regions like Hellas Planitia, Argyre Planitia, Mare Acidalia, Arcadia Planitia plain and Valles Marineris. These places were assumed to be possible sources of marsquakes.

In this study, the FEM will be used to compute the stress state in the lithosphere of Mars. The surface faults on Mars are used to check the calculated stress.

1.3. Research Questions

Previous sections suggest that the interior of Mars can be investigated with topography and gravity data, and additional observations on faults reveal more information about stress state on Mars. FEM can be used to bridge these two parts by building a Mars model with interior structure and calculating the stress state in it. Thus, the research question for this study is formulated as

What information about the subsurface crustal structure of Mars can be revealed from the surface faults?

To answer the research question, the following sub-questions are derived:

1. *What are the existing realistic crustal models for Mars?*
   (a) What are the basic and advanced crustal models from the literature?
   (b) How to implement the selected crustal models in Matlab/Python?
   (c) What would be the effect of applying different crustal models on the results of surface stress?
   (d) What would be the effect of varying model parameters (e.g., lithospheric thickness, crustal density, mantle density, and Young's modulus) on the results of surface stress?
2. *How to compute the surface stress state on Mars with FEM?*
   (a) Which FEM software packages are suitable for this project?
   (b) Are there any existing FEM models for Mars? If there are, how to improve these models? If not, how to create one?
   (c) How to incorporate different crustal models into the Mars FEM models?
   (d) How to extract the state of lithospheric stress from the output of FEM?

3. *How to analyze the relationship between surface faults and subsurface crustal structure on Mars?*
   (a) What is the relationship between crustal structure and the state of stress in the lithosphere?
   (b) What is the relationship between surface faults and lithospheric stress state on Mars?
   (c) Would the computed stress state have a better fitting for the younger faults?

Based on the main research question and followed sub-questions, this thesis can be divided into three parts (as shown in Figure 1.3): firstly, studying different crustal models for Mars; secondly, implementing different crustal models into the FEM models for Mars and calculating the stress state of lithosphere; lastly, comparing the modeled stress state and observed faults on the surface of Mars.

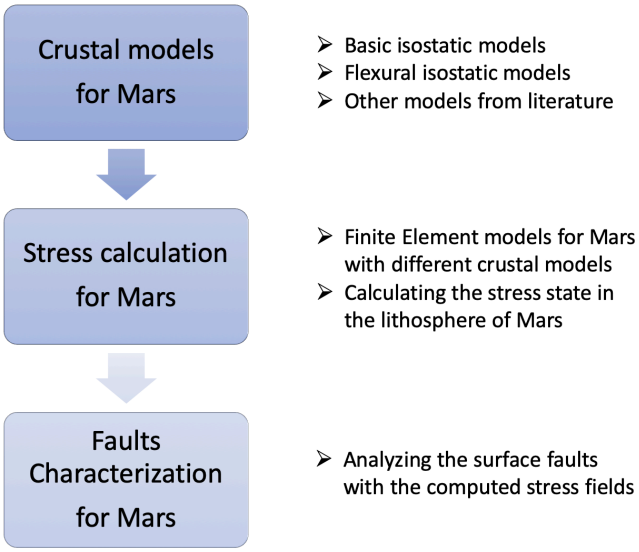

Figure 1.3: The main work packages for this thesis.

The following chapter 2 serves as an additional introduction where the data (topography, gravity and faults) used in this study are introduced. Readers can find more background information on the red planet from chapter 2. After the introduction from both chapter 1 and chapter 2, methodologies are presented in chapter 3 and chapter 4. The investigation on the subsurface crustal structure of Mars is discussed in chapter 3. The construction of the FEM model, as well as the incorporation of the crustal models into the FEM model, is elaborated in chapter 4. Verification and validation on the methodologies are presented in chapter 5. Results, discussion, conclusion, and recommendation can be found in chapter 6, chapter 7, chapter 8, and chapter 9, respectively.

2

Observations of Mars

Mars has been a target for space exploration for decades. In the pre-spacecraft age, information of Mars was obtained by naked-eye and telescopes. Observation of the Red Planet by naked-eye could only reveal information about its position and motion. Surface details of Mars were visible when telescopes came into use in the observation. Italian astronomer Galileo Galilei was the first person who viewed the planet with a telescope back in 1610 (Peters, 1984). The first map of Mars where Syrtis Major Planum was correctly shown (Moore, 1984) was drawn by Dutch astronomer Christiaan Huygens in 1659. Telescope observations yielded more information about Mars like the rotation period and axial tilt (William, 1996).

The second period of Mars exploration began in the 1960s with robotic spacecraft. The goals of early flyby missions in the 1960s were to approach Mars, conduct close measurement and image the Martian surface at close distance (Snyder and Moroz, 1992). Later orbiter, lander and rover missions aimed to take more images, conduct more detailed measurements and experiments for the planet. The US Mariner 4 first completed the flyby mission to Mars in 1965 and sent back the first images of the Martian surface (Nicks, 1967). On 14 November 1971, Mariner 9 arrived at Mars and entered the orbit, making it the first orbiter of Mars. The title of the first lander of Mars goes to Soviet Mars 3 lander which had a soft-land on Mars in December 1971. After decades of unmanned spacecraft mission to Mars, the next period of Mars exploration is aim to pave the way for future human exploration (Rossi and Gasselt, 2010).

This chapter presents important observations (topography, gravity and faults) of Mars in the ”35-second snapshot”. Topography, which described the surface feature, is introduced firstly. Secondly, the gravity of Mars in presented, which contains information about mass distribution on Mars. Thirdly, the observed faults and stresses are discussed. This chapter aims to provide more background information for readers.

2.1. Topography

The topography of Mars has been mapped by different approaches. During the Martian oppositions in the 1970s and early 1980s, earth-based radar measurements were used to retrieve topography information on parts of Mars (Downs et al., 1982). Since those observations from Earth were conducted during Martian oppositions, the radar ranging data only covered the area within $\pm 23°$ around the equator. The topography models covering a larger surface area were developed with data from several Mars missions. For example, radio occultation measurements from Mariner 9 and Viking orbiters were used to estimate the topography by Cain et al. (1972) and Lindal et al. (1979) separately. Images from the Viking mission were used by Wu et al. (1984) to derive the topographic information with stereoscopic viewing techniques. But these Martian topography models were limited by spatial extend or large uncertainty. Errors of these models were about 1 to 3 km in the vertical direction (Smith et al., 1999).

To obtain high-quality global measurements of the Martian topography, the Mars Orbiter Laser Altimeter (MOLA) was sent to Mars onboard Mars Global Surveyor (MGS) in 1996. Four-year measurements (from 1997 to 2001) of MOLA contributed to topography models whose average accuracy was

better than 1 m with respect to the planet's center of mass (Neumann et al., 2001).

In this study, the global topographic maps from MOLA are used. The data can be downloaded from the website of NASA Planetary Data System (PDS) Geosciences Node[1] and has the map resolution from 4 to 128 pixels per degree globally. Both the planetary radius and areoid[2] maps can be found on the above-mentioned website. And the topography is calculated as the difference between the planetary radius and the areoid.

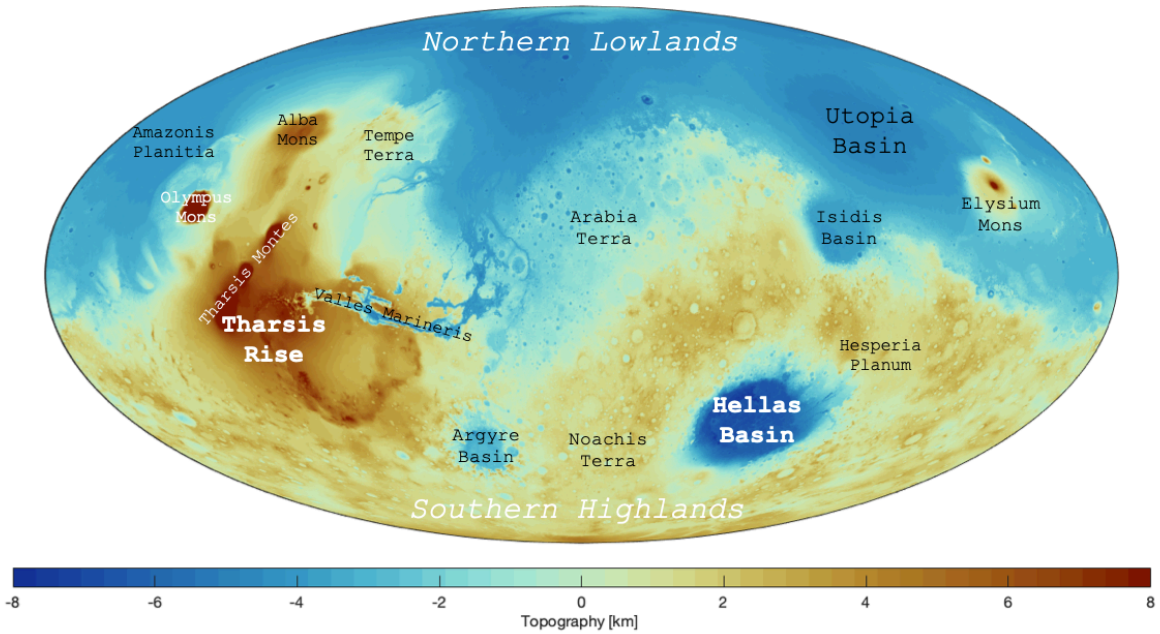

Figure 2.1: Topography of Mars with data from MOLA. The range of the colorbar is limited to ± 8 km in order to show the global topographic features. The map is presented using a Mollweide projection with a central meridian of 0° longitude. Major topographic features are labeled.

The topography of Mars from MOLA is shown in Figure 2.1. The most prominent features of Martian topography are the hemispheric dichotomy, the Tharsis bulge and the Hellas basin. The hemisphere dichotomy describes the large differences (about 5 km) in elevation between the Northern and Southern hemispheres (Smith et al., 1999). This phenomenon is also referred to as crustal or global dichotomy. It is shown in Figure 2.1 that the Northern hemisphere is dominated by lower topographic values (below zero km) while the mean height of the Southern hemisphere is more above zero km. Generally, the age of the surface can be approximated by counting the number of impact craters per unit area (Tanaka, 1986). The fact that the surface in the north is more lightly cratered suggests that the Northern hemisphere is younger than the Southern. The smoother Northern hemisphere was likely to be resurfaced by volcanism in the late Noachian-early Hesperian time period (Robinson, 1995).

Tharsis bulge, which is also called Tharsis rise, refers to the high-elevation region which is centered at 100° W longitude near the equator. The area is characterized by Olympus Mons and the Tharsis Montes. With a height of nearly 22 km, Olympus Mons is the highest volcano on Mars and currently the second tallest mountain in the Solar System (next to Rheasilvia on Vesta). Tharsis Montes is located to the left of the centre of this region where three large shield volcanoes aligned: Arsia Mons, Pavonis Mons and Ascraeus Mons. The formation of Tharsis bulge was largely due to volcanism and related tectonic processes (Williams et al., 2008). Huge shield volcanoes in Tharsis region are thought to be linked with hot superplume from the deep mantle of Mars (Yuen et al., 2007), which is similar to the hotspot under the Hawaii island on the Earth. The geological features in Tharsis are quite complex and are found to be populated by diverse structures in different time and space scales (Beuthe et al., 2012).

The Hellas basin is the huge impact basin in the Southern hemisphere. It is seen as a large blueish circle surrounded by greenish rings in Figure 2.1. Hellas Planitia has a radius of about 1150 km and

[1] https://pds-geosciences.wustl.edu/missions/mgs/mola.html [07-01-2021]
[2] A gravitational and rotational equipotential surface of Mars, analogous to "geoid" for Earth.

was likely formed during the Late Heavy Bombardment period (late Pre-Noachian and early-Noachian period) (Schultz and Frey, 1990).

2.2. Gravity

This section covers the gravity data of Mars together with the spherical harmonics toolbox to process the data. In addition, some gravitational reductions are conducted to obtain the gravity anomalies.

2.2.1. Data and Tools

Martian global gravity data has been gathered in the second Mars exploration period (since the 1960s) from different spacecraft including Mariner 9, Viking 1, Viking 2, MGS, Mars Odyssey (MODY)[3] and MRO[4]. The last three missions largely contributed to the Martian gravity solutions as they orbited Mars at close distance (Wieczorek, 2015). The early orbit for MGS was highly elliptical, and the altitude at the periapsis was just 170 km. MODY also obtained part of the tracking data from altitudes around 200 km. But later in the missions, their orbits were circularized into near-circular orbits around 400 km.

With radio-tracking data from MGS, MODY and MRO, Konopliv et al. (2011) obtained a global gravity solution (JGMRO 110C) up to degree and order 110. Later in 2016, a higher resolution gravity solution was created by Genova et al. (2016). This dataset is called the Goddard Mars Model-3 (GMM-3) and is presented in spherical harmonics up to degree and order 120. GMM-3, together with other gravity models of Mars, can be downloaded from NASA PDS Geosciences Node [5].

In the above gravity models, gravity data is presented in the form of spherical harmonics coefficients C_{nm} (also known as Stokes coefficients). Given the coefficients C_{nm} for degree n and order m, gravitational constant G, total mass of the body M and the reference radius R_0, one can derive the gravitational potential with (Wieczorek, 2015)

$$U(\mathbf{r}) = \frac{GM}{r} \sum_{n=0}^{\infty} \sum_{m=-n}^{n} \left(\frac{R_0}{r}\right)^n C_{nm} Y_{nm}(\theta, \phi) \tag{2.1}$$

where θ and ϕ are the planetocentric colatitude and longitude at position $\mathbf{r}$ on the sphere, respectively. $Y_{nm}(\theta, \phi)$ is the spherical harmonic function for degree n and order m, which is expressed in Equation A.7. The coefficients with negative order $C_{n,-m}$ are referred to as S_{nm}.

The radial component of the gravitational field g_r can be calculated from Equation 2.1 by taking the first radial derivative, which is given by (Wieczorek, 2015)

$$g_r = \frac{GM}{r^2} \sum_{n=0}^{\infty} \sum_{m=-n}^{n} \left(\frac{R_0}{r}\right)^n (n+1) C_{nm} Y_{nm}(\theta, \phi) \tag{2.2}$$

where the direction of g_r is positive downward, and the rotational potential is neglected.

In this study, the gravity data from GMM-3 is used. To examine the solutions of gravity field, the square root of the potential power per spherical harmonic degree can be used, which can be calculated from (Neumann et al., 2004)

$$\sigma_n = \sqrt{\frac{1}{2n+1} \sum_{m=-n}^{n} C_{nm}^2}. \tag{2.3}$$

Figure 2.2 shows the potential power per degree for the GMM-3 gravity solution (blue) and its uncertainties (red). The magnitude of the uncertainties increases gradually until it reaches the same level as that of the gravity signal at n = 100. To avoid the data with relatively high uncertainties, the gravity data with spherical harmonic degree higher than 90 is abandoned in this study.

The spherical harmonic toolbox from Root et al. (2016) is used in this study to conduct both Global Spherical Harmonic Synthesis (GSHS) and Global Spherical Harmonic Analysis (GSHA). The GSHS

[3] In operation since 2001
[4] In operation since 2006
[5] https://pds-geosciences.wustl.edu/dataserv/gravity_models.htm [05-01-2021]

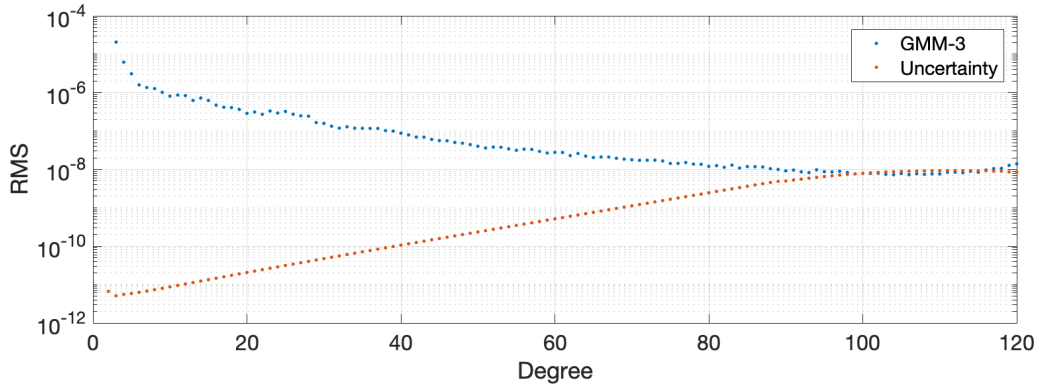

(a) The square root of the total power spectra of GMM-3 and its uncertainties for 0 < n ≦ 120.

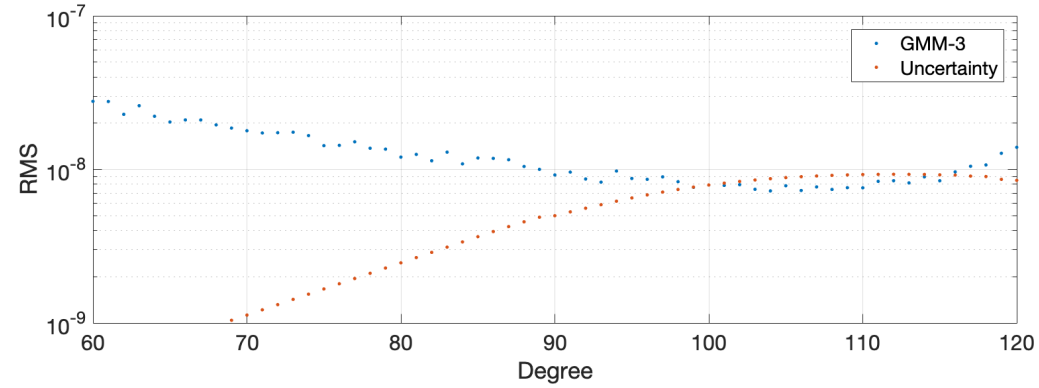

(b) The square root of the total power spectra of GMM-3 and its uncertainties for 60 ≦ n ≦ 120.

Figure 2.2: The square root of the potential power for all degrees (a) and higher degrees (b) of GMM-3 and its uncertainties.

converts the data from spherical harmonic domain into spatial domain. With the Stokes coefficients and several parameters of the planet as input, the GSHS software can be used to output the gravitational potential, components of gravitational fields (vectors) and components of gravity gradient tensors. The GSHA does the other way around, which converts the data from spatial domain into spherical harmonics domain. This spherical harmonic toolbox was initially designed for Earth, but it could be adapted to other celestial bodies (Backer, 2018). In addition, it could make the transformation between spatial and spherical harmonic for other spatial-distributed parameters like the crustal thickness and density.

2.2.2. Gravity Anomaly

The gravitational profile of a planet is related to its mass distribution. Extra mass on the surface of the planet could bring extra gravitational signals. Gravity anomalies can be observed by performing gravity reductions and provide information inside the lithosphere of Mars.

The gravity coefficients are connected to the mass distribution of the planet. For example, the degree-0 term (C_{00}) represents the mass of the planet, degree-1 terms (C_{10}, C_{11}, S_{11}) depends on the offset between the center of mass and the origin of the coordinate system, and C_{20} term stands for the flattening of the planet (Backer, 2018, Wieczorek, 2015). To study the gravity anomaly in the crust of Mars, the above-mentioned coefficients are removed from the gravity signal.

The resulted gravity anomaly (Figure 2.3) is called the Free-Air Anomaly (FAA) in this study, which shows the gravity anomaly in the crust (both on the surface and in the subsurface). One could expect that the regions with high topography would have larger FAA, and lower topography yields to lower FAA. In other words, the FAA is correlated to the topography. This might be true for regions like the Tharsis rise, Alba Mons, Elysium Mons and Valles Marineris. But different stories are found around the Isidis Planitia, Utopia Planitia and Hellas Basin where regions with negative topography show zero or even large position FAA.

Topography only gives information on the surface of Mars while the FAA also contains gravity signal

under the surface. The mismatch between the topography and FAA suggests that the subsurface part of the crust is not homogeneous and may vary in density or thickness.

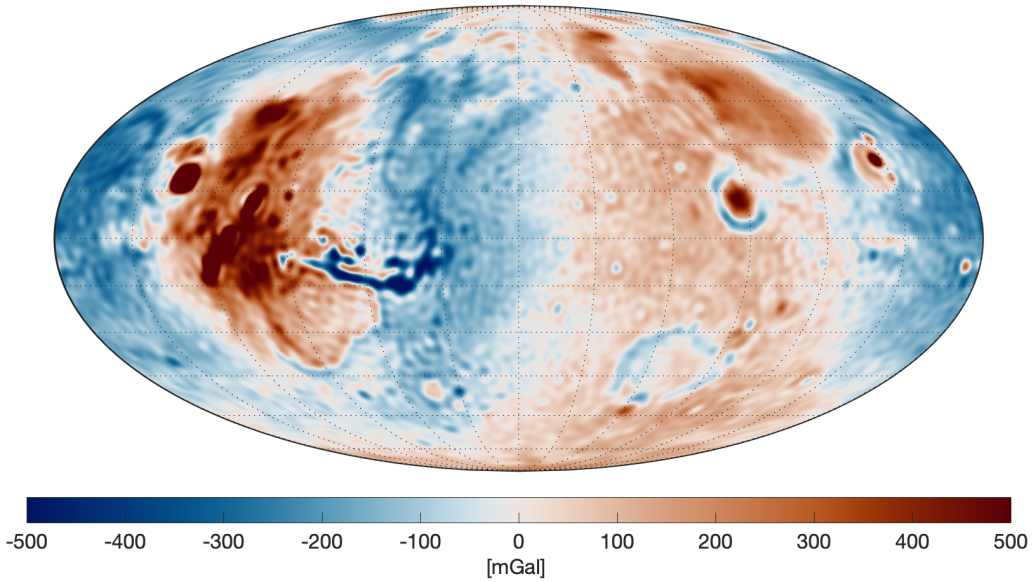

Figure 2.3: Free Air Anomaly of Mars, which is obtained by removing $C_{00}, C_{10}, C_{11}, S_{11}$ and C_{20} terms in the first 90 spherical harmonic degrees. The global dichotomy is absent because the central terms are removed. The range of the colorbar is limited to ± 500 mGal. The image is presented using a Mollweide projection with a central meridian of 0° longitude. Maximum and minimum FAA are 3570 mGal and -746 mGal, respectively.

To examine the gravity signal under the surface, one could remove signal contributed by topography from the FAA g_F by (Fowler, 2005)

$$g_B = g_F - \delta g_B \tag{2.4}$$

where g_B is called Bouguer gravity anomaly and δg_B is the Bouguer gravity correction which represents the gravity signal from topography

$$\delta g_B = 2\pi G \rho H \tag{2.5}$$

where G is the gravitational constant, ρ is the density of topography and H represents topographic height.

With topographic data from MOLA and a crustal density of 2900 kg/m^3, the Bouguer gravity anomaly for Mars is obtained with Equation 2.4 and shown in Figure 2.4. The dichotomy is not removed in the topographic data so that this global feature is clearly visible. The Bouguer gravity anomaly shows the gravity signal under the surface of Mars without the signal from topography. Zero Bouguer anomaly means the gravity anomaly can totally attribute to mass from topography. On the other hand, non-zero Bouguer anomaly implies that there are other sources of gravity signal from the subsurface of the planet. Positive Bouguer anomaly stands for excessive mass in the subsurface while negative Bouguer anomaly refers to a local mass deficiency.

Large Bouguer anomalies are found at the low-topography regions like a large part of the Northern hemisphere, Hellas Basin and Argyre Planitia. This suggests that more mass is located beneath these regions and reveals information about the local crustal structure. It could be that the crustal density at negative-topography regions is higher or negative topography results in thinner crust which makes dense mantle materials closer to the surface. Different theories to explain the gravity anomaly by establishing relationship between topography and crustal thickness or density are introduced in chapter 3.

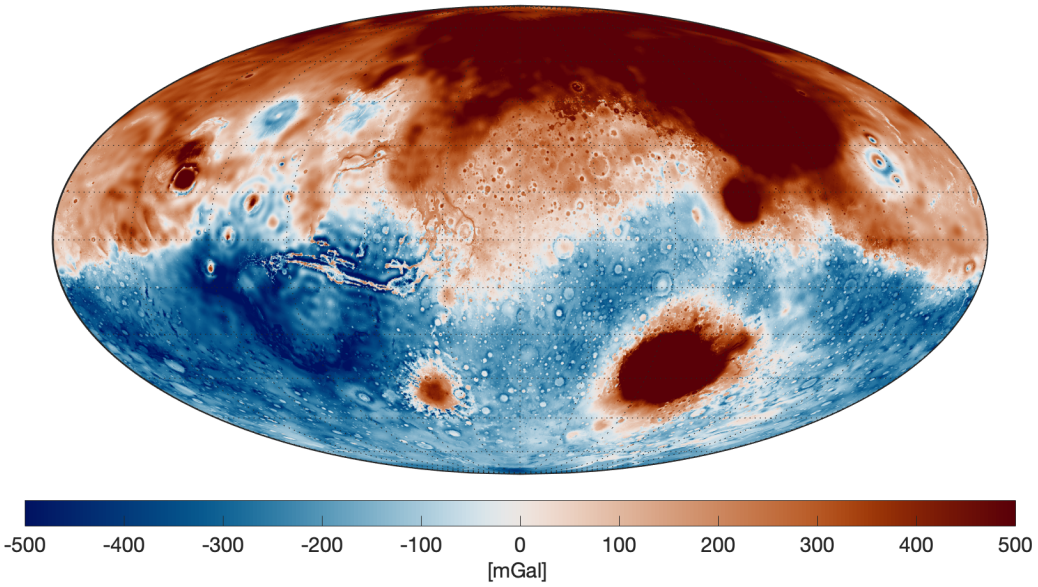

Figure 2.4: Bouguer Gravity Anomaly of Mars, which is obtained by performing Bouguer correction based on FAA. The global dichotomy is not removed in the Bouguer correction. The topography signal of volcanic mountains is not removed completed by simple Bouguer correction because a global crustal density of 2900 kg/m^3 is lower than that of volcanic materials. The range of the colorbar is limited to ± 500 mGal. The image is presented using a Mollweide projection with a central meridian of 0° longitude. Maximum and minimum Bouguer anomalies are 1359 mGal and -1065 mGal, respectively.

2.3. Faults and Stress

One way to evaluate the computed stress state from models is to compare it with the observed surface faults and see whether they adhere to the expected relationship. In this section, the surface faults data of Mars and basic stress theory are introduced.

2.3.1. Surface Faults

Faults refer to the lateral displacements happening on fractures (Turcotte and Schubert, 2014). The scales of surface faults vary from millimeters to kilometers. This thesis studies the large-scale (~km) surface faults on Mars.

On Earth, the state of faults can be monitored by seismology networks or GPS stations. But this is not the case (at least for now) to measure the faults on Mars. Imagery is a common source to obtain information about the faults on Mars. But identifying faults on Mars with images is constrained by many factors, such as the quality of data, the viewing angles and lighting conditions. These constraints make it difficult to obtain a global unbiased collection of faults. For example, a comprehensive investigation on faults with images from Viking missions were conducted by Anderson et al. (2001), and over 24,450 individual faults were found. But these faults only cover the Western hemisphere.

To avoid the disadvantages of images data in faults identification on Mars, Knapmeyer et al. (2006) added synthetic lighting to the MOLA shaded relief maps. They collected an inventory of Martian faults with about 8500 compressional and extensional tectonic faults (total length: 680,000 km). This Martian global surface faults database was updated in 2008 with 1409 new compressional faults and 4925 new extensional faults (Knapmeyer et al., 2008). The updated faults database also classified all faults into different groups based on the location of their origins and estimated the age for each fault.

Figure 2.5 shows the map of both compressional and extensional faults on Mars. The distribution of some faults are related to topographic features. For example, most normal faults are distributed around the Tharsis province and Valles Marineris in the Western hemisphere. The dichotomy boundary in the Eastern hemisphere, as well as the Hellas Basin, are clearly outlined by faults.

The faults distribution in the Western hemisphere is highly related to the Tharsis bulge. As it is shown in Figure 2.5, the majority of observed compressional faults in the Western hemisphere are distributed in circles around the Tharsis rise. These thrust faults are quite old (age > 3.5 Gyr) and could be the results of compressional stresses from large volcanic loads and the lithosphere flexure

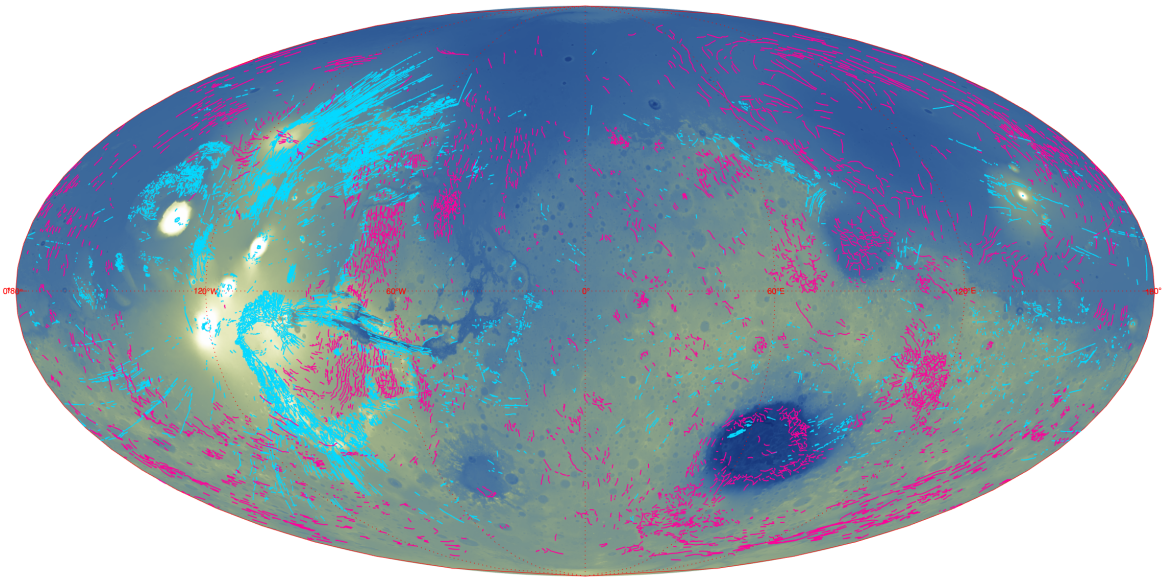

Figure 2.5: Global map of compressional (neon pink) faults and extensional (neon blue) faults on Mars. Topography is mapped in the background. The faults database is from Knapmeyer et al. (2006). This image is presented using a Mollweide projection with a central meridian of 0° longitude.

(Knapmeyer et al., 2006, Zhong, 2002). Similar topography-related thrust faults can also be seen around the boundary of Hellas Basin. Most of the extensional faults are in radial directions toward the Tharsis Montes, Alba Mons, Olympus Mons, Syria Planum and Tempe Terra. These normal faults suggest the wide spread of tensional stress in and around the Tharsis province at the time of formation.

The formation of strike-slip faults on Earth is related to the plate tectonics (Andrews-Hanna et al., 2008). Since Mars only has one single plate (no global plate tectonics), the number of strike-slip faults found on Mars is not comparable to that of the other two types of faults (Knapmeyer et al., 2006). That's why the strike-slip faults are absent in Figure 2.5. When comparing the calculated stress field to the observed faults, it is reasonable to use the most recent-formed faults from observation because models compute the lithosphere stress with new topography and/or gravity data. However, the dating of faults was based on the age of geological structure where the faults were found (Figure 2.6). So, the ages of faults in the database only present the "reliable maximum ages for each fault" as the fault could be younger than its surrounding surface.

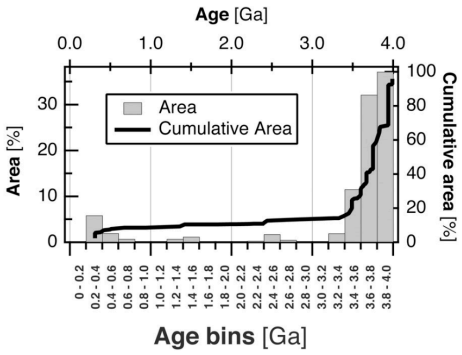

(a) Percentage of the Martian surface at given age span (Knapmeyer et al., 2006).

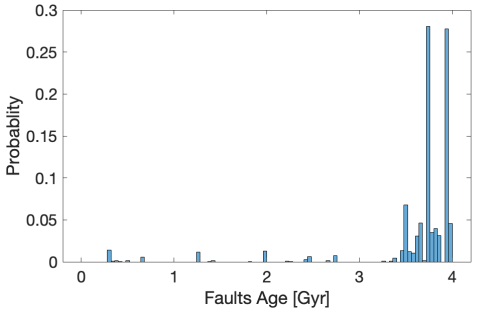

(b) Histogram of the faults age in Figure 2.5. Data source: Knapmeyer et al. (2006, 2008).

Figure 2.6: Histograms for (a) the age of Martian surface and (b) age of surface faults. The distribution of age for faults is similar to that of the surface. 75% of the surface is older than 3.5 Gyr. 1 Ga = 1 Gyr = 10^9 years.

The state of the stress which induces the fault can be retrieved by examining the direction of the displacement on the fault (Turcotte and Schubert, 2014). For instance, a normal fault occurs when a

region is under tensional (extensional) stresses, and compressional stress could result in thrust faulting, as illustrated in Figure 2.7 (a) and (b) respectively. Strike-slip faults can be found in the region where shear stress is dominant, as shown in Figure 2.7 (c) and (d).

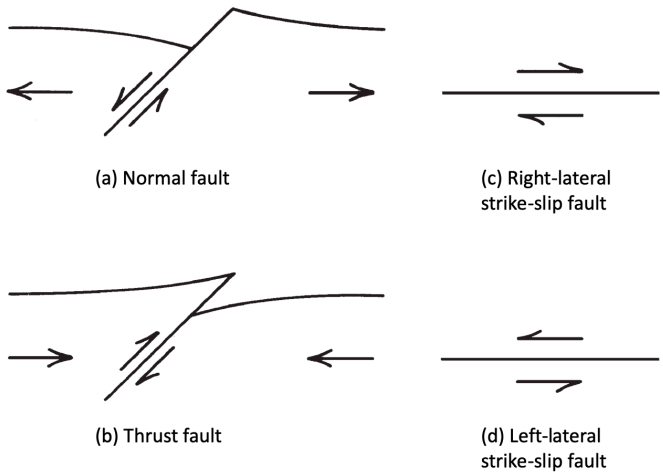

Figure 2.7: Cross sections of different faults (Turcotte and Schubert, 2014).

In this study, models are built to calculate the stress state in the lithosphere of Mars. By extracting the calculated surface stresses and comparing them to the distribution of observed faults, one can examine the performance of the models.

2.3.2. Stress and Strain

In continuum mechanics, the Cauchy stress tensor is widely used to define the state of stress at a point in three dimensions. It contains nine components, including three normal stress components (σ_x,σ_y,σ_z) at the diagonal entries and six shear stress components (τ_{xy},τ_{yx},τ_{xz},τ_{zx},τ_{yz},τ_{zy}) at the off-diagonal entries. This is illustrated visually in Figure 2.8 and mathematically in Equation 2.6.

$$\sigma_{3d} = \begin{bmatrix} \sigma_{11} & \sigma_{12} & \sigma_{13} \\ \sigma_{21} & \sigma_{22} & \sigma_{23} \\ \sigma_{31} & \sigma_{32} & \sigma_{33} \end{bmatrix} \equiv \begin{bmatrix} \sigma_{xx} & \sigma_{xy} & \sigma_{xz} \\ \sigma_{yx} & \sigma_{yy} & \sigma_{yz} \\ \sigma_{zx} & \sigma_{zy} & \sigma_{zz} \end{bmatrix} \equiv \begin{bmatrix} \sigma_x & \tau_{xy} & \tau_{xz} \\ \tau_{yx} & \sigma_y & \tau_{yz} \\ \tau_{zx} & \tau_{zy} & \sigma_z \end{bmatrix} \tag{2.6}$$

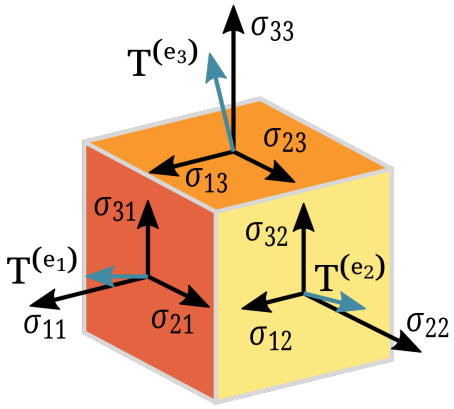

Figure 2.8: Components of stress tensor in Cartesian coordinate (Helwa, 2009). Different expressions for the components are also shown in Equation 2.6.

Plane Stress

One goal of this study is to find out the faults distribution from calculated stress state in the lithosphere of Mars. Since the surface of Mars is dominated by compressional and extensional faults, the stress components in the vertical direction can be ignored in the stress-fault relation analysis. In other words, plane stress theory is applied in the analysis.

To express the stress state in 2D, only four stress components, which define the normal stress and shear stress components in two directions, are needed. Equation 2.6 can be reduced into

$$\sigma_{2d} = \begin{bmatrix} \sigma_{11} & \sigma_{12} \\ \sigma_{21} & \sigma_{22} \end{bmatrix} = \begin{bmatrix} \sigma_{xx} & \sigma_{xy} \\ \sigma_{yx} & \sigma_{yy} \end{bmatrix} = \begin{bmatrix} \sigma_x & \tau_{xy} \\ \tau_{yx} & \sigma_y \end{bmatrix}. \tag{2.7}$$

The transformation equations for the plane stress are given by (Gere and Goodno, 2012)

$$\sigma_{x1} = \sigma_x \cos^2\theta + \sigma_y \sin^2\theta + 2\tau_{xy} \sin\theta \cos\theta \tag{2.8a}$$

$$\sigma_{y1} = \sigma_x \sin^2\theta + \sigma_y \cos^2\theta - 2\tau_{xy} \sin\theta \cos\theta \tag{2.8b}$$

$$\tau_{x1y1} = (\sigma_y - \sigma_x) \sin\theta \cos\theta + \tau_{xy} \left(\cos^2\theta - \sin^2\theta\right) \tag{2.8c}$$

where σ_{x1} and σ_{y1} are the new normal stresses, τ_{x1y1} and τ_{y1x1} are the new shear stresses, θ is the angle between the old and new coordinates (Figure 2.9). Moment equilibrium gives $\tau_{x1y1} = \tau_{y1x1}$.

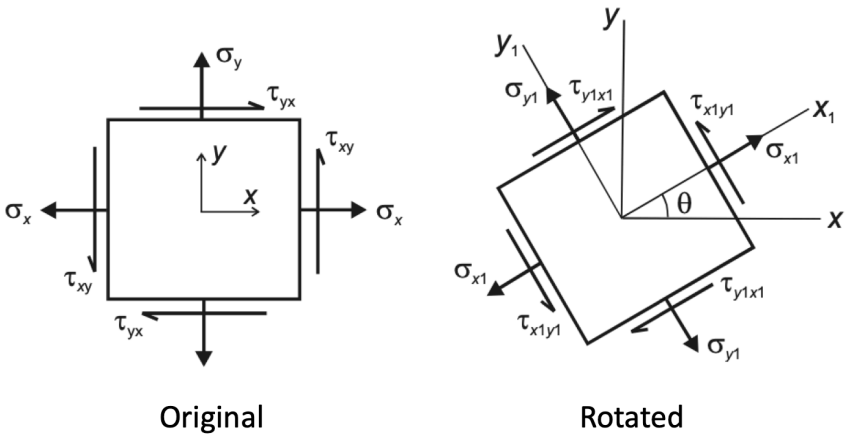

Figure 2.9: Coordinate transformation for plane stresses(Gere and Goodno, 2012).

A special plane could be found when the shear stress $\tau_{x1y1} = 0$ in Equation 2.8. Such a plane is called the Principal Plane, and the angle is given by

$$\tan 2\theta_p = \frac{2\tau_{xy}}{\sigma_x - \sigma_y}. \tag{2.9}$$

The normal stresses of the principal plane can be calculated by combining Equation 2.8 and 2.9, which is given by

$$\sigma_1 = \frac{1}{2}(\sigma_x + \sigma_y) + \sqrt{\frac{1}{4}(\sigma_x - \sigma_y)^2 + \tau_{xy}^2} \tag{2.10a}$$

$$\sigma_2 = \frac{1}{2}(\sigma_x + \sigma_y) - \sqrt{\frac{1}{4}(\sigma_x - \sigma_y)^2 + \tau_{xy}^2} \tag{2.10b}$$

where σ_1 and σ_2 are the maximum and minimum principal stresses, respectively. The direction of the principal stress is defined positive outward as shown in Figure 2.9. It means that positive principal stresses are tensive/tensional/tensile while negative principal stresses are compressive/compressional. However, it doesn't mean that maximum principal stress is always tensional since it could be smaller

than zero in some cases. So, when conducting stress analysis, it's important to distinguish the sign of the principal stress and then the magnitude.

Apart from the principal stresses, **Von Mises stress** is also used in many stress analyses to compare with the yield stress criterion and gives a good indication of margins over possible plastic response. It can be directly used to identify some regions of interest in the stress plots prior to a principal stress analysis. The equation for Von Mises stress in 2D is given by

$$\sigma_{\mathrm{v}} = \sqrt{\sigma_x^2 - \sigma_x\sigma_y + \sigma_y^2 + 3\sigma_{xy}^2}. \tag{2.11}$$

As a scalar combination of the stress components, Von Mises stress does not contain information about the direction of stress or other property like tension and compression.

Plane Strain

The plane strain has four components and can be written as

$$\epsilon_{2d} = \begin{bmatrix} \epsilon_{11} & \epsilon_{12} \\ \epsilon_{21} & \epsilon_{22} \end{bmatrix} = \begin{bmatrix} \epsilon_{xx} & \epsilon_{xy} \\ \epsilon_{yx} & \epsilon_{yy} \end{bmatrix} = \begin{bmatrix} \epsilon_x & \gamma_{xy} \\ \gamma_{yx} & \epsilon_y \end{bmatrix} \tag{2.12}$$

where ϵ_x and ϵ_y are the normal strains, γ_{xy} and γ_{yx} are the shear strains.

The transformation equations for plane strain are given by (Gere and Goodno, 2012)

$$\epsilon_{x1} = \epsilon_x \cos^2\theta + \epsilon_y \sin^2\theta + \gamma_{xy} \sin\theta \cos\theta \tag{2.13a}$$

$$\epsilon_{y1} = \epsilon_x \sin^2\theta + \epsilon_y \cos^2\theta - \gamma_{xy} \sin\theta \cos\theta \tag{2.13b}$$

$$\gamma_{x1y1} = 2\left(\epsilon_y - \epsilon_x\right) \sin\theta \cos\theta + \gamma_{xy}\left(\cos^2\theta - \sin^2\theta\right) \tag{2.13c}$$

which is slightly different from that of the plane stress in Equation 2.8.

Similarly, the principal plane can be determined by

$$\tan 2\theta_p = \frac{\gamma_{xy}}{\varepsilon_x - \varepsilon_y} \tag{2.14}$$

where θ_p shows the direction of the principal plane.

The maximum and minimum principal strains can be calculated by

$$\epsilon_1 = \frac{1}{2}\left(\epsilon_x + \epsilon_y\right) + \sqrt{\frac{1}{4}\left(\epsilon_x - \epsilon_y\right)^2 + \frac{1}{4}\gamma_{xy}^2} \tag{2.15a}$$

$$\epsilon_2 = \frac{1}{2}\left(\epsilon_x + \epsilon_y\right) - \sqrt{\frac{1}{4}\left(\epsilon_x - \epsilon_y\right)^2 + \frac{1}{4}\gamma_{xy}^2}. \tag{2.15b}$$

Strain ϵ and stress σ can be linked through the Young's modulus (modulus of elasticity) E by

$$\sigma = E\epsilon. \tag{2.16}$$

3

Crustal Models for Mars

When seismic measurements from the ground are not available or insufficient, modeling the relationship between the topography and gravity of a planet and comparing it to the observations is a useful method to obtain information about the planet's subsurface structure (Wieczorek, 2015). In this study, the data of topography and gravity are combined with geological theory of isostasy. They are used to invert for geophysical parameters for Mars. This chapter introduces different isostatic models for Mars and a spectral approach to compare these models with observation.

3.1. Models of Isostasy

The idea of isostasy was introduced to explain two phenomena. Firstly, the mismatch between the gravity anomalies and the gravitational attraction of large mountains on Earth (Airy, 1855). Secondly, how the topography is soundly supported by a rigid crust together with a viscous mantle? The first phenomenon can be explained by isostatic equilibrium in which the gravity anomalies of topography are compensated underneath the surface. There are two end-member in classic isostasy, Airy and Pratt, which use different approaches to implement the compensation. The second question can be answered from the perspective of stress: the non-hydrostatic stresses induced by the topography support the crust (Jeffreys, 1943). Since non-hydrostatic stress is the difference between the actual stress and hydrostatic pressure in the crust, it is also called the "deviatoric stress".

3.1.1. Classic Isostasy

Classic isostatic models simplify the problem by assuming local compensation, which means the crustal columns can move independently in the vertical direction and do not affect each other. Early isostasy includes two models from Airy and Pratt separately (Watts, 2001). In Airy's model, the crustal density is uniform. The compensation is reached by varying the crustal thickness. Thus, a larger positive topography would yield to a deeper root while negative topography would cause a shallower root. But in Pratt's model, a uniform-thickness crust is assumed, and compensation is achieved by changing lateral density. The root beneath positive topography has a lower density.

General Equations

The equations for Airy's models can be found in Equation 3.1 and Equation 3.2. Equation 3.1 describes the depth of the root under positive topography, where h_1 is the topographic height, ρ_u is the density of the crust and ρ_s is the density of the mantle. For the case of sea floor, the depth of the root, r, is shown in Equation 3.2 where ρ_w is the density of water. In case of pure negative topography (without infill materials), the term ρ_w can be removed.

$$r_1 = \frac{\rho_u h_1}{\rho_s - \rho_u} \tag{3.1}$$

$$r_3 = \frac{\rho_u - \rho_w}{\rho_s - \rho_u} d \tag{3.2}$$

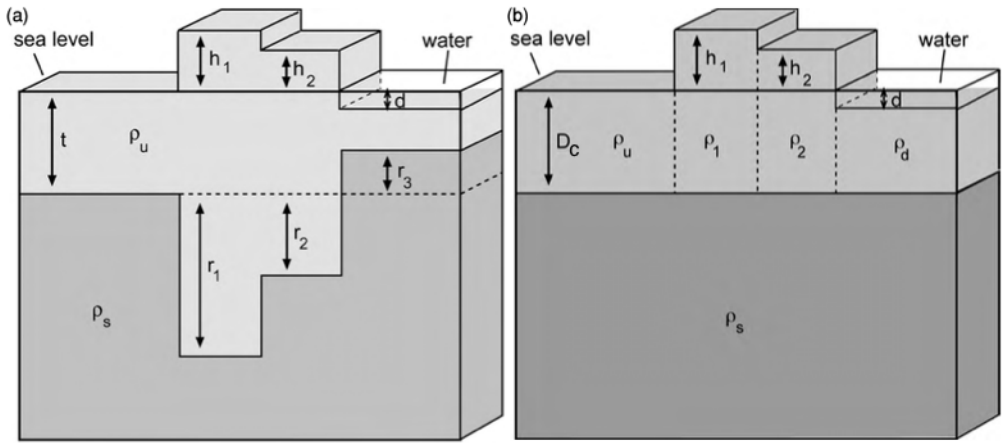

Figure 3.1: Illustrations of (a) Airy's theory of isostasy and (b) Pratt's theory of isostasy (Fowler, 2005).

The mathematical description for Pratt's model can be found in Equation 3.3 and Equation 3.4, where ρ_u is the mean density of the crust, D_c is the depth of compensation of the crust, ρ_1 and ρ_d represent the densities of the crust under topographic loads.

$$\rho_1 = \frac{\rho_u D_c}{h_1 + D_c} \tag{3.3}$$

$$\rho_d = \frac{\rho_u D_c - \rho_w d}{D_c - d} \tag{3.4}$$

Equations for Mars

For Mars, the equations for both Airy and Pratt can be simplified by removing the density of water, ρ_w, and replacing d with h. After this simplification, there is no need to distinguish negative and positive topography in two separate equations as the sign would be included in the topography term h. The depth of the root r from Airy and density of crust ρ from Pratt can be simplified into

$$r = \frac{\rho_c h}{\rho_m - \rho_c} \tag{3.5}$$

where ρ_c is the density of the crust, ρ_m is the density of the mantle,

$$\rho = \frac{\rho_0 D_c}{D_c + h} \tag{3.6}$$

where ρ_0 is the mean crustal density.

The assumption of local compensation neglects the shear stresses between the crustal columns and only relies on the buoyancy to provide the support. On the one hand, these assumptions simplified the problem and made the mathematical expressions straightforward. On the other hand, ignoring those physical processes made both Airy and Pratt the end-member among the models of isostasy.

3.1.2. Flexural Isostasy

Unlike Airy or Pratt isostasy, another type of isostatic theory allowing the crustal column to exert shear stresses on its neighbors. Such theory is called regional or flexural isostasy. The flexural isostasy theory assumes the lithosphere to be an elastic plate or shell. Thus, when a topographic load is applying to the lithosphere, the compensation would be distributed around a larger area than the Airy's model. Since the pressures from the loads spread over a broad region in flexural models, the maximum crustal thickness is not as large as that of the Airy's model, as shown in Figure 3.2.

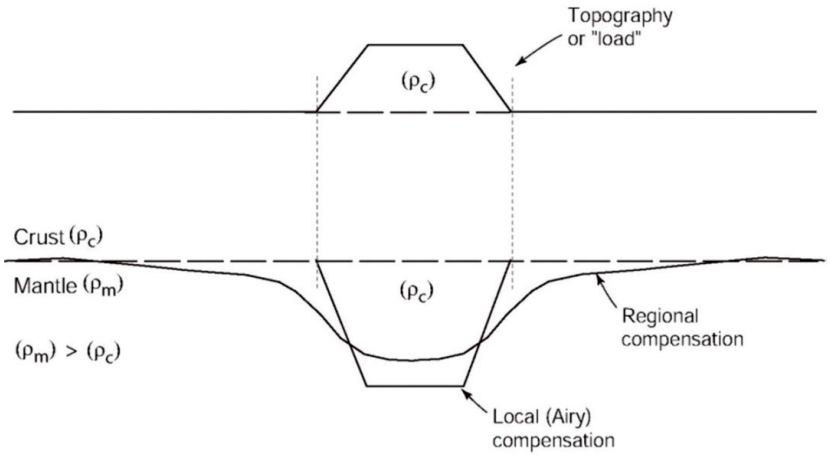

Figure 3.2: Comparison of regional isostasy (infinite plate) and local isostasy (Airy) models(David, 2010). Airy's model results in a larger crustal thickness than the infinite plate model. Pratt's model would bring larger density variations than the flexural model.

Infinite Plate Model

The infinite plate model is a simple but common flexural model. It simulates the lithosphere as an infinite plate floating on viscous interior materials. To describes the effect of flexural models, Watts (2001) introduced the concept of flexural response function, which is the ratio between the deflection or flexure (output) of the lithosphere and the geological loads (input). The values of the flexural response function ranges from zero to one, corresponding to the Bouguer response (no compensation) and Airy response (full compensation), respectively.

The flexural response function for the infinite plate is given (Watts, 2001) by:

$$\Phi(n)_{plate} = \left[1 + \frac{D}{(\rho_m - \rho_c)g}\left(\frac{2n+1}{2R}\right)^4\right]^{-1} \tag{3.7}$$

where n is the spherical harmonic degree, r is radius of the planet, g is the gravitational acceleration, and D is called the flexural rigidity.

$$D = \frac{ET_e^3}{12(1-v^2)} \tag{3.8}$$

In Equation 3.8, E is the modulus of elasticity (or Young's modulus) and v is the Poisson's ratio. T_e is the effective elastic thickness of lithosphere, which describes the lithosphere's resistance to bending or deflection with vertical loads. A higher effective elastic thickness represents a more rigid lithosphere which would not easily bend. Airy's model is locally compensated and has no resistance to bending when loads are applied. So, the value for Airy's flexural parameter is zero, which in turn brings the value of its flexural response function to one:

$$\Phi(n)_{local} = (1)^{-1} \tag{3.9}$$

which also applies to the Pratt's model.

An example of the flexural response function as a function of spherical harmonic degree n is shown in Figure 3.3. It is plotted for Earth with lithospheric thickness T_e ranges from 25 to 75 km by Watts and Moore (2017). The vertical axis shows the value of flexural response function, which is also the degree of compensation. The horizontal axis represents different spherical harmonic degree n and its equivalent wavelength λ. On the surface of a sphere with a radius of r, these two parameters are linked by the Jeans' relation (Wieczorek and Simons, 2005)

$$\lambda = \frac{2\pi R}{\sqrt{n(n+1)}}. \tag{3.10}$$

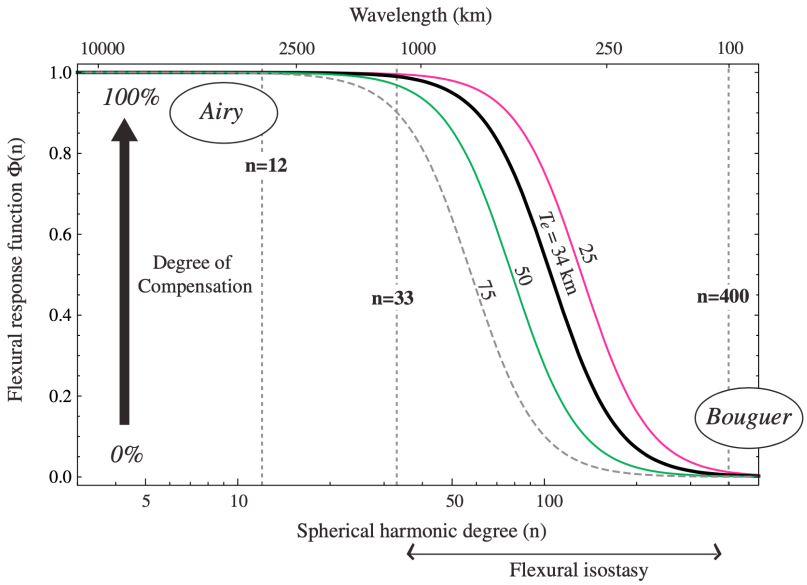

Figure 3.3: Flexural response function $\Phi(n)_{plate}$ of the infinite plate with various T_e for Earth (Watts and Moore, 2017).

In Figure 3.3, different T_e yields different curves but they share a similar pattern like a low-pass filter. The flexural response functions Φ_{plate} equal to one at low-degree (long-wavelength) region, begin to decrease between n = 12 and n = 33, and reach zero at high-degree (low-wavelength) zone. $\Phi_{plate} = 1$ stands for local isostasy, which means the region is 100% compensated (Airy case in Figure 3.3). This is illustrated in the bottom plot of Figure 3.4 where the wavelength of the load is so large that the lithosphere could not support it at all. On the contrary, $\Phi_{plate} = 0$ means no compensation happened and is called the "uncompensated" Bouguer case. The Bouguer case is shown at the top plot of Figure 3.4. It shows that the wavelength of the load is so small that the lithosphere can support it without deflection. The regions in between the Airy and Bouguer in Figure 3.3 are thought to have flexural isostasy, in which the loads are neither large enough to "destroy" the lithosphere nor small enough to leave the lithosphere intact. Both isostatic compensation and lithosphere bending would support the loads. The plot of flexural response functions for Mars can be found in Figure 3.6.

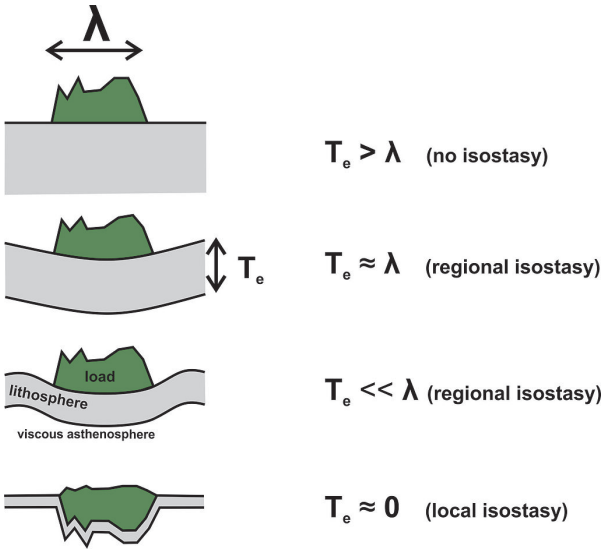

Figure 3.4: Isostatic response of lithosphere (grey) to vertical loads(green) (Gaianauta, 2015). T_e is the effective elastic thickness of the lithosphere. λ is the wavelength (Equation 3.10) of the load. Local isostasy happens where the lithosphere is too thin to support the load. A stronger lithosphere supports the load with regional (or flexural) isostasy. In the extreme case, the lithosphere with very large thickness can fully support the load without isostatic compensation.

Thin Shell Model

The infinite plate model may provide a good representation of short-wavelength features at the surface of a planet. But it is not a good idea to apply infinite plate model for large-wavelength features where the effect of planet's curvature appears. After all, neither the Earth nor Mars is flat. Thus, a more realistic model which considers both flexure and the spherical shape of the planet is desired.

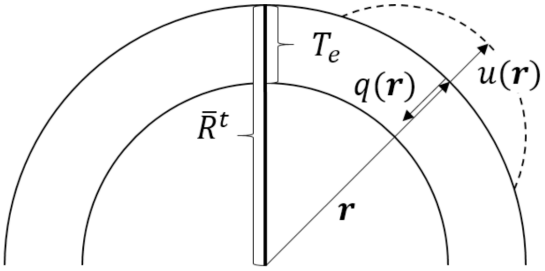

Figure 3.5: Illustration of an elastic thin shell (T_e << R) by Thor (2016). It shows the deflection $u(r)$ and loading pressure $q(r)$ (or $p(r)$) caused by a load at position **r**.

The elastic thin shell model is shown in Figure 3.5. For a thin shell with radius r and an uniform thickness of T_e, Kraus (1967) derived how much vertical displacement/deflection w the thin shell model would have under certain loads

$$\left[D\nabla^6 + 4D\nabla^4 + ET_eR^2\nabla^2 + 2ET_eR^2\right]w = R^4(\nabla^2 + 1 - v)p \tag{3.11}$$

where ∇^2 is the Laplacian operator (see Appendix A), D is the flexural rigidity (Equation 3.8), and p is the loading pressure

$$p = g\left[\rho_c h - (\rho_m - \rho_c)\, w\right]. \tag{3.12}$$

Based on Equation 3.11, Turcotte et al. (1981) expanded both displacement w and loading height h in spherical harmonics and found the ratios between the coefficients as a function of spherical harmonics degree n:

$$\frac{w_n}{h_n} = \left(\frac{\rho_c}{\rho_m - \rho_c}\right)\left\{\frac{n(n+1) - (1-\nu)}{\sigma\left[n^3(n+1)^3 - 4n^2(n+1)^2\right] + \tau[n(n+1) - 2] + n(n+1) - (1-\nu)}\right\} \tag{3.13}$$

where

$$\tau = \frac{ET_e}{R^2(\rho_m - \rho_c)g} \tag{3.14}$$

$$\sigma = \frac{\tau}{12(1-v^2)}\left(\frac{T_e}{R}\right)^2 \tag{3.15}$$

The second term at the right-hand side of Equation 3.13 was referred to C_n as the "degree of compensation for degree n" (Turcotte et al., 1981), which is given by

$$C_n = \frac{n(n+1) - (1-\nu)}{\sigma\left[n^3(n+1)^3 - 4n^2(n+1)^2\right] + \tau[n(n+1) - 2] + n(n+1) - (1-\nu)} \tag{3.16}$$

It's important to note that the concept of the "degree of compensation" from Turcotte et al. (1981) is equivalent to the concept of the "flexural response function" from Watts (2001). In this thesis, the name "flexural response function" is used. However, Equation 3.16 from Turcotte et al. (1981) is not the correct flexural response function for the thin shell model due to a missing term in Equation 3.11 from Kraus (1967).

This mistake was pointed out by Beuthe (2008), who also derived the equation of deflection u for a constant-thickness elastic thin shell with under loading pressure p as

$$\eta D\Delta\Delta'\Delta' u + \frac{R^2}{\alpha}\Delta' u = -R^4\left(\Delta' - 1 - \nu\right)p + R^3\left(\frac{1}{1+\xi}\Delta' - 1 - \nu\right)\Delta\Omega \tag{3.17}$$

where η is a parameter very close to 1

$$\eta = \frac{\xi}{1+\xi} = \left(1 + \frac{T_e^2}{12R^2}\right)^{-1}, \tag{3.18}$$

α is inversion the of the extensional rigidity

$$\alpha = \frac{1}{K\,(1-v^2)} = \frac{1}{ET_e}, \tag{3.19}$$

ξ is a dimensionless ratio

$$\xi = R^2\frac{K}{D} = 12\frac{R^2}{T_e^2} \tag{3.20}$$

and the operator Δ is linked to the Laplacian operator

$$\Delta = \nabla^2. \tag{3.21}$$

For homogeneous thin shells, one can assume

$$\Delta\Omega = 0. \tag{3.22}$$

With Equation 3.18 to Equation 3.22, Equation 3.17 can be written as

$$\left[D\nabla^2\left(\nabla^2\right)'\left(\nabla^2\right)' + R^2ET_e\left(\nabla^2\right)'\right]u = -R^4\left[\left(\nabla^2\right)' - 1 - v\right]p. \tag{3.23}$$

One can remove the $(\nabla^2)'$ operator in Equation 3.23 with Equation A.2:

$$\left[D\nabla^6 + 4D\nabla^4 + \left(4D + R^2ET_e\right)\nabla^2 + 2R^2ET_e\right]u = -R^4\left(\nabla^2 + 1 - v\right)p, \tag{3.24}$$

which is almost the same as Equation 3.11. The different sign at the right-hand sides of both equations is a result of different definition for the displacement/deflection direction ($u = -w$). The other difference is that the term "$4D\nabla^2 w$" is missing at the left-hand side of Equation 3.11. This mistake happened when Kraus combined equations for the thin shells in the final step Beuthe (2008). The same error is also seen in other studies (Banerdt, 1986, McGovern et al., 2002, Turcotte et al., 1981) and has a consequence for the first harmonic degree component.

Since Turcotte et al. (1981) derived the flexural response function (Equation 3.16) based on a mistaken version of thin shell models (Equation 3.11), a correct thin shell flexural response function is desired. To achieve that, one need to transform Equation 3.24 into spherical harmonic space and derive the ratio between the coefficients of displacement w or u and loading height h. This can be done with Equation A.3, which transforms Equation 3.24 into

$$\begin{aligned}\left(\frac{ET_e^3}{12(1-v^2)}\left[-n^3(n+1)^3 + 4n^2(n+1)^2 - 4n(n+1)\right] + R^2ET_e(-n(n+1)+2)\right)u_{lm} \\ = -R^4\left[-n(n+1) + 1 - v\right]p_{lm},\end{aligned} \tag{3.25}$$

where u_{lm} and p_{lm} are the spherical harmonics coefficients of u and p, respectively.

Inserting Equation 3.12 into Equation 3.25 gives the relationship between the coefficients u_{lm} and h_{lm} as following

$$\frac{u_{lm}}{h_{lm}} = \left(\frac{\rho_c}{\rho_m - \rho_c}\right)\Phi(n)_{shell} \tag{3.26}$$

where $\Phi(n)_{shell}$ is the correct flexural response function for the thin shell:

$$\Phi(n)_{shell} = \frac{n(n+1) - (1-v)}{\sigma[n^3(n+1)^3 - 4n^2(n+1)^2 + 4n(n+1)] + \tau[n(n+1) - 2] + n(n+1) - (1-v)}. \tag{3.27}$$

Compared to Equation 3.16, Equation 3.27 has the missing term "$4n(n+1)\sigma$" back. With a few more steps (see Appendix A), one can write Equation 3.27 into a format similar to that of the infinite plate (Equation 3.7) as

$$\Phi(n)_{shell} = \left[1 + \frac{D}{(\rho_m - \rho_c)g}\left(\frac{1}{R^4}\frac{[n(n+1)-2]^2}{1 - \frac{1-v}{n(n+1)}} + \frac{12(1-v^2)}{T_e^2R^2}\frac{1 - \frac{2}{n(n+1)}}{1 - \frac{1-v}{n(n+1)}}\right)\right]^{-1}. \tag{3.28}$$

Deriving the flexural response functions for different isostatic models in this study is essential for the following three reasons. Firstly, the flexural response functions themselves could reflect the characteristics of different isostatic models. By simply comparing the functions in Table 3.1, one could find that those functions only have small differences. Compared to the flexural response function of local isostatic models (Equation 3.9), the function of the infinite plate (Equation 3.7) has an extra term which represents the bending or flexure of the model. For the thin shell model which considers the curvature of the planet, additional terms that stand for membrane stresses are added to the flexural response function (Equation 3.28). Their similarities and differences are visualized in the plots of flexural response functions in Figure 3.6.

Secondly, the flexural response function is a powerful tool to conduct flexural isostatic analysis. With the crustal profiles computed from local isostasy, one could filter these profiles using the flexural response function and obtain the new profiles under flexural isostasy. This process is described by (Mussini, 2020)

$$M_{lm} = A_{lm}\Phi(n) \tag{3.29a}$$
$$D_{lm} = P_{lm}\Phi(n) \tag{3.29b}$$

where A_{lm} is the crustal thickness profile from Airy's model, p_{lm} is the crustal density profile from Pratt's model, M_{lm} and D_{lm} are the new profiles for crustal thickness and density distribution, respectively. All profiles are in the domain of spherical harmonics, and the multiplication in Equation 3.29 is conducted for each degree (n).

Thirdly, the flexural response function simplifies the flexural problem into one single equation. Only a few parameters, which represent the size of the planet, strength of the gravity field and the property of the lithosphere, are used. By changing the values of these parameters, one can theoretically compare the characteristics of the lithosphere for different celestial bodies.

Table 3.1: Comparison of the Flexural Response Function for different models.

Model		Flexural Response Function
Classic Isostasy	Airy and Pratt	$\Phi(n)_{local} = (1)^{-1}$
Flexural Isostasy	Infinite Plate	$\Phi(n)_{plate} = \left[1 + \frac{D}{(\rho_m - \rho_c)g}\left(\frac{2n+1}{2R}\right)^4\right]^{-1}$
	Thin Shell	$\Phi(n)_{shell} = \left[1 + \frac{D}{(\rho_m - \rho_c)g}\left(\frac{1}{R^4}\frac{[n(n+1)-2]^2}{1-\frac{1-\nu}{n(n+1)}} + \frac{12(1-\nu^2)}{T_e^2 R^2}\frac{1-\frac{2}{n(n+1)}}{1-\frac{1-\nu}{n(n+1)}}\right)\right]^{-1}$

Table 3.2: Summary of Parameters for both Mars and Earth. The values in the table are used in this study unless otherwise specified. All values for Earth are taken from Watts and Moore (2017). The sources of the values of parameters for Mars are listed in the last column.

Parameters		Mars	Earth	Unit	Reference
Gravitational Constant	G	6.67×10^{-11}		$m^3/kg/s^2$	(Watts and Moore, 2017)
Mean Radius	r	3389.5	6371.0	km	(Wieczorek, 2015)
Gravitational Acceleration	g	3.72	9.81	m/s^2	(Hirt et al., 2012)
Crustal Density	ρ_c	2900	2650	kg/m^3	(Wieczorek, 2015)
Mantle Density	ρ_m	3500	3330	kg/m^3	(Wieczorek, 2015)
Young's modulus	E	65	100	GPa	(Kalousová et al., 2012)
Poisson's Ratio	ν	0.25	0.25	-	(Kalousová et al., 2012)

Based on Equation 3.7 and Equation 3.28, a visualisation of the flexural response functions of the infinite plate and the thin shell for Mars is presented in Figure 3.6. The parameters for Mars are stated in Table 3.2. The blue curves represent the flexural response of the infinite plate as a function of spherical harmonics degree n while that of the thin shell is represented by the red curves.

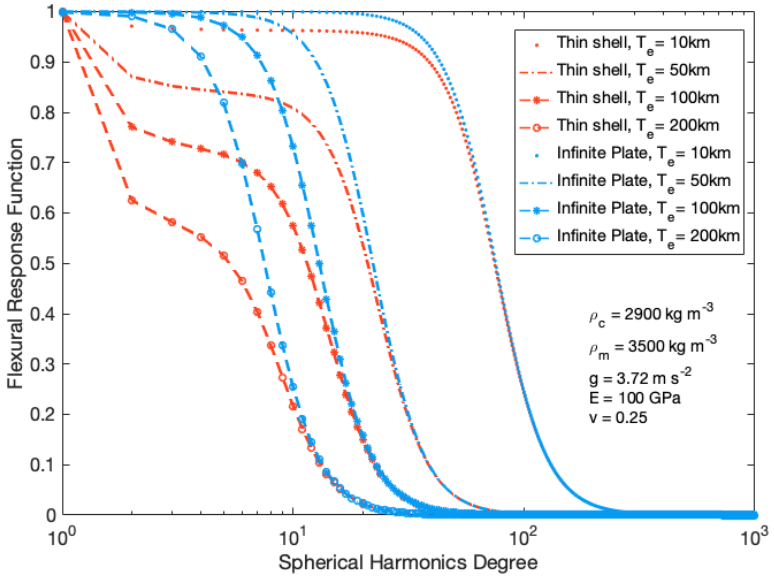

Figure 3.6: Comparison between the flexural response function of the thin shell model and infinite plate model with various T_e for Mars. Values for parameters are specified.

The infinite plate models in Figure 3.6 show similar behaviours as found in Figure 3.3: their values decrease from one to zero as the degree increases and function like low-pass filters which block the features in the high-degree (or short-wavelength) band. This is different from models of local isostasy which have a constant response of one. Compared to models of local isostasy, flexure is added to the infinite models. The bending stresses induced from the flexure could support the topographic loads at certain degrees where isostatic compensation is not needed. Besides, the infinite plate models shift to the left-hand side as the lithospheric thickness T_e increases. This means the model with a higher lithospheric thickness has a higher rigidity (Equation 3.8) which allows its filter effect to start at a lower degree (or a longer wavelength).

The flexural response functions of the thin shell models overlap with those of the infinite plate models at high-degree region but they diverge from the plate models at low-degree zone. This divergence happens because membrane stresses are taken into account in the thin shell model. The longer the wavelength, the greater the influence of the planet's curvature would be. Thus, more membrane stresses are induced by the thin shell model at low-degree region.

In short, the difference in the flexural response functions between the models of local isostasy and the infinite plate model shows the effect of bending stresses. The divergence in the flexural response functions between the infinite plate model and the thin shell model comes from the membrane stresses. This is consistent with findings from other studies (Kalousová et al., 2012, Turcotte et al., 1981).

A comparison of the flexural response functions between Mars and the Earth in the thin shell model is shown in Figure 3.7. The parameters for both planets are stated in Table 3.2. The red curve is the flexural response function for Mars with a best-fitting lithospheric thickness of 158 km[1]. That for the Earth is represented by the blue curve with a T_e = 34 km. The green curve shows how Mars would behave with a lithospheric thickness of 34 km, for comparative purposes.

The difference between the flexural response functions (blue and green) of T_e=34 km for both planets comes from the difference in their planetary parameters. The radius of the planet is believed to have the largest effect (the radius of Earth is nearly twice than that of Mars). Since the curvature is inverse proportional to the radius of the circle in a plane, the curvature effect of Mars is larger than that

[1]The best-fitting lithospheric thickness is calculated for $2 \leqq n \leqq 90$.

of the Earth. Relatively, at the same spherical harmonics degree, the support from membrane stresses on Mars is larger than that on the Earth.

In reality, Mars has a more rigid lithosphere (T_e = 158 km from this study), and the difference the flexural response functions of Mars and the Earth with their best-fitting T_e = 34 km is larger than that from the previous comparison (between the blue and green curves). Comparing the blue and red curves not only shows that the lithosphere of Mars is relatively stronger but also reveals different isostatic compensation on both planets. While the local isostasy dominates the first 20 degrees on the Earth, it does not play a important role on Mars.

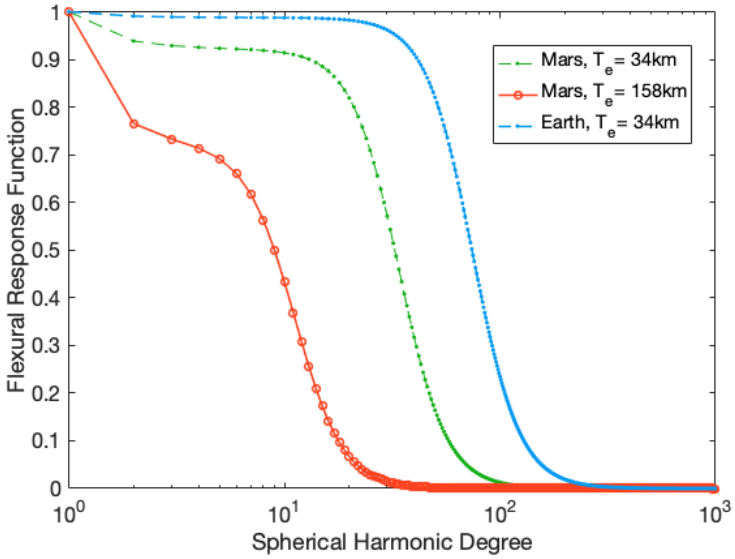

Figure 3.7: Flexural response function as a function of spherical harmonic degree for the thin shell models for both Mars and Earth.

3.1.3. Advanced Isostasy

Classic isostatic equilibrium is reached under the prescription that there are equal mass or pressure at the depth of compensation (Beuthe, 2020). Since classic models of isostasy ignore the shear stresses between the neighboring crustal columns, the loads are supported by buoyancy in classic isostasy. However, regional isostasy considers both flexure and curvature into the model. In this case, the loads are supported by a combination of buoyancy, bending stresses and membrane stresses. The original equal mass/pressure prescription may not be strictly applicable for regional isostasy.

Another prescription which defines the isostatic equilibrium as the state of minimum deviatoric stresses within the lithosphere was mentioned by Jeffreys (1959) and later elaborated by Dahlen (1982) and Beuthe et al. (2012), respectively. Deriving the equations for the ”Minimum Deviatoric Stresses Isostasy” is beyond the scope of this thesis. But knowing this is helpful to the interpretation of results from the FEM models.

3.2. Power Spectra Analysis

One way is investigate the subsurface structure of a planet is to probe a planet from orbit and retrieve information about its topography and gravitational field. Important geophysical parameters can be derived by modelling the relationship between a planet's topography and gravity. For example, many studies (Belleguic et al., 2005, Beuthe et al., 2012, McGovern et al., 2002) modeled the admittance, which is the ratio between gravity and topography in the spectral domain. But this artificial parameter is hard to interpret under the geophysical context.

In this study, power spectrum is used to compare the relationship between gravity and topography (Watts and Moore, 2017). The power spectrum is also called degree variance, which is a tool to express the energy stored in the gravitational field in terms of spherical harmonic degrees or wavelengths. With the relationship between topography and gravity defined in the first place, one can convert the power spectra of topography from different models into the power spectra of gravity. Then, results from different models can be evaluated by comparing the modeled power spectra to the observed one. In this section, the power spectra of gravity anomaly and several topography models are introduced.

3.2.1. Free Air Anomaly

The power spectrum at a given degree n can be calculated by summing up the square of all coefficients, which is given (Kaula, 1967) by

$$\sigma^2(n) = \sum_{m=0}^{n} \{C_{nm}^2 + S_{nm}^2\} \tag{3.30}$$

where C_{nm} and S_{nm} are the spherical harmonics coefficients of gravity. The unit used for power spectra of gravity is mGal^2.

The power spectrum of FAA is used as the observed gravity spectrum because it shows the gravity anomaly in the crust of a planet. To obtain the FAA, gravity reductions mentioned in chapter 2 are required. The FAA power spectrum can be computed from Equation 3.30. However, considering the unit for the gravity power spectrum, the coefficients C_{nm} and S_{nm} are not the Stokes coefficients which describe a planet's mean gravitation potential. Instead, the coefficients in Equation 3.30 should be the spherical harmonic coefficients of certain mass anomalies.

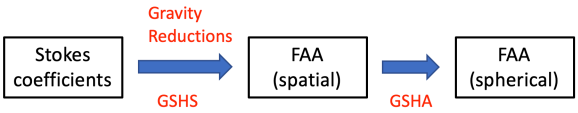

Figure 3.8: Flowchart of the procedure to obtain the spherical harmonics coefficients of FAA.

The first step to get the correct coefficients is to perform both gravity reductions and GSHS to the origin Stokes coefficients. The second step is to extract the radial component of gravitational vectors, which represents the FAA in the spatial domain. The last step is to convert the spatial FAA into the space of spherical harmonic by GSHA, from which the right coefficients for the power spectrum of FAA are derived. This process is visualized in Figure 3.8.

Alternatively, one could apply the following equation to obtain the power spectrum of the gravity anomaly (Pavlis et al., 2012) at a given degree n

$$\sigma^2(n) = \left[\frac{GM}{a^2} \cdot (n-1)\right]^2 \sum_{m=0}^{n} \{\bar{C}_{nm}^2 + \bar{S}_{nm}^2\} \tag{3.31}$$

where g is the gravitational constant, M is the mass of the planet, a is the equatorial radius of the planet, $\bar{C}$ and $\bar{S}$ represent the Stokes coefficients. Equation 3.31 avoids the incommodious procedures of global spherical harmonics transformations, and it is used for the power spectra analysis.

3.2.2. Topography Models

Similar to that of gravity, the power spectrum of topography for spherical harmonic degree n is given (Watts and Moore, 2017) by

$$\sigma^2_{\text{topo}}(n) = \sum_{m=0}^{n} \{T^2_{nm} + Y^2_{nm}\} \tag{3.32}$$

where T_{nm} and Y_{nm} are the spherical harmonic coefficients of a planet's rock equivalent topography.

In the uncompensated topography model, the gravity effect of the topography only depends on mass of topography. The power spectrum of the gravity effect of uncompensated topography model can be calculated from (Kaula, 1967)

$$\sigma^2_{\text{uncomp}}(n) = \left[4\pi G\rho_c \frac{n-1}{2n+1}\right]^2 \sigma^2_{\text{topo}} \tag{3.33}$$

where ρ_c is the mean density of the crust and g is the gravitational constant.

Based on the uncompensated model, the gravity effect of compensated topography can be calculated by incorporating the effect of isostatic compensation into Equation 3.33. For a fully compensated topography under local isostasy, its gravity effect is given (Kaula, 1967) by

$$\sigma^2_{\text{local}}(n) = \left\{4\pi G\rho_c \frac{n-1}{2n+1}\left[1 - \left(\frac{R-D_c}{R}\right)^{n+2}\right]\right\}^2 \sigma^2_{\text{topo}} \tag{3.34}$$

where r is the radius of the planet and D_c is the depth of compensation.

Equation 3.33 and Equation 3.34 give the upper and lower limits of the gravity effect of topography models, respectively. The results from regional (or flexural) compensated models should lie between the limits. For models with regional compensated topography, the power spectra of their gravity effects are given (Watts and Moore, 2017) by

$$\sigma^2_{\text{regional}}(n) = \left\{4\pi G\rho_c \frac{n-1}{2n+1}\left[1 - \Phi(n)\left(\frac{R-D_c}{R}\right)^{n+2}\right]\right\}^2 \sigma^2_{\text{topo}} \tag{3.35}$$

where $\Phi(n)$ is the flexural response function for the infinite plate (Equation 3.7) or the thin shell (Equation 3.28).

An **example** of power spectra analysis **for Earth** (Watts and Moore, 2017) is presented in Figure 3.9. The black points show the power spectrum of Earth's FAA while the coloured points present the power spectra of gravity effects of different topography models.

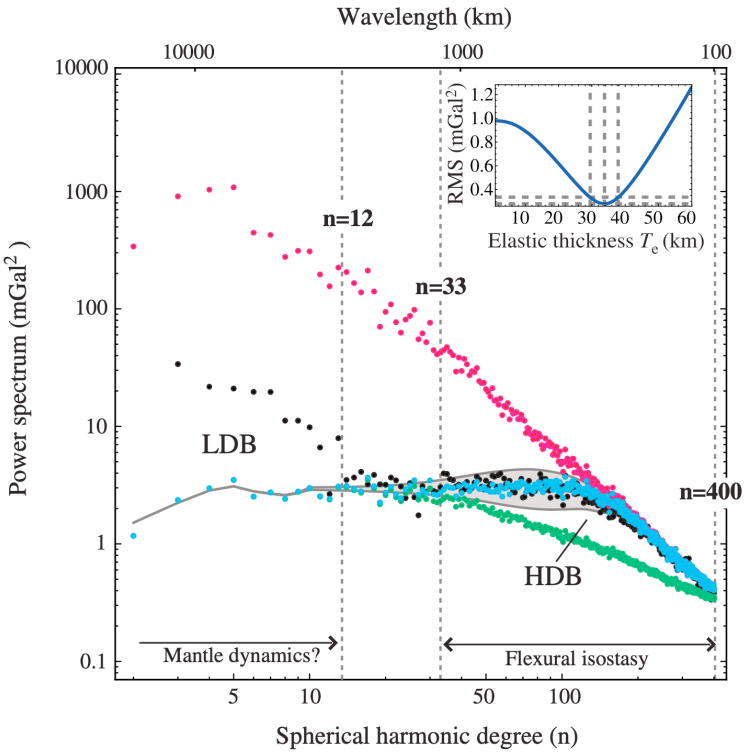

Figure 3.9: Comparison of power spectra between Earth's FAA (black), gravity effects of topography with no compensation (pink), local compensation (green) and regional compensation (blue) (Watts and Moore, 2017). HDB and LDB stands for high degree band and low degree band, respectively.

The uncompensated model (pink) and locally compensated model (green) set the upper and lower limits, respectively. The power spectra of both FAA (black) and regionally compensated model (blue) are between the limits. The observed spectrum fits the power spectrum of infinite plate model better than others. This suggests that the infinite plate model is the best model among the three to represent the behaviour of Earth's crust. However, there are large differences between the modeled and observed spectra at low degree band (LDB), which could be explained by support from mantle dynamics.

The inset at the top right of Figure 3.9 shows how a best lithospheric thickness is found for the infinite plate model. This is done by searching the minimum root-mean-square (RMS) error between the modeled and observed spectra with varying lithospheric thickness. The best fit of $T_e = 34$ km was found for an infinite plate model for Earth by Watts and Moore (2017). Similar approaches are used in this thesis to study the crust of Mars.

4

3D Flat FEM Models for Mars

Having discussed the models of isostasy for Mars, this chapter details how these crustal models are built with FEM. Firstly, an overview of the models created in this study is introduced in section 4.1. Secondly, the generation of the models in Abaqus is discussed in section 4.2. Next, the implementation of different isostatic models are introduced in section 4.3. Lastly, section 4.4 explains how the target regions are selected in this study and how the boundary effect is alleviated.

One of the advantages of the flat Mars model over a spherical Mars model is computational efficiency (Nield et al., 2018). Furthermore, the simple geometry of the flat model makes it easier for trial and error than a spherical one.

4.1. The Software and Model Overview

This section introduces the FEM software package (Abaqus) used in the study. Then, an overview on the 3D flat FEM models for Mars is provided.

4.1.1. The FEM Software

The basic idea behind the FEM is discretization of the actual geometry of the problem by a set of finite elements. Nodes are used to connect these finite elements, and together, they are called the mesh. The tool used for this thesis is Abaqus, which can calculate the displacements of the nodes and derive the stresses as well as strains in every single finite element.

Abaqus is a suite of engineering simulation programs for computer-aided engineering and FEM. One of the most important components of Abaqus is the Abaqus/CAE, which stands for Complete Abaqus Environment(CAE), a graphical and interactive environment for Abaqus. With this powerful interface, users can edit the geometry of the modeled structure and assign relevant properties to it. It is also possible to import CAD models from other software. Abaqus/CAE can mesh the geometry and verify the analysis model.

Once the model is finished, an input file containing the information of the model is generated. Abaqus/CAE hands it over to analysis tools while keeping an eye in the background to control and monitor the job. The major analysis products in Abaqus are Abaqus/Standard and Abaqus/Explicit. The former one is designed for handling static and low-speed dynamic events which demand high-accuracy solutions for stresses. While the latter one is a special-purpose analysis product for high-speed, transient dynamic events such as impact and explosion. Once the analysis is completed, the output database can be processed by Abaqus/CAE or other software.

In short, a full ABAQUS analysis consists of three stages (Figure 4.1): preparation, simulation and evaluation. These stages are performed in sequence and can be implemented in pre-processors like Abaqus/CAE, analysis programs like Abaqus/Standard or Abaqus/Explicit, and software like Abaqus/CAE or Matlab separately.

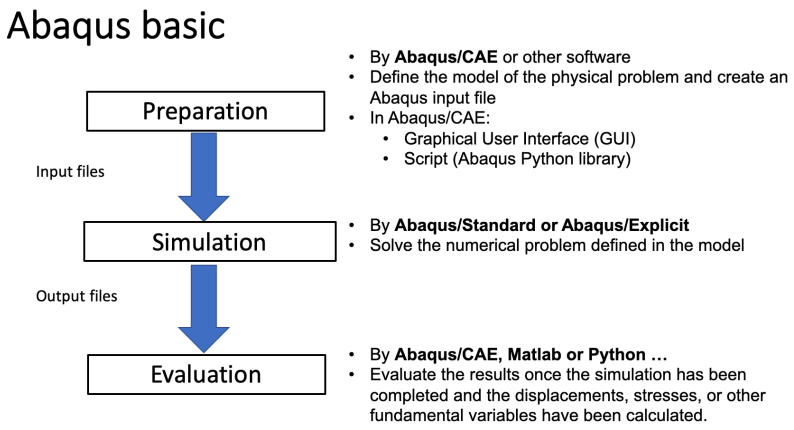

Figure 4.1: The basic procedure for Abaqus.

4.1.2. Model Overview

The high-level overview of the 3D flat FEM model is presented in Figure 4.2 where the inputs, outputs, relevant scripts and software are included. Before the FEM model starts, topography and gravity data is used by `Model.m` to construct different crustal models and generate the surface loads. The `Model_data.py` contains all parameters in the model settings and paths to input files. It should be imported before the generation of the FEM model. The `Model_gen.py` contains all the steps required to construct the model. This file is processed by the Abaqus Python Development Environment (PDE) to extract all the information for model generation. The steps in `Model_gen.py` is elaborated in section 4.2.

The default `Model_data.py` and `Model_gen.py` are designed for a model with uniform thickness and density for each layer. However, incorporating the results from crustal models would bring lateral variations in the crustal density or thickness. So, both `Model_data.py` and `Model_gen.py` are updated in order to incorporate the features of different crustal models from chapter 3. This "update" for the model is elaborated in section 4.3.

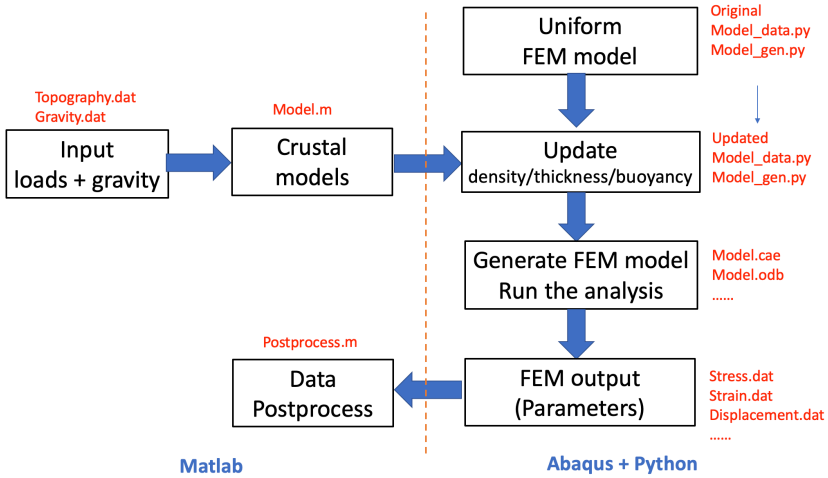

Figure 4.2: A high-level overview of the 3D flat FEM model for Mars. Matlab is used for procedures on left of the orange dashed line while the other procedures are implemented with both Abaqus and Python.

When the model construction is finished, the `Model.cae`, which contains the completed model, is generated. The fact that `Model.cae` can be opened in Abaqus/CAE makes it easy to visualize and change the settings of the model. The `Model.odb` is the output database, which contains all pre-defined parameters from the model. It also can be viewed in Abaqus/CAE and print specified parameters (like `Stress.dat` and `Strain.dat`) from the GUI. The output parameters are further

processed by `Postprocess.m` in Matlab.

Table 4.1: The configuration of the 3D FEM flat model in Abaqus. Parameters like depth of the crust and model size can be modified to fit different regions/models.

Part	**Depth** [km]	**Size** [km]	**Density** [kg/m^3]	**Young's modulus** [N/m^2]	**Poisson's Ratio**	**Mesh Size** [km]
Crust	0-100	3560×3560	2900	5×10^{10}	0.5	40×40
Mantle 1	100-400	3560×3560	3500	1×10^{11}	0.5	90×90
Mantle 2	400-1400	3560×3560	3700	1×10^{11}	0.5	90×90
Core	>1400	-	-	-	-	-

4.2. Model Creation

This section gives a step-by-step introduction to how Abaqus generates the FEM model. Firstly, subsection 4.2.1 introduces the generation of different parts for the flat Mars. Then, the mesh settings are discussed in subsection 4.2.2. Finally, the step and loads are described in subsection 4.2.3.

4.2.1. Part

The flat Abaqus model consists of several individual rectangular parts (Abaqus keyword *Part) simulating the crust and mantle, as shown in Table 4.1. In the default settings, the crustal part has a depth of 100 km and a size of 3560×3560 km, the mantle part has the same size and a depth all the way down to 1400 km, and the core part is not simulated. Instead, the support from the core is simulated by the encastré boundary condition (Abaqus keyword *Boundary), which undertakes all the stress/force from the top parts and fixes the bottom surface of the mantle in terms of both translations and rotations. The crustal part is on top of the mantle parts, and they have different resolution after mesh. So, they are connected by the surface-to-surface tie constraints (Abaqus keyword *Tie). Such tie connections also allow stresses to transfer between the neighboring mesh layers and prevents the surface penetration (Nield et al., 2020).

In Abaqus, no units are shown. So, users should keep the units in a consistent manner. In this study, the standard International System of Units (SI) is used (Table 4.2). However, expressing the the length of the model size (3560 km) in meters would exceed the maximum approximate size limit in Abaqus' geometry engine. To tackle this issue, one could first create the parts with units in km, then scaling the parts by a scale factor of 1000 to convert the unit back to meter.

Table 4.2: Consistent units for Abaqus in this study.

Quantity	Length	Force	Mass	Time	Stress	Energy	Density
Symbol	m	N	kg	s	Pa(N/m^2)	J	kg/m^3

After the parts have been created, assembled, and constrained, different properties are assigned to the parts as shown in Table 4.1. The crust has a density of 2900 kg/m^3 while higher densities of 3500 and 3700 kg/m^3 are assigned to the upper and lower mantle, respectively. The values of Young's modulus for the crustal and mantle parts are 5×10^{10} GPa and 1×10^{11} GPa separately. A Poisson's ratio of 0.5 is shared by both parts to exclude the material compressibility (Van der Wal, 2009). Compressible materials can be indicated by a Poisson's ratio lower than 0.5 but it could bring large instabilities in Abaqus analysis and is hard to fully implemented under surface loads (Wu, 2004). The parameters for viscosity are not defined because this study calculates the state of equilibrium in the model, and time-dependent viscosity does not play an important role in this case. So, only the incompressible elastic material behavior is taken into account in the model.

4.2.2. Mesh

To better study the stress state in the crust, a high resolution mesh with the maximum element edge size of 40×40 km is defined for the crustal part. A relatively coarse mesh of 90×90 km is taken for the

mantle parts. For comparison, a model resolution of 100×100 km was used by Nield et al. (2018) in their area of interest for a flat Earth Glacial Isostatic Adjustment (GIA) model.

Different 3D element shapes are available in Abaqus. They are wedge, tetrahedron, and hexahedron as shown in Figure 4.3. While the hexahedron is sufficient for models with regular geometry, the elements of wedge and tetrahedron are designed to tackle models with complex geometry.

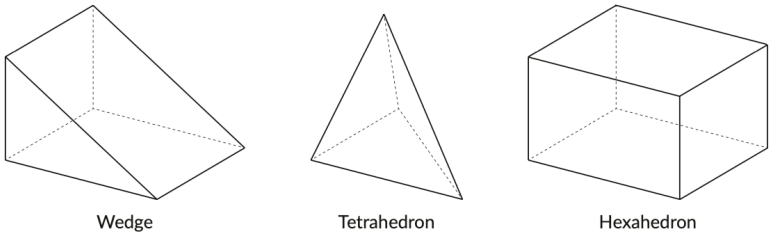

Figure 4.3: Different 3D element shapes in Abaqus (Casteren, 2018).

The mesh element type used in this study is C3D8H, which indicates that it is a continuum hybrid element with 8 nodes. For a flat model with cuboid parts, the brick element is sufficient to generate the mesh. The use of this simple mesh element also ensures the convergence and accuracy of the model. The hybrid element is selected to avoid the singularity due to the incompressible material (Van der Wal, 2009).

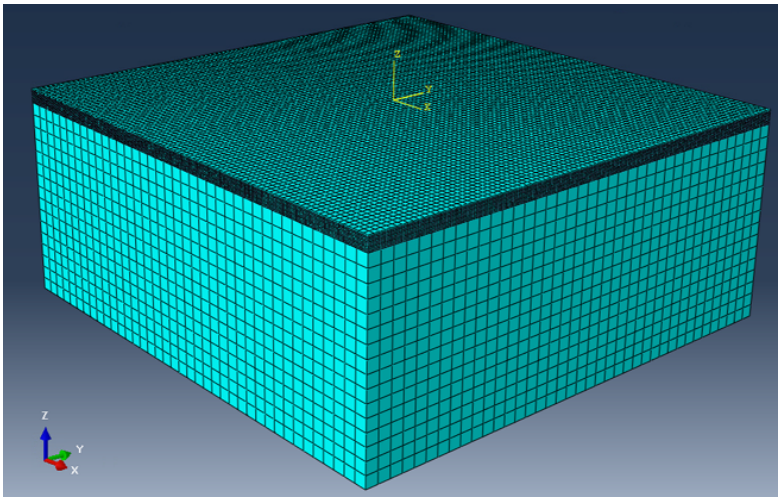

Figure 4.4: The mesh of the 3D flat Mars model. The crust at the top is covered by fine mesh while the mantle is with coarse mesh.

4.2.3. Load and Step

In order to model the crust of Mars, both the crustal structure and the topography need to be taken into account. The implementation of crustal model in the Abaqus is discussed in section 4.3, and this subsection covers the settings of the loads and step.

To apply surface loads on a planet, the time steps need be defined to determine how long the surface loads are working in the model. For example, to model the GIA on Earth, multiple steps are defined with time-varied ice loads on the surface by many studies (Casteren, 2018, Nield et al., 2020). It can be done for the Earth because there is historical ice loading data available. But for Mars, the loading history of either ice or topography is not available. So, instead of using the multiple time steps and changing the surface loads with time, only one step and fixed surface loads are used.

The only step used in the model is the **geostatic step** (Abaqus keyword *Step). With the geostatic step, the model can generate a geostatic stress field which supports the surface loads. This step would not stop until the generated stress field is in equilibrium with the applied loads and boundary condition in the model. With the geostatic step, it is possible to model the lithosphere of Mars under loads without

inputting any time information. However, the geostatic step also assumes that the lithosphere Mars is in equilibrium with its surface loads. Though this assumption may not represent what really happens on the red planet, it fits the idea of isostatic equilibrium and could reveal information on how deviatoric buoyancy and stresses play roles in supporting the surface loads.

The surface loads of Mars are converted from topographic height h into pressure p by

$$p = \rho_c g h. \tag{4.1}$$

Then, the topographic pressure field is mapped on the surface of the flat model (Abaqus keyword *Load). Figure 4.5 shows how a circular positive load is mapped on the surface of the flat model. The load is represented by the pink arrows. These arrows are pointing downward, which means that the topography is positive and brings extra mass on the surface. The lengths of the arrows are determined by the magnitude of the loads.

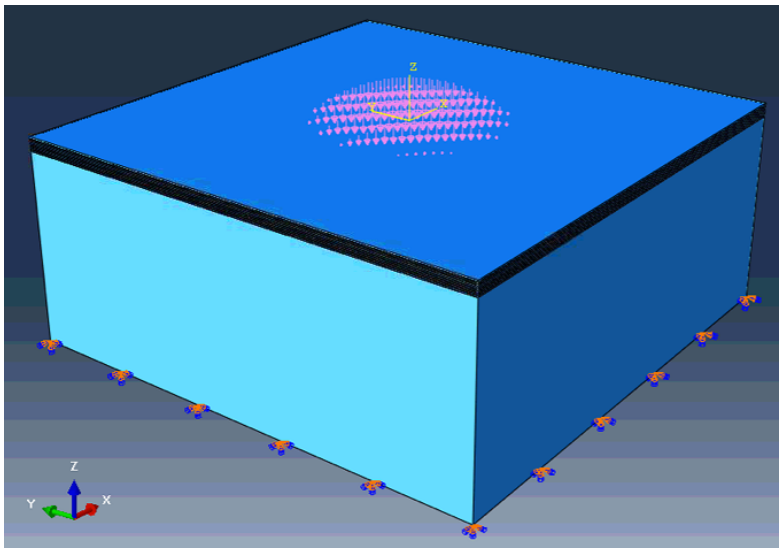

Figure 4.5: A sample circular load (pink arrows) with varying heights on top of the 3D flat Mars model. The encastré boundary condition is visible at the bottom of the model.

After the loads and steps are defined in Abaqus, a job can be created for the model. In the job definition, the model name, analysis type, memory usage, and number of CPUs can be specified. The analysis process initiates once the job is submitted. But in this study, isostatic models should be incorporated into the FEM model before creating the job. This is discussed in the next section.

4.3. Implementation of Isostasy

The models of isostasy discussed in chapter 3 require lateral variations in either crustal thickness or crustal density. The purposes behind the spatial variations in thickness or density are to alter the distribution of buoyancy at the crust-mantle boundary and maintain the isostatic equilibrium. Such isostatic restoring forces are implemented in Abaqus as elastic foundations or Winkler foundations (Abaqus keyword *Interaction) at the material boundaries (Wu, 2004). To create the elastic foundation, the stiffness with a value equal to $\Delta\rho g$ has to be defined for each boundary layer. By doing so, it also means that the buoyancy is uniform at the material boundary.

In this thesis, the gravity of the crust and the mantle is neglected. The motivations are: firstly, to simplify the model and make the solution converge quicker in Abaqus; secondly, to study the effect of the loads only; lastly, to compute the nonhydrostatic stress state in the lithosphere. As a result, the buoyancy at the interface between the crust and heavier mantle should correspond to the applied loads only. Such topography-related buoyancy is called deviatoric buoyancy in this study, as it excludes the effect of the body forces from the crust and the mantle.

The deviatoric buoyancy has lateral variations at the material boundary, and such spatial variations cannot be achieved by the elastic foundations in Abaqus. Instead, it is calculated directly and loaded as pressure at the crust-mantle boundary in the flat Mars model. Since the deviatoric buoyancy can be implemented without the elastic foundations, the flat Mars model is further simplified by neglecting the lateral variations in density (for Pratt) and thickness (for Airy). This assumption would not affect the results of this study as the variations in crustal thickness only play an important role in terms of the short-wavelength deformation (Nield et al., 2018).

4.3.1. Local Isostasy

In the Pratt's model, a uniform depth of compensation D_c is assumed, and the buoyancy is distributed on the same boundary layer but with different magnitudes (due to the different heights of the loads). The basic equation for the Pratt's model is Equation 3.6, which shows how the density of each crustal column ρ varies due to the topography height h. In this case, the deviatoric buoyancy dP depends on the density difference between the mean density ρ_0 and the crustal density ρ from Equation 3.6, the gravity of the planet g, and the depth of compensation D_c

$$dP_{Pratt} = (\rho_0 - \rho) g D_c \tag{4.2}$$

where the positive pressure is upwards (push) and negative one is downwards (pull). The implementation of Pratt's model can be visualized in Figure 4.6.

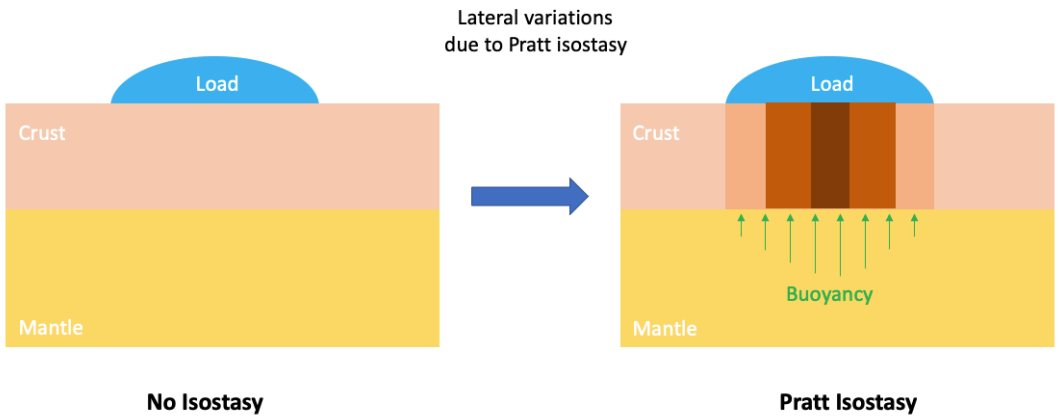

Figure 4.6: The illustration of the implementation of Pratt's model in Abaqus. The applied load (blue) brings density variations in the crust. The darker the color is, the larger the density variation is. A larger density variation also brings larger buoyancy (green arrows) at the boundary. The deviatoric buoyancy is only added under the load.

The Airy's model is harder to implement in Abaqus than the Pratt's model. Because in the Airy's model, the deviatoric buoyancy has to be distributed at different layers due to the variations in crustal thickness. Thus, the crustal part in the flat model is further divided into 10 or more layers, which

provides surfaces at different depths to load the buoyancy in the Abaqus. This process is called discretization (Figure 4.7). More layers in the discretization could increase the accuracy of the model. But the computation time is also proportional to the number of crustal layers. In practice, 10 to 20 layers for the crustal part could balance the computational accuracy and efficiency for the model. The buoyancy anomalies at various depths are calculated by

$$dP_{Airy} = (\rho_m - \rho_c)gr \tag{4.3}$$

where r is the variation of crustal thickness due to Airy's isostasy from Equation 3.5.

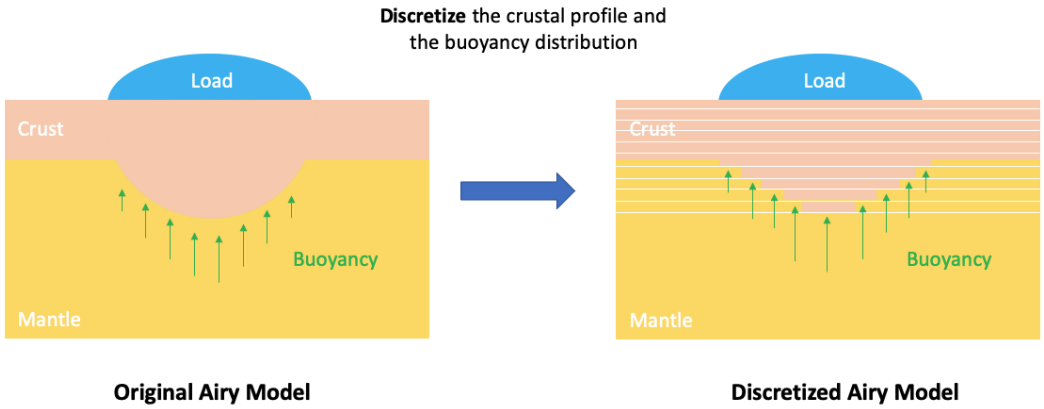

Figure 4.7: The illustration of the implementation of Airy's model in Abaqus. The continuous crust-mantle boundary is divided into multiple layers so that the buoyancy (green) can distribute at different depths. The deviatoric buoyancy is only added under the load.

4.3.2. Flexural Isostasy

Since the models of flexural isostasy are based on the crustal profile from the local isostasy, the implementation of flexural isostasy in the flat Mars model is the same as that of the isostasy.

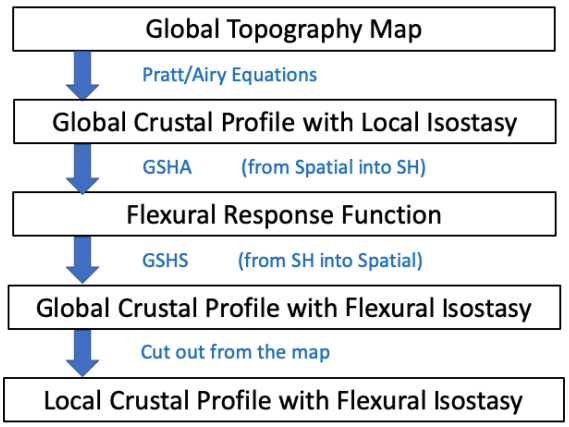

Figure 4.8: The flowchart to generate crustal profiles with flexural isostasy.

The crustal profiles from flexural isostasy can be obtained by Equation 3.29 with flexural response functions introduced in chapter 3. This process is elaborated in Figure 4.8 with four steps. Firstly, a global crustal profile based on local isostasy with the topography data as input is needed. The crustal profile can be either a global crustal density distribution from the Pratt's model or a crustal thickness map from the Airy's model (both are used as shown in Figure 4.10). Secondly, a GSHA is needed to transform the global crustal profile from spatial domain into spherical harmonic domain. Equation 3.29 is used at this step to filter the coefficients at each degree. The third step is to transform the new crustal

profile from spherical harmonic back to space with a GSHS. This step generates a global crustal profile with flexural isostasy. Lastly, the regions of interest are extracted from the global crustal map and applied to the flat model.

Two examples are given to illustrate how the flexural isostasy would filter the crustal profiles. The first one is a simple loading case with two circular loads, as shown in Figure 4.9. The crustal profiles based on local and flexural models of isostasy for the two loads are presented in Figure 4.10 in a global scale.

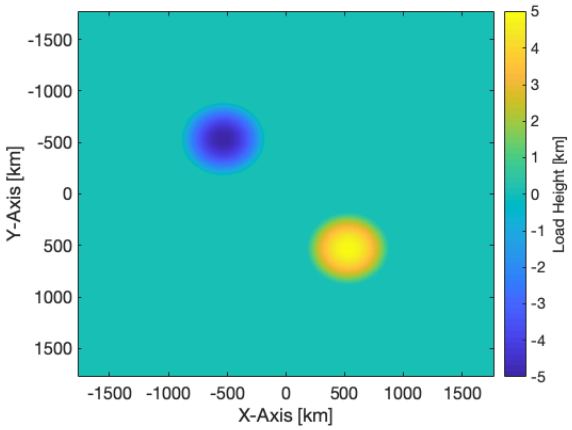

Figure 4.9: Simple surface loads with both positive (+5 km) and negative (-5 km) topography. The heights of the loads decrease/increase parabolically to zero. Both loads have a radius of 354 km.

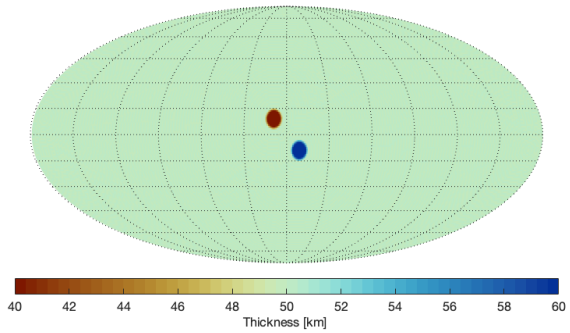

(a) Crustal thickness with the Airy's Model.

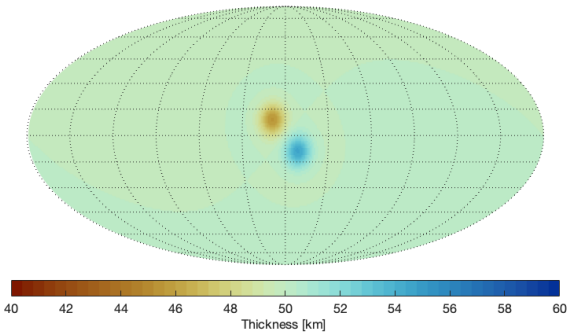

(b) Crustal thickness with the thin shell model (based on the Airy).

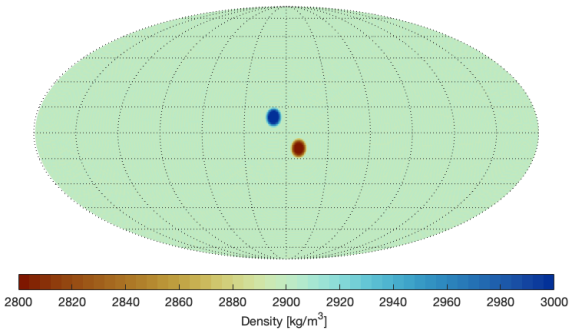

(c) Crustal density with the Pratt's Model.

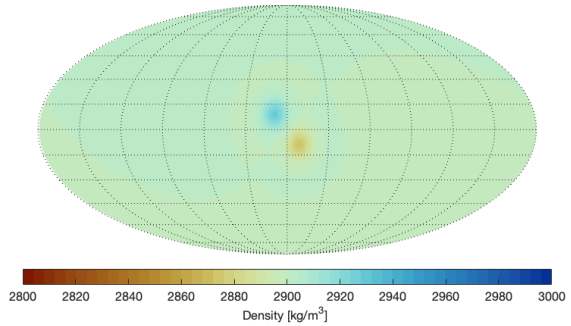

(d) Crustal density with the thin shell model (based on the Pratt).

Figure 4.10: Global crustal profiles for the sample loads (Figure 4.9) under Airy(a), Pratt(c) and their corresponding thin shell models(b+d). The Airy's model assumes a mean crustal thickness of 50 km, a crustal density of 2900 kg/m^3 and a mantle density of 3500 kg/m^3. The Pratt's model takes a mean crustal density of 2900 kg/m^3 and a compensation depth of 100km. The thin shell model has an elastic thickness of 158 km. All images are presented using a Mollweide projection.

The average crustal thickness for the Airy's model is 50 km. While the negative load makes the

crust thinner, the positive load increases the crustal thickness (Figure 4.10a). Such opposite behaviors can also be found in the density variations caused by the loads in the Pratt's model (Figure 4.10c). The flexural isostasy includes the support from elastic stresses, which makes the spatial variations of thickness or density increase in size but decrease in magnitude (Figure 4.10d and Figure 4.10b). The results are consistent with Figure 3.2 from David (2010).

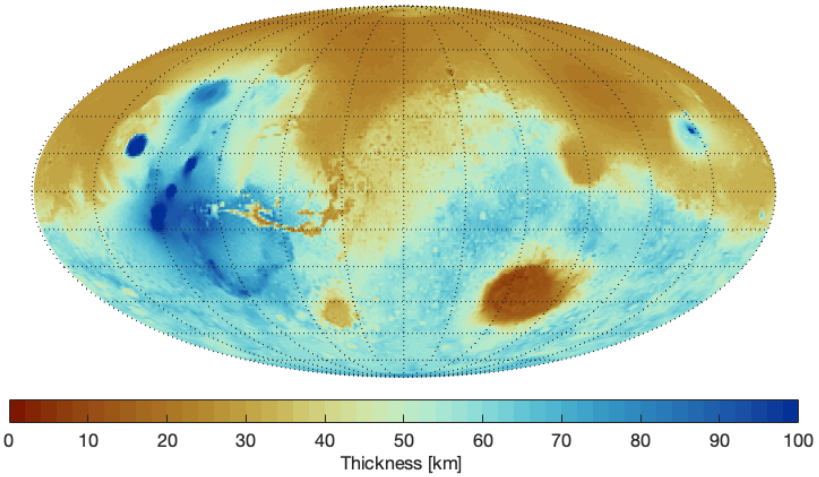

(a) Crustal thickness for Mars with Airy's model.

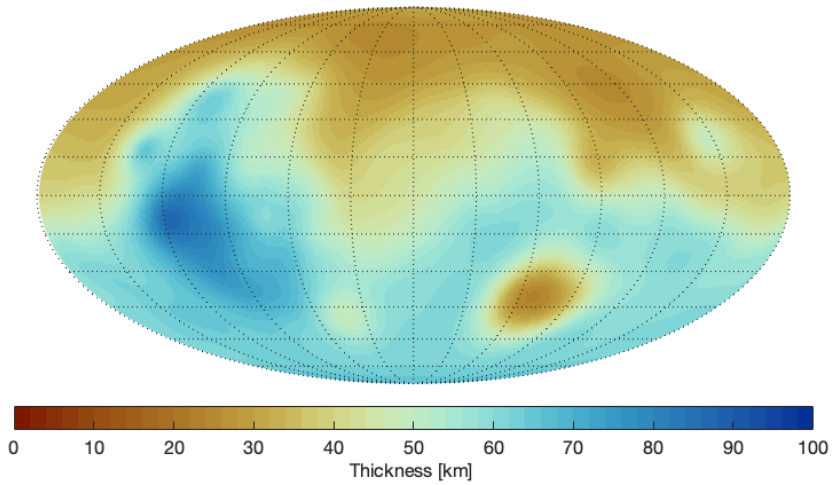

(b) Crustal thickness for Mars with the thin shell model (based on Airy).

Figure 4.11: Global crustal thickness profiles for Mars with local(a) and regional(b) isostasy. The Airy's model uses an average crustal thickness of 50 km, a crustal density of 2900 kg/m^3, and a mantle density of 3500 kg/m^3. The thin shell model takes an elastic thickness of 158 km. Both images are presented using a Mollweide projection with a central meridian of 0° longitude.

The second example (Figure 4.11) shows how the thin shell model changes the crustal thickness profile from the Airy's model. The crustal thickness profile from local isostasy is highly related to the topography, and short-wavelength (high-degree) features are clearly visible in Figure 4.11a. But the flexural isostasy works like a low-degree-pass (or long-wavelength-pass) filter and smooths out all short-wavelength features. Only the effects from long-wavelength features, like the global dichotomy, Tharsis Rise, and Hellas Basin, remain in Figure 4.11b.

4.4. Target Regions

The flat Mars model is designed to conduct regional analysis. This section explains how the regions of interest are selected in subsection 4.4.1 and how the boundary effects are reduced in the flat models in subsection 4.4.2.

4.4.1. Selection

The regions of interest in this study are the Tharsis Rise, Hellas Basin, and Utopia Basin. The Tharsis Rise and Hellas Basin, together with their neighboring regions are selected because they are the most prominent features on the surface of Mars except the global dichotomy. While the Olympus Mons reaches a height up to 21 km, the Hellas Basin goes down to 7 km deep. They are good examples as positive and negative topographic loads for the 3D flat Mars model.

The number of faults distributed over the regions is also a significant criterion. As shown in Figure 4.12, both the Tharsis region and the Hellas Basin are the home to young faults with age less than 3.5 Gyr. In addition, a large number of both extensional and compressional faults are located around the Utopia Basin (and Elysium Mons), which is selected as the third region of interest. This region is more complex than the previous two because it not only has large positive and negative topographic features but also contains the boundary of the global dichotomy.

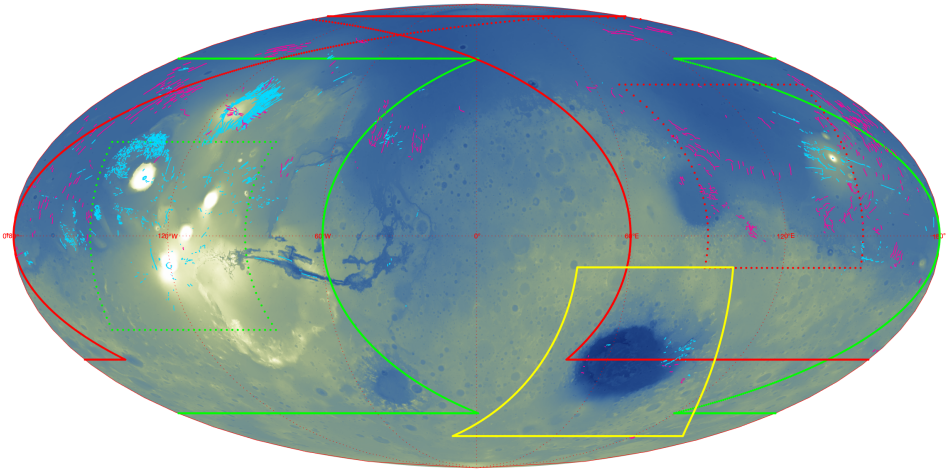

Figure 4.12: Regions of interest (green:Tharsis, red:Utopia, yellow:Hellas) with extensional (neon blue) and compressional (neon pink) faults younger than 3.5 Gyr. The image is presented using a Mollweide projection with a central meridian of 0° longitude. Rectangular boxes are distorted due to projection.

The default size of the flat model is 3560×3560 km, which is depicted by the green dotted-line box, red dotted-line box, and yellow solid-line box in Figure 4.12. However, for Tharsis and Utopia, the default size is not large enough to cover the major features and faults. So, the size for these two region is extended to 7120×7120 km. After model extension for the Tharsis and Utopia, major faults on the surface of Mars are covered in these three regions, as shown in Figure 4.13.

Table 4.3: An overview of the regions of interest. These regions are highlighted in Figure 4.13.

Region	Center	Size
Tharsis Rise	0° N, 120° W	7120×7120 km
Utopia Basin	20° N, 120° E	7120×7120 km
Hellas Basin	40° S, 70° E	3560×3560 km

An overview of the reigons of interest is presented in Table 4.3. Since these regions are shown in the Mollweide projection in both Figure 4.12 and Figure 4.13, plots with equidistant projection for the regions are shown in Figure 4.14. It shows how the regions look like in the flat model.

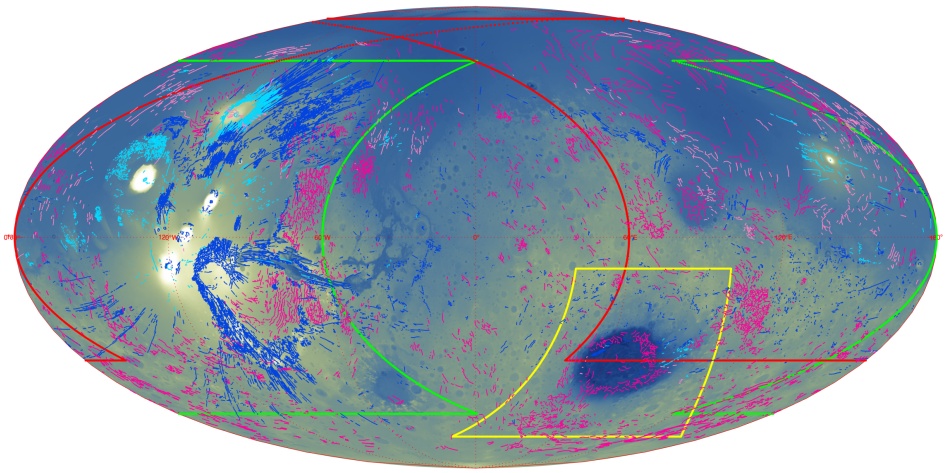

Figure 4.13: Regions of interest (green:Tharsis, red:Utopia, yellow:Hellas) with extensional (blue) and compressional (pink) faults. The faults younger than 3.5 Gyr are colored with neon blue (extensional) and light pink (compressional). The image is presented using a Mollweide projection with a central meridian of 0° longitude.

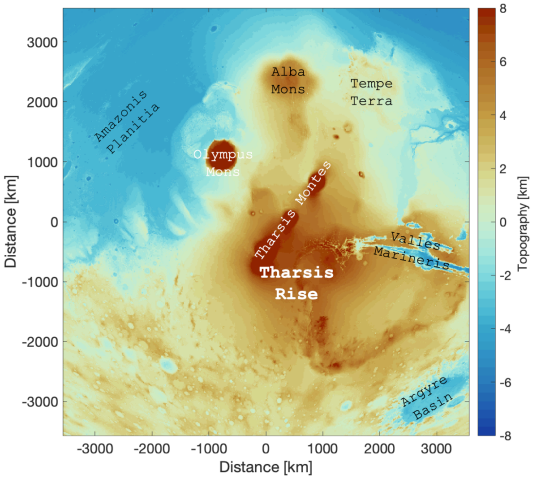

(a) Tharsis Rise.

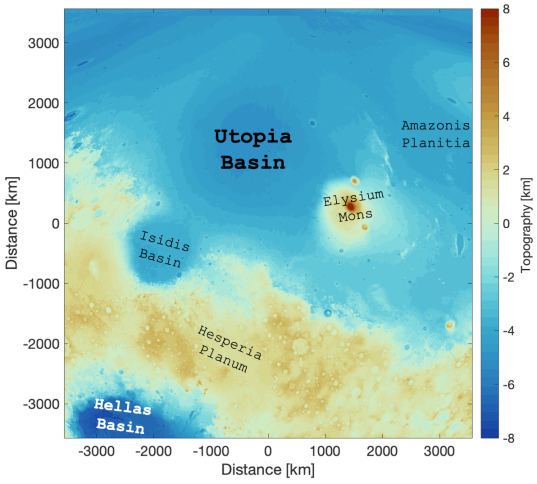

(b) Utopia Basin.

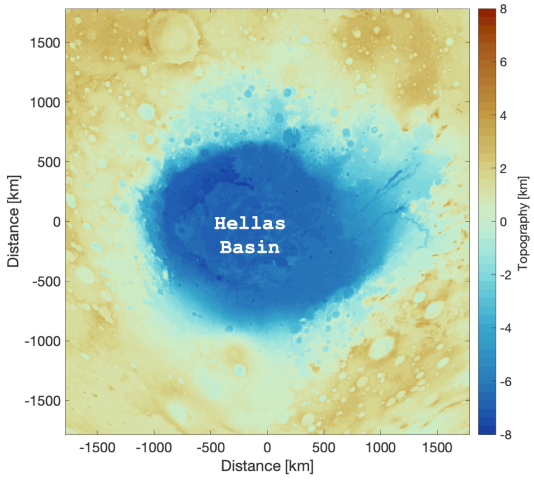

(c) Hellas Basin.

Figure 4.14: The topography of regions of interest in equidistant projection.

4.4.2. Boundary Effect

Since the flat Mars model is not infinite, the boundary might have a impact on the region of interest. A common practice to make sure the boundary effects are negligible is to extend the model. For example, to study a 3500×4500 km region of interest, Nield et al. (2018) used a flat model with a total width of 60000 km. It is true that the larger the model is, the less boundary effect would be. But it also comes with the price of computation time. Therefore, it is necessary to find a balance between boundary effect reduction and computational efficiency.

To find such a balance, the default model size (Table 4.3) is extended up to 2.5 times as shown in Figure 4.15. The results from different models are compared to determine the minimum extended size to alleviate the boundary effects.

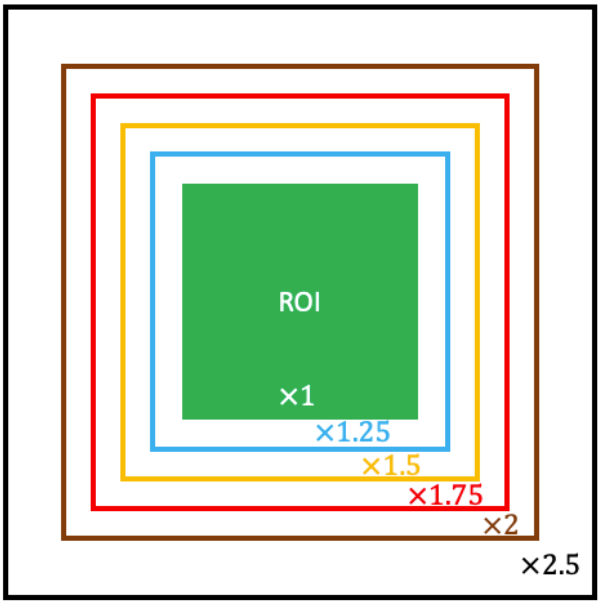

Figure 4.15: An illustration of the extended models to study the boundary effects. The original region of interest is shown in green, and the extended models are with different colors. ROI stands for region of interest.

Taking the Tharsis Rise region for example, the differences in the magnitude and direction of the maximum principal stresses for different extended models are presented from Figure 4.16 to Figure 4.19. Large boundary effects can be observed in Figure 4.16 in terms of both magnitude and direction for the original ×1 model. Figure 4.17 shows that the boundary effects are largely reduced as the model size increases to ×1.25. In Figure 4.18 and Figure 4.19, the effects of the boundary are not visible, and the sporadic differences in both magnitude and direction plots are attributed to interpolation errors from post-process. Similar results are obtained for the Utopia Basin and Hellas Basin, which can be found in Appendix B.

In summary, by extending the model to 1.25 times of the original one, the boundary effects can be reduced significantly. Though the ×1.25 model appears to be sufficient, a safer choice is the ×1.5 model which is selected for this study to ensure the boundary does not affect the regions of interest.

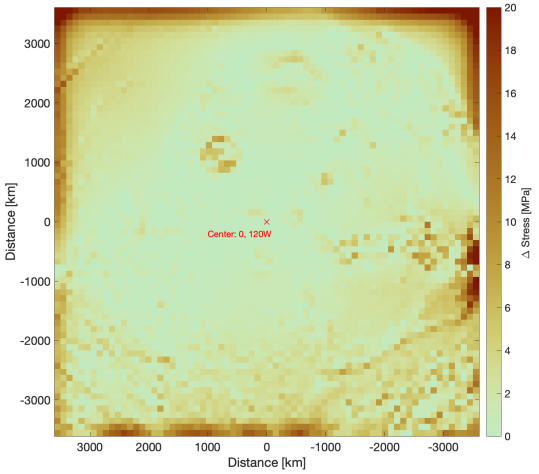

(a) Difference in the magnitude of maximum principal stresses.

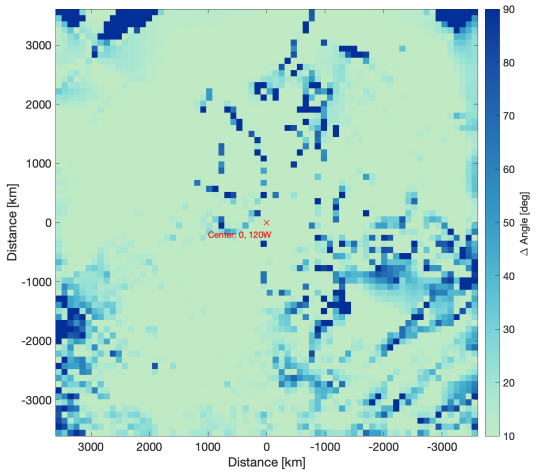

(b) Difference in the direction of maximum principal stresses.

Figure 4.16: The difference in the magnitude and direction of the maximum principal stresses between the ×1 and ×1.25 models.

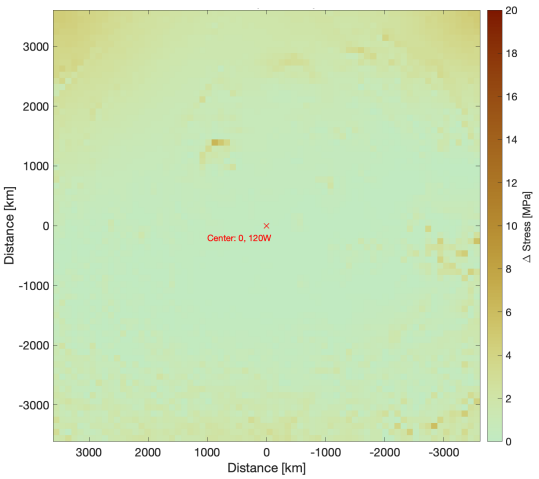

(a) Difference in the magnitude of maximum principal stresses.

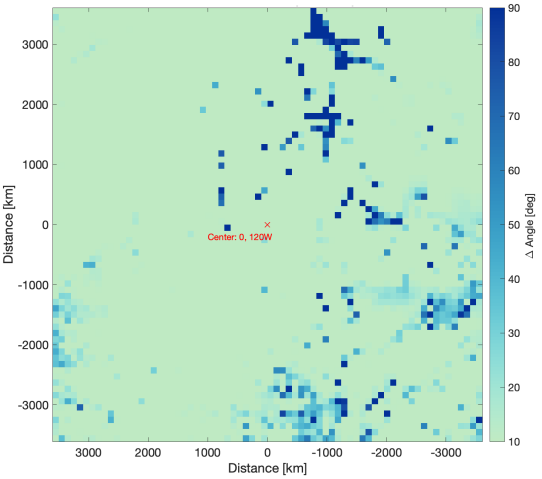

(b) Difference in the direction of maximum principal stresses.

Figure 4.17: The difference in the magnitude and direction of the maximum principal stresses between the ×1.25 and ×1.5 models.

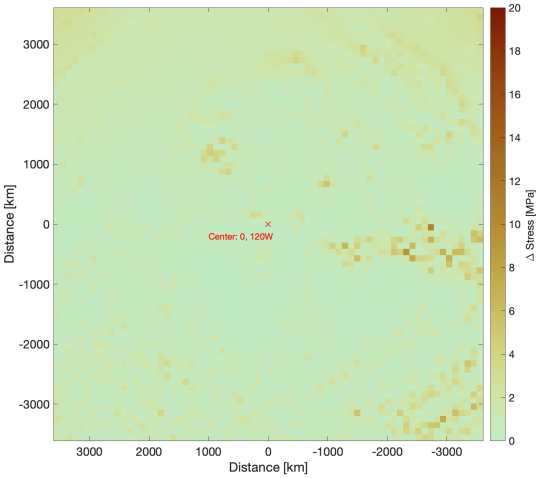

(a) Difference in the magnitude of maximum principal stresses.

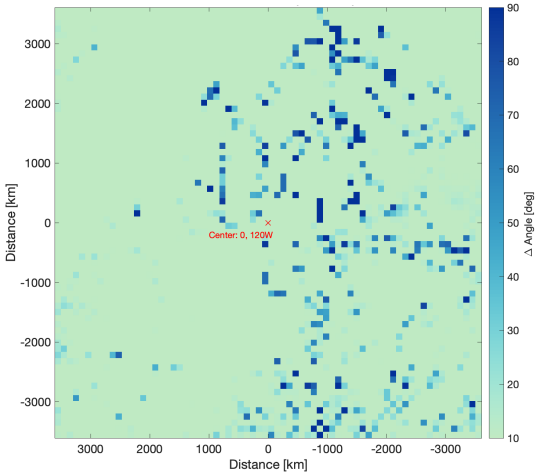

(b) Difference in the direction of maximum principal stresses.

Figure 4.18: The difference in the magnitude and direction of the maximum principal stresses between the ×1.5 and ×1.75 models.

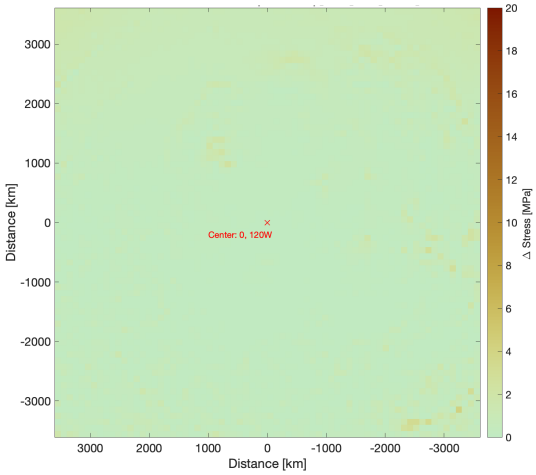

(a) Difference in the magnitude of maximum principal stresses.

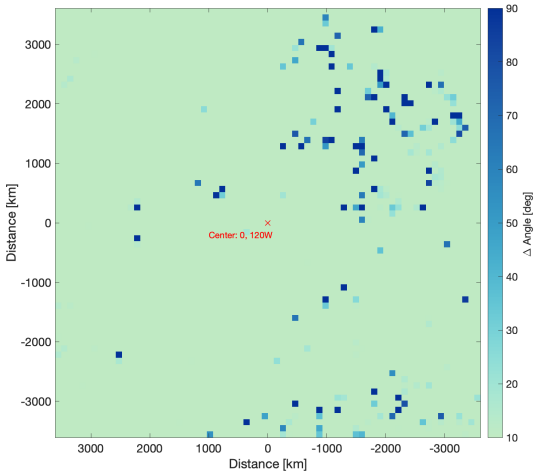

(b) Difference in the direction of maximum principal stresses.

Figure 4.19: The difference in the magnitude and direction of the maximum principal stresses between the ×1.75 and ×2 models.

4.4.3. Plume Modeling

The Tharsis rise represents the most prominent gravity Figure 2.3 and topography Figure 2.1 anomalies on Mars. Previous studies (Redmond and King, 2004, Zhong, 2002) suggest that the Tharsis region is mainly supported by the flexure of the lithosphere and partly by a deep mantle plume. Van der Tang (2021) modeled such a mantle plume under the Tharsis rise and found that the best-fitting (to gravity anomaly) plume was at the depth from 800 km to 900 km with a density anomaly of 400 kg/m^3.

A proper way to model such a mantle plume is to change the density (and other relevant parameters) of the plume region in the FEM model and simulate the plume with time-dependent steps. But it would take too much time to create and run such a model. Instead, this study simulates the effect of the mantle plume under the Tharsis rise by modeling the pressure induced by the plume. In the FEM model, pressure is loaded at the crust-mantle boundary. So, plume modeling is also referred to as bottom loading.

Since the magnitude of the pressure is unknown, the pressure with different orders of magnitude (10 MPa, 100 MPa, 1000 MPa, 10000 MPa) is loaded in the FEM model separately to investigate the effects of bottom loading. Figure 4.20 shows how the pressure distributes at the crust-mantle boundary with the maximum pressure of 10 MPa.

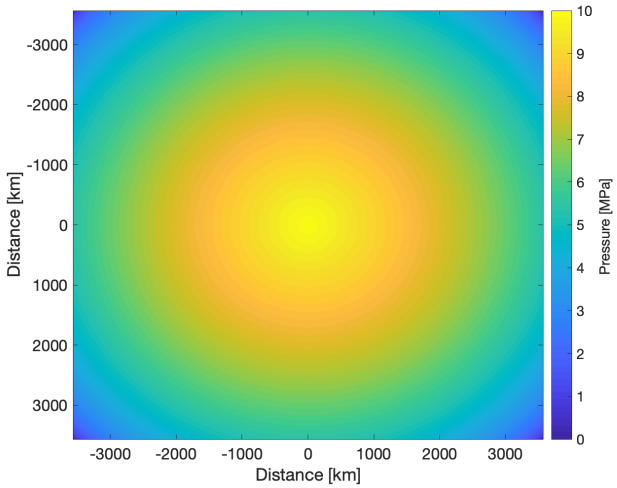

Figure 4.20: The bottom load (pressure) at the crust-mantle boundary to simulate the effect of a mantle plume under the Tharsis region. The maximum pressure is at the center, and the pressure decreases parabolically to zero at the edges.

5

Verification and Validation

This chapter presents the verification and validation on the data (section 5.1), power spectrum analysis (section 5.2), and the FEM model (section 5.3). Results from literature are used to verify and validate the data and methodologies in the first two sections. The FEM model is validated with a series of simple modeling cases.

5.1. Data

In this section, the power spectra of both topography (MOLA) and gravity (GMM-3) data are compared to that of referenced data from literature. Similarities and differences between the data are discussed.

5.1.1. Topography

The topography data used in this study is downloaded from the NASA PDS site as mentioned in chapter 2. It is the difference between the shape (or radius) of the planet and the areoid. To validate this topography data from MOLA, its power spectrum is compared to that of the MarsTopo2600 shape model from Wieczorek (2015) in Figure 5.1. The power spectra of both MOLA and MarsTopo2600 fit very well in the first 110 degrees except for the degree two. The large deviation at degree two may attribute to the consideration of the oblateness of the planet. The MarsTopo2600 is a shape model which would contain the effect of the oblateness in its degree-two terms. However, the MOLA is a topography model where the effect of the oblateness is lessened.

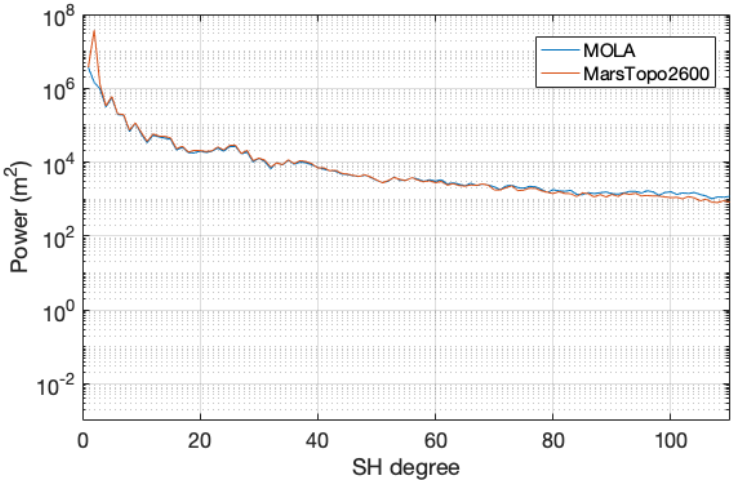

Figure 5.1: Power spectra of the topography of Mars for MOLA (blue) and MarsTopo2600 (red). The larger difference at degree two is due to the oblateness of the planet.

Figure 5.2 presents the power spectrum of MarsTopo2600 by Wieczorek (2015). It is used to verify

that the power spectrum of MarsTopo2600 in Figure 5.1 is plotted correctly.

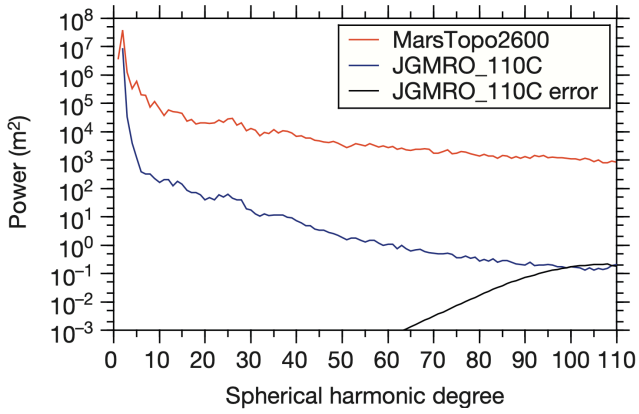

Figure 5.2: Power spectra of the topography (MarsTopo2600), geoid (JGMRO 110C), and geoid error by Wieczorek (2015). Only the MarsTopo2600 is used for verification in this study.

5.1.2. Gravity

The gravity data of Mars (GMM-3) is used in this study for the power spectra analysis in chapter 3. To verify that the correct gravity dataset is used, the square root of the potential power of the stokes coefficients and its uncertainties from GMM-3 dataset are calculated by Equation 2.3 and shown in Figure 2.2.

The square root of potential power of GMM-3 is shown in blue in Figure 2.2 and green solid line in Figure 5.3. That of the GMM-3's uncertainties are plotted in red in Figure 2.2 and green dashed line in Figure 5.3. The patterns of both GMM-3 and its uncertainties are consistent in Figure 2.2 and Figure 5.3, which suggests the correct gravity data is used. The verification and validation of the gravity data itself has been done by Genova et al. (2016) and Van der Tang (2021).

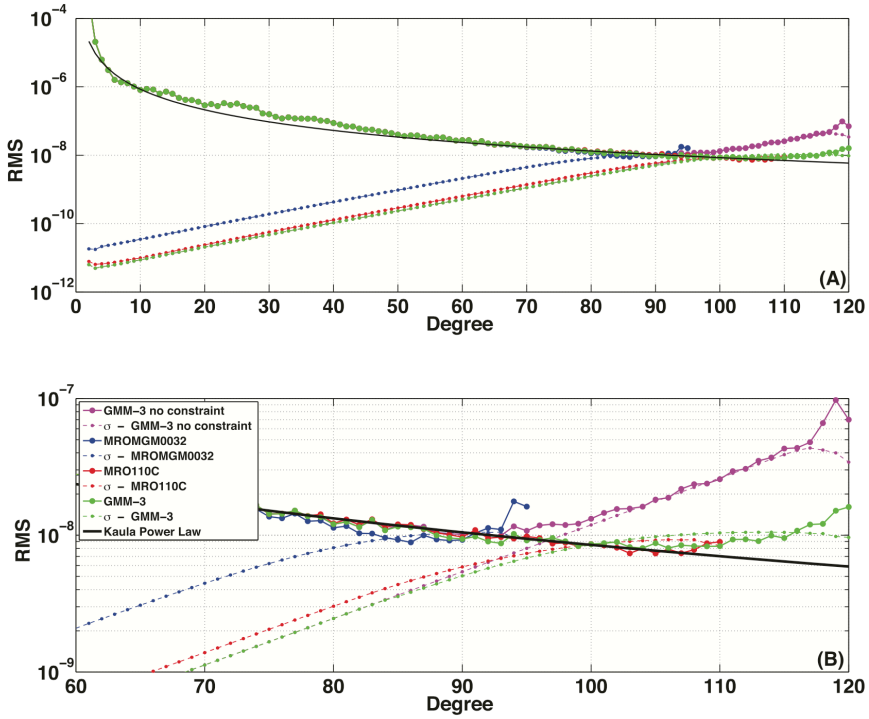

Figure 5.3: The square root of potential power (A) and higher degree spectra (B) of the GMM-3, MRO110C, and MROMGM0032 solutions and relative formal uncertainties from Genova et al. (2016). The GMM-3 (green) in this figure is used for verification.

5.2. Power Spectra Analysis

In this section, both Fig.1 and Fig.3 from Watts and Moore (2017) are reproduced. With the same input data and equations, Fig.3 is remade successfully, but some differences are found between the remade Fig.1 and the original one. The issue with Fig.1 is elaborated in this section.

5.2.1. Reproduction of Fig.3 from Watts and Moore (2017)

To verify the scripts used for the power spectra, Fig.1 and Fig.3 from Watts and Moore (2017) are reproduced. The topography data is from the Earth2014 Rock Equivalent Topography model[1]. All equations and parameters are the same as those from Watts and Moore (2017). These equations are also discussed in chapter 3.

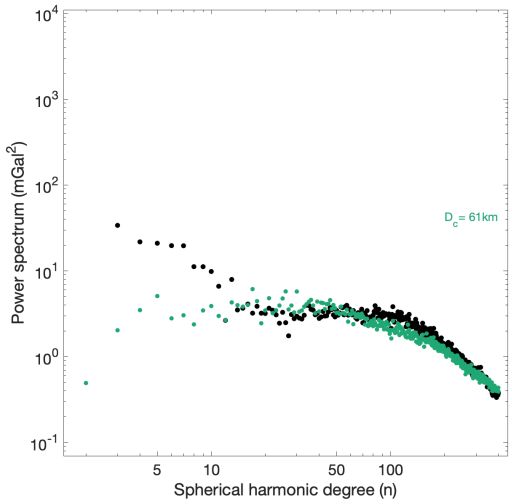

(a) The calculated spectrum based on the gravity effect of the topography and its Airy compensation (green) with a D_c of 61 km. The topography data is from Earth2014 Rock Equivalent Topography (RET) model.

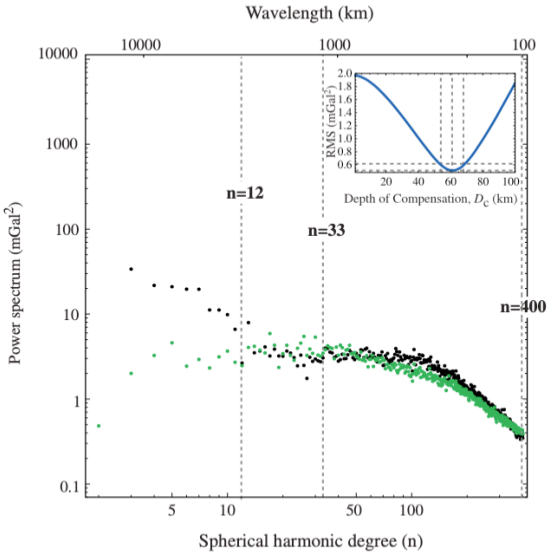

(b) Comparison of the power spectrum of Earth's FAA field (black) to the calculated spectrum based on the gravity effect of the topography and its Airy compensation (green) with a Dc of 61 km (Watts and Moore, 2017).

Figure 5.4: Comparison of the power spectrum of the gravity effect of the topography and its local compensation with a D_c of 61 km.(a) shows the plot from this study and (b) is Fig.3 from Watts and Moore (2017).

Figure 5.4a compares the power spectrum of observed Earth gravity anomaly and that of the gravity effect of the topography and its local compensation with a D_c of 61 km. The spherical harmonic coefficients from the EGM2008 gravity model (Pavlis et al., 2012) is used. The power spectrum of the gravity anomaly is calculated with Equation 3.31. The Earth2014 Rock Equivalent Topography model (Rexer and Hirt, 2015) is used as input topographic data.

Figure 5.4b is taken from Watts and Moore (2017), which does the same as Figure 5.4a. It can be seen that both subplots in Figure 5.4 match with each other. This visual inspection confirms that the code used for the power spectra analysis is correct.

Fig.3 from Watts and Moore (2017) is reproduced and discussed in the above. By doing so, it is sufficient to verify the code used for power spectra analysis in this study. With verified spectral analysis code, Fig.1 from Watts and Moore (2017) is also reproduced. But readers should keep in mind that the content on the next page **does not serve as** verification and validation because the results are not the same as the original paper. The differences are discussed in the following to raise questions about Fig.1 from the original paper.

[1] http://ddfe.curtin.edu.au/models/Earth2014/ [25-06-2021]

5.2.2. Reproduction and Discussion of Fig.1 from Watts and Moore (2017)

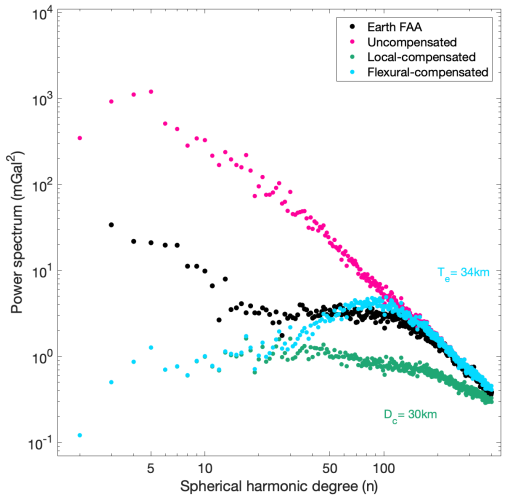

(a) The reproduced Fig.1 with verified code in this study.

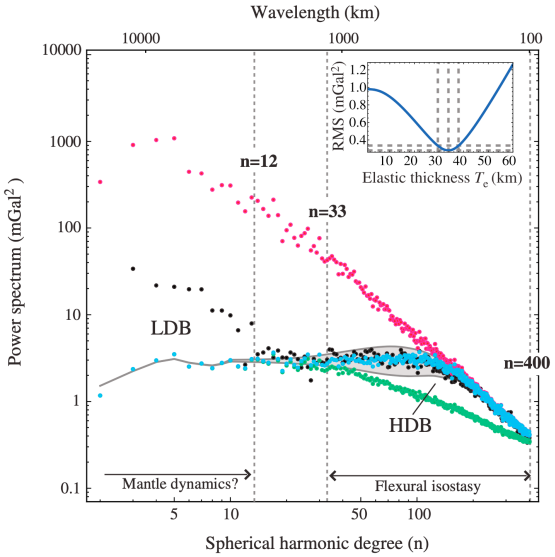

(b) The original Fig.1 from Watts and Moore (2017).

Figure 5.5: Comparison of power spectra between Earth's FAA (black), gravity effects of topography with no compensation (pink), local compensation (green) and flexural compensation (blue). (a) is the figure reproduced in this study. (b) is Fig.1 from Watts and Moore (2017). The values for parameter used in (a) are taken from Watts and Moore (2017). The power spectra of both local-compensated and flexural-compensated topography overlap in the low-degree band.

Figure 5.5a is meant to reproduce Figure 5.5b, which compares the power spectrum of Earth's gravity anomaly to those of Earth's topography with no compensation, local compensation, and flexural compensation. As seen in Figure 5.5, the power spectra of both Earth FAA (black) and the gravity effect of uncompensated topography (pink) match in both subplots. Firstly, the same pattern for Earth's FAA is seen in Figure 5.4, and this is confirmed here. Secondly, the match of the power spectra of uncompensated topography in both Figure 5.5a and Figure 5.5b proves that the equations and code used for topography without compensation are correct.

However, discrepancies are found between Figure 5.5a and Figure 5.5b in the power spectra of local-compensated (green) and flexural-compensated (blue) topography. Their results especially mismatch at $n < 50$. Equation 3.35 suggests that the power spectrum of flexural-compensated topography is dependent on that of the local-compensated topography (Equation 3.34). If both of them go wrong, topography with local compensation should be checked first.

For $n = 2$, the power spectrum of the gravity effect of topography with local compensation ($D_c = 61$km) has a value of approximately 0.5 mGal^2 in Figure 5.4. That value is larger than 1 mGal^2 in Figure 5.5b ($D_c = 30$km). This does not make sense because a lower D_c should yield to a lower value in power spectrum according to Equation 3.34. The result in Figure 5.5a, which has a value slightly larger than 0.1 mGal^2, does make sense as it is lower than the value in Figure 5.4.

Furthermore, the best-fitting flexural rigidity $D = 4.37 \times 10^{23}$ N m (Watts and Moore, 2017) is not equivalent to the stated T_e=34 km when applying the values of parameters given by Watts and Moore (2017). It is likely that they used different values for parameters in the calculation instead of the ones they gave in the paper, which makes the reproduction of Figure 5.5b impossible[2].

[2]We have emailed Watts and Moore about this issue, but they have not responded yet. We also contacted Christian Hirt who confirmed that we used the correct Earth2014 RET model (Hirt et al., 2012).

5.3. The FEM Model

To study the behavior of the 3D flat Mars model, a series of simple loads are created as testing cases. These loads include single positive load, single negative load, dual positive loads, dual negative loads, positive & negative loads, and large dual positive loads. Only the most representative results are presented in this section.

5.3.1. Positive & Negative Loads

The Positive & Negative (PN) loads are the most representative simple loading case. The loads consist of a positive circular load up to +5 km and an negative circular load down to -5 km. The maximum or minimum points of the loads are at the center of the loads as shown in Figure 4.9.

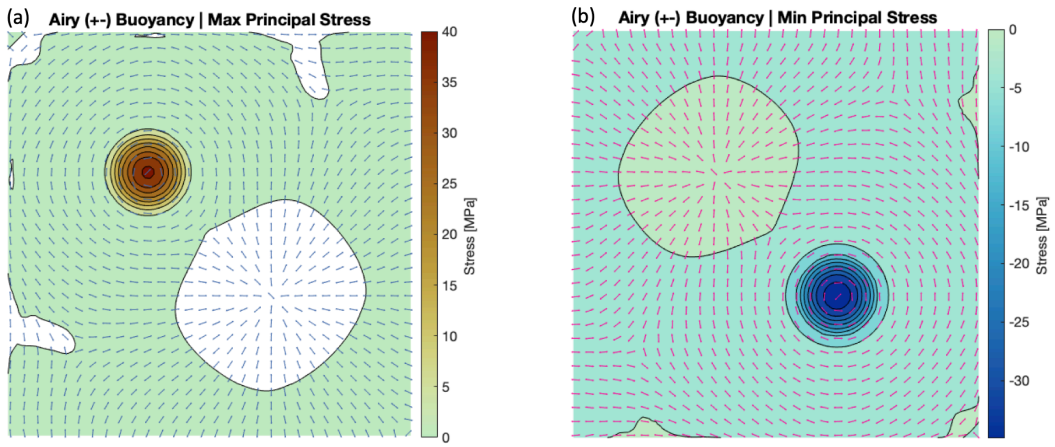

Figure 5.6: Maximum principal stresses (a) and Minimum principal stresses (b) at the surface for the NP loads with Airy's compensation. The arrows indicate the direction of maximum/minimum principal stresses.

Figure 5.6 shows the surface stress analysis for the PN loads under Airy's isostasy (other isostatic models have similar results). The positive maximum principal stresses, which indicate the tensional regions, are presented in Figure 5.6 (a). It shows that a large tensional zone is formed underneath the negative circular load at the upper left of the plots. While Figure 5.6 (b) shows the regions under compression with negative minimum principal stresses. And a compressional zone is caused by the positive load at the lower right of the plots. Judging from the directions of the principal stresses, both tensional and compressional faults are expected to be radially distributed over the loading areas.

While Figure 5.6 presents the surface stress state for only one model, Figure 5.7 compares principal stresses at the diagonal of the flat models with different compensations. The pink dashed curve represents the model without any extra compensation. While the blue and green ones stand for the models with Airy's and Pratt's compensations separately. The peak of the principal stresses can be found at the center of the negative load where is dominant by tensional stresses. And the bottom lies at the center of the positive load where the most compressional stresses prevail.

The models of local isostasy have compensations (buoyancy) at the crust-mantle boundary. Such buoyancy can support the loads together with the stresses in the crust. So, the models with isostatic compensations do not require as much stress as the non-compensation model to maintain the equilibrium. But the Airy's model under the negative load is an exception where the crust-mantle boundary moves closer to the surface and the modeled thickness of the lithosphere becomes very small.

It is important to note that the "non-compensation" (also called the "Abaqus") model is the model without extra buoyant support. For such a model, an equilibrium can still be reached because the shear stresses between the crustal elements/columns are not neglected in Abaqus. In other words, the stresses play a big role in supporting the loads.

Figure 5.8 compares the local isostasy (Pratt), flexural isostasy (Plate) and the non-isostasy models. Figure 4.10 already shows that the flexural model would experience less support from buoyancy than the local isostatic model because they have more support from stresses. As a result, the maximum principal stresses for the flexural (plate) model are higher than the Pratt's model in Figure 5.8.

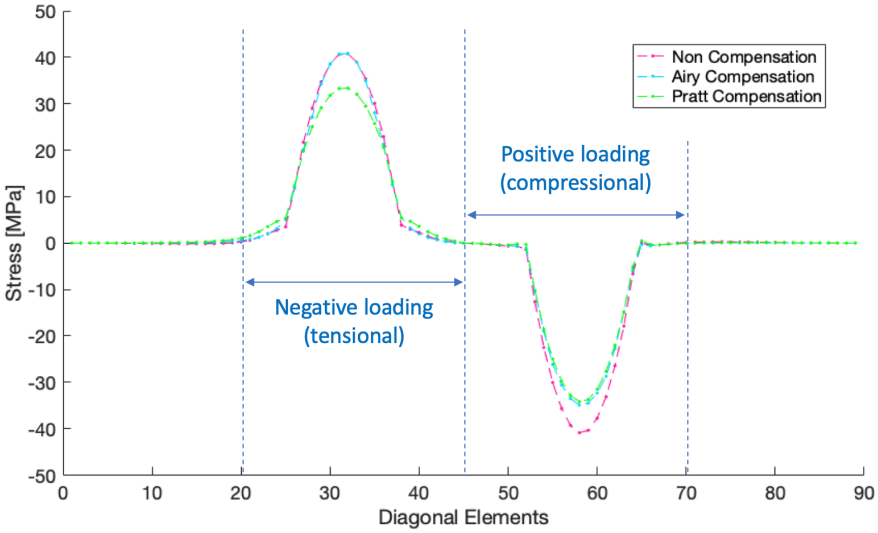

Figure 5.7: Maximum principal stresses of the diagonal elements for the NP loads with non (or Abaqus) (pink), Airy (blue) and Pratt (green) compensations.

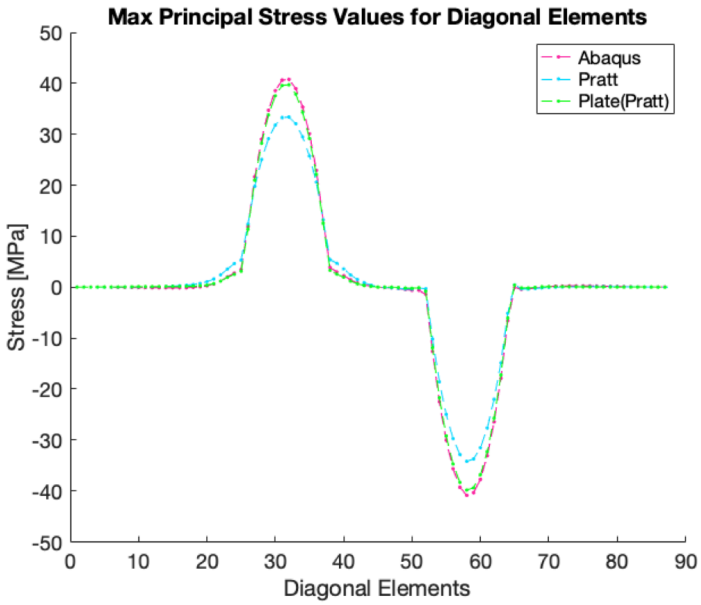

Figure 5.8: Maximum principal stresses of the diagonal elements for the NP loads with Abaqus (pink), Pratt (blue), and Plate (green) compensations.

Figure 5.9 and Figure 5.10 show the effects of varying the average crustal thickness (for the Airy's model) and the depth of compensation (for the Pratt's model), respectively.

For both models, increasing these parameters results in lower stresses in the crust under the peak of the loads. It suggests that a thicker crust in both Airy's and Pratt's models requires less stress support. The reason may be that stresses required to support the load can more widely spread in a thicker crust where the magnitude of stresses reduces. In other words, a crust with larger rigidity is simulated effectively. This further implies that pure local isostasy cannot be simulated in Abaqus as interaction between neighboring elements is not neglected.

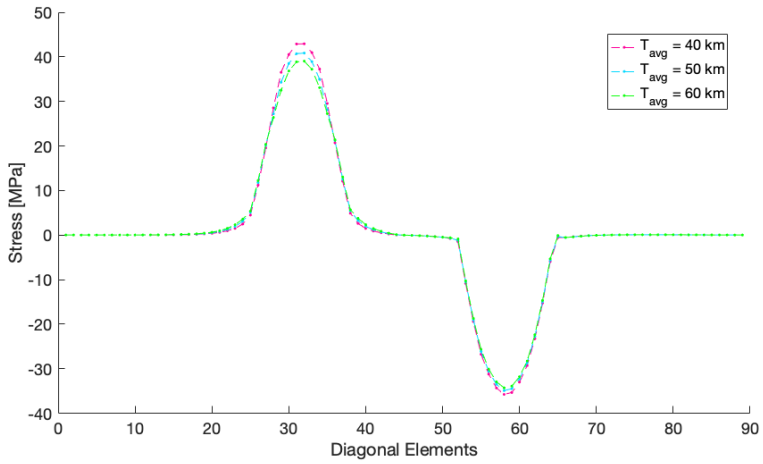

Figure 5.9: Maximum principal stresses of the diagonal elements for the NP loads with different average crustal thickness from Airy's model.

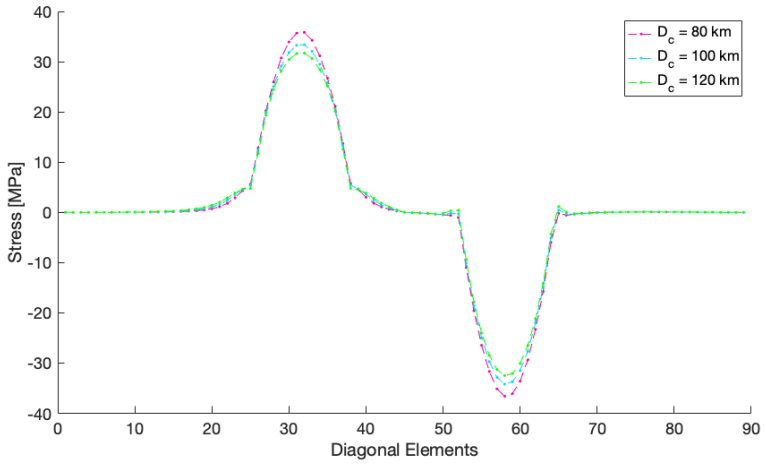

Figure 5.10: Maximum principal stresses of the diagonal elements for the NP loads with different depth of compensation from Pratt's model.

5.3.2. Large Dual-Positive Loads

The large-dual-positive (LDP) loads are designed to check if the infinite plate model and the thin shell model would behave differently in the flat Mars model. Figure 5.11 shows the difference in the flexural

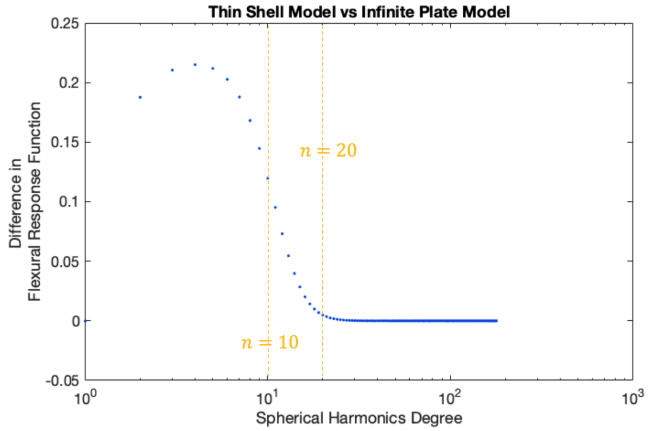

Figure 5.11: The difference in the flexural response functions between the infinite plate model and thin shell model (T_e=120 km).

response functions between the infinite plate model and thin shell model. Theoretically, their difference becomes visible from λ=1039 km (n=20) and increases to around 12% at λ=2030 km (n=10).

This means that for a load at the wavelength of around 2000 km, the buoyant support from the infinite plate model would be 10% higher than that from the thin shell model. To test if such a difference would affect the surface stresses, the LDP loads are created. The LDP-loading case includes two positive loads with radius of 354 km and 1000 km, respectively. The profiles of the loads can be found in Figure 5.12.

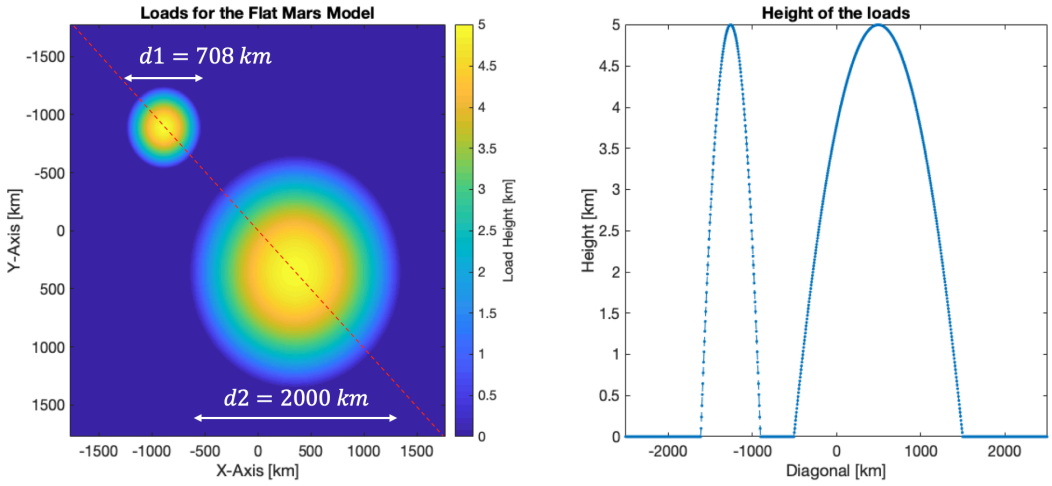

Figure 5.12: The large dual positive (LDP) loads with top view (left) and cross-section view (right).

The crustal thickness variations due to the LDP loads under the Airy's isostasy is visualized in Figure 5.13. The blue curve shows how the crustal thickness would vary under local isostasy (Airy). And these of the infinite plate model and the thin shell model are represented by the orange and yellow curves. It is clear that the flexural models relieve the crustal variation from the model of local isostasy, which is consistent with the study of David (2010) as shown in Figure 3.2. And less crustal variations are observed in the shell model than the plate model. What's more, as the wavelength of the load increases, the difference in the thickness variations between the two flexural models also increases.

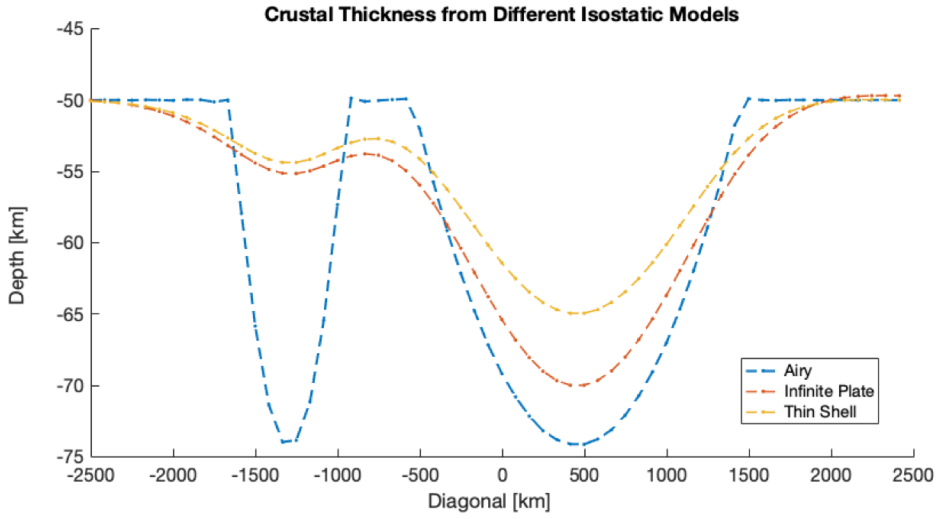

Figure 5.13: A cross-section view on the crust under the LDP loads with Airy, Infinite Plate and Thin Shell isostasy. A mean crustal thickness of 50 km is assumed for the Airy's isostasy. The crustal density is 2900 kg/m^3 and mantle density is 3500 kg/m^3.

The minimum principal stresses at the surface of the models with LDP loads are shown in Figure 5.14. The minimum principal stresses are presented because they show the how compressive the regions are under positive-topography loads. The red, blue and green curves show the stress profiles for non-compensated, airy-compensated and plate-compensated models. The bottom of the curves represents the centers of the loads where large differences between the local isostasy and the other two models can be found. Such differences are lower under the larger load, which can be explained by the difference in the crustal thickness as shown in Figure 5.13.

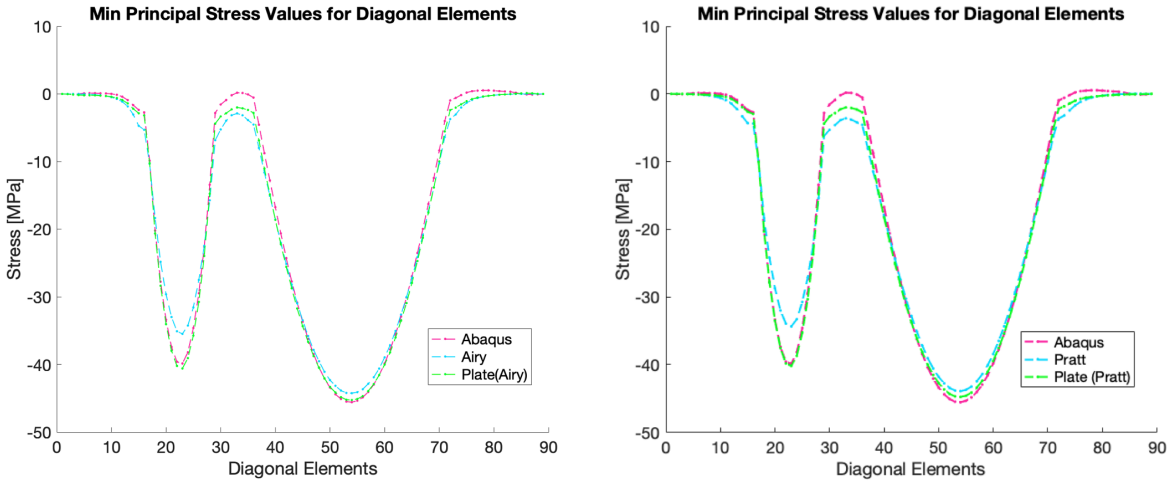

(a) Models based on **Airy** Isostasy (b) Models based on **Pratt** Isostasy

Figure 5.14: The minimum principal stresses at the diagonal under the LDP loads for different models. The stress states for elements at the diagonal are shown.

Though Figure 5.13 shows the differences in crustal thickness variations between the infinite plate model and the thin shell model, such differences do not significantly affect the stress state at the surface of the models. As Figure 5.15 suggests that the maximum difference in the minimum principal stresses at the center of the loads is around -0.2 MPa. On the other hand, the minimum principal stresses reach -45 MPa under the long-wavelength load (d2). Under the short-wavelength load (d1), the difference is even smaller. So, in the flat Mars model, the difference in the surface stresses between the infinite plate model and the thin shell model is negligible.

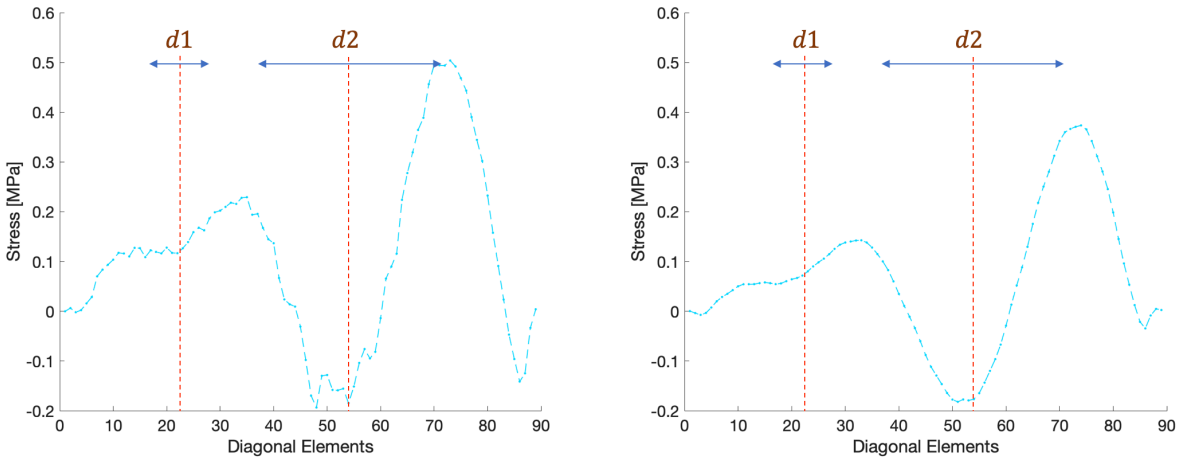

(a) Flexural Models based on **Airy** Isostasy (b) Flexural Models based on **Pratt** Isostasy

Figure 5.15: Differences of the minimum principal stresses between the infinite plate and thin shell models under the LDP loads. The red dashed lines indicate the centers of the loads (Figure 4.9).

6

Results

This chapter presents the major findings from this thesis. In section 6.1, the power spectra analysis is performed for all candidate crustal models, enabling the comparison of these models on Mars. The effects of independently varying parameters in the crustal models are also studied. After being evaluated, these crustal models are implemented in the FEM models. Therefore, section 6.2 presents the results from FEM modeling for the selected regions on Mars with previous defined crustal models. Besides purely isostatic support, a possible plume under the Tharsis rise is also investigated in the model.

6.1. Crustal Models for Mars

This section contains results from the crustal studies. Firstly, results from the power spectra analysis for different crustal models are presented. The best-fitting lithospheric thickness is obtained in different cases. Secondly, the effects of independently varying parameters (Young's modulus, Poisson's ratio and density contrast) are presented.

6.1.1. Power Spectra Analysis

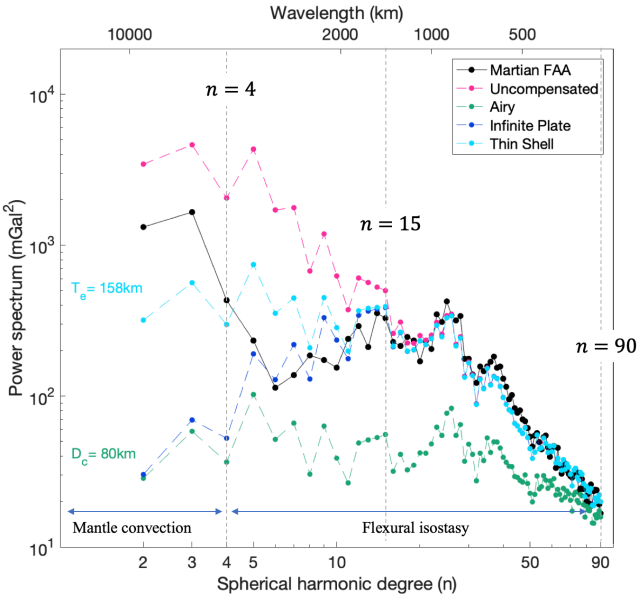

Figure 6.1: Comparison of the power spectrum of Martian FAA field (black) to calculated spectra based on the gravity effect of uncompensated topography (red) and the gravity effect of the topography and its local compensation (green), infinite plate compensation (dark blue) and thin shell compensation (light blue). The blue horizontal arrows show the estimated degree band where mantle dynamics and flexural isostasy make the most contribution. The lithospheric thickness T_e of 158 km is the best fit for the thin shell model from degree 2 to 90.

By comparing the power spectrum of the FAA and those of the gravity effect of the topography with different crustal models, one could evaluate the performance of these crustal models and find the more realistic models among them.

Figure 6.1 presents the power spectrum of the Martian FAA field (black) as a function of spherical harmonic degree, together with calculated spectra based on the gravity effect of topography with no compensation (red), local compensation (green), infinite plate compensation (dark blue) and thin shell compensation (light blue).

The uncompensated model (red) and fully compensated (green) model set the upper and lower limits for the calculated spectra, respectively. The power spectra of both flexural models, whose lithospheric thickness is 158 km, are in between the limits. Both flexural models converge to the uncompensated model at $n > 20$ region but they diverge from each other at low-degree region ($n < 15$). As the degree decreases, the power spectrum of the infinite plate model drops and tends to approach the fully compensated model while that of the thin shell model maintains at the same level.

The observed spectrum (black) has smaller values than the uncompensated topography (red) for $n < 25$. The reason why it is greater than the uncompensated model for $n \geqq 25$ regions is discussed in next chapter. From Figure 6.1, it is hard to determine whether the thin shell model or the infinite plate model is better fitting to the observation. Because the power spectrum from the infinite plate model better follows the power spectrum of the observation for $4 < n \leqq 15$. But in the low degree band ($2 \leqq n \leqq 4$), the power spectrum of the thin shell model is closer to that of the observation than the infinite plate model.

To compare the performance of both flexural models (thin shell and infinite plate), the Root-Mean-Square (RMS) errors between the power spectrum of observed gravity anomaly and that of the gravity effect of the topography with the thin shell and infinite plate compensation are calculated as a function of lithospheric thickness of the lithosphere (T_e).

Figure 6.2 shows these RMS errors for both the thin shell model (Figure 6.2a) and the infinite plate model (Figure 6.2b) from $2 \leqq n \leqq 90$. The best-fitting T_e for the thin shell model is 158 km with a RMS error of about 177.84 mGal^2. For the infinite plate model, a lower best-fitting T_e of 142 km is found with a higher RMS error (around 223.17 mGal^2).

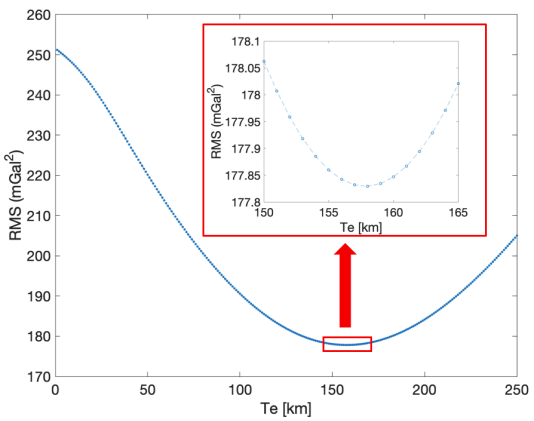

(a) RMS errors for the topography with the thin shell compensation. The best-fitting T_e of 158 km was found for $2 \leqq n \leqq 90$.

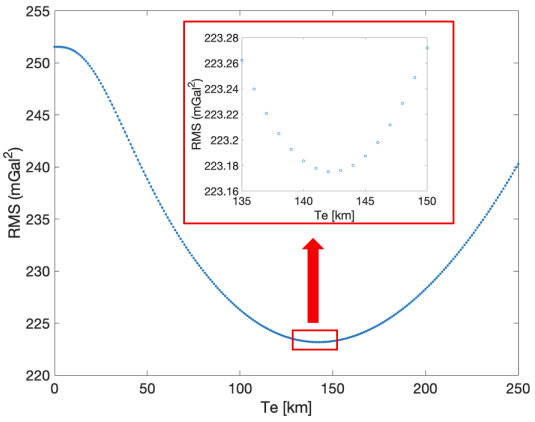

(b) RMS errors for the topography with the infinite plate compensation.The best-fitting T_e of 142 km was found for $2 \leqq n \leqq 90$.

Figure 6.2: RMS errors between Martian FAA and the gravity effect of the topography with flexural compensation as a function of lithospheric thickness T_e. Insets show the zoom-in view of the red rectangular zone where the best-fitting value of T_e was found. RMS errors are calculated globally from $2 \leqq n \leqq 90$. Values for parameters are summarized in Table 3.2.

Figure 6.3 shows these RMS errors for both the thin shell model (Figure 6.3a) and the infinite plate model (Figure 6.3b) from $5 \leqq n \leqq 90$. For both models, the elastic thickness of the lithosphere is thinner than the previous case. The best-fitting T_e is found to be 101 km and 136 km for the thin shell model and infinite plate model, respectively. Unlike Figure 6.2, the RMS error for the infinite plate model is smaller than that of the thin shell model in Figure 6.3.

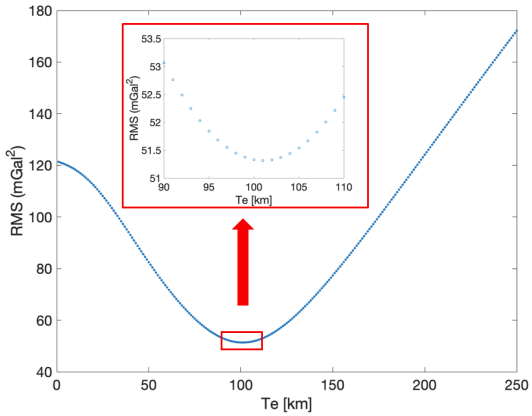

(a) RMS errors for the topography with the thin shell compensation. The best-fitting T_e of 101 km was found for $5 \leqq n \leqq 90$.

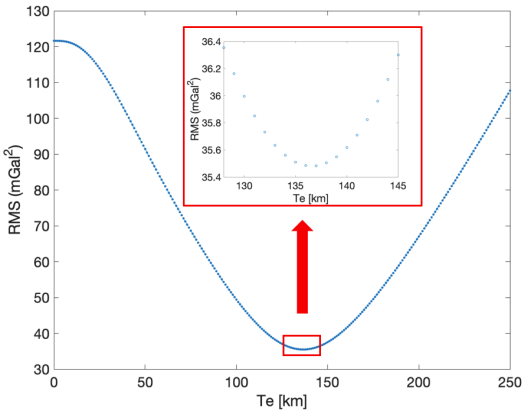

(b) RMS errors for the topography with the infinite plate compensation.The best-fitting T_e of 136 km was found for $5 \leqq n \leqq 90$.

Figure 6.3: RMS errors between Martian FAA and the gravity effect of the topography with flexural compensation as a function of lithospheric thickness T_e. Insets show the zoom-in view of the red rectangular zone where the best-fitting value of T_e was found. RMS errors are calculated from $5 \leqq n \leqq 90$ (without first four degrees where mantle dynamics play a role).

6.1.2. Effects of Independently Varying Parameters

As summarized in Table 3.1, the flexural response functions of the infinite plate and the thin shell models are dependent on various parameters, such as Young's modulus, Poisson's ratio, and the density contrast between the crust and mantle. The following results show how these parameters affect the best-fitting lithospheric thickness in the power spectra analysis. To find the best-fitting T_e, the gravity effect of the topography with the thin shell compensation is compared to the observed gravity anomaly of Mars. The RMS errors are calculated from degree 2 to 90.

Figure 6.4 shows the effects of varying Young's modulus on the best-fitting lithospheric thickness. Young's modulus ranges from 1 to 100 GPa, and the corresponding best-fitting T_e drops from 580 km to around 120 km. In Figure 6.2a, the best-fitting T_e of 158 km is found with a Young's modulus of 65 GPa, which is consistent in Figure 6.4.

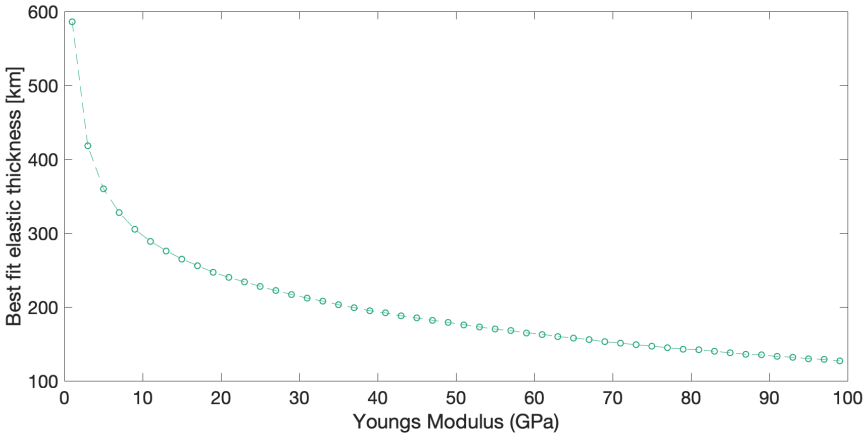

Figure 6.4: The best-fitting lithospheric thickness T_e as a function of Young's modulus for the thin shell model ($2 \leqq n \leqq 90$). Young's modulus ranges from 1 GPa to 100 GPa. Values for other parameters are summarized in Table 3.2.

The effects of varying the Poisson's ratio on the best-fitting lithospheric thickness are shown in Figure 6.5 where the best-fitting T_e decreases gradually with an increasing Poisson's ratio. The variation of the best-fitting T_e is about 12 km for the given range of Poisson's ratio.

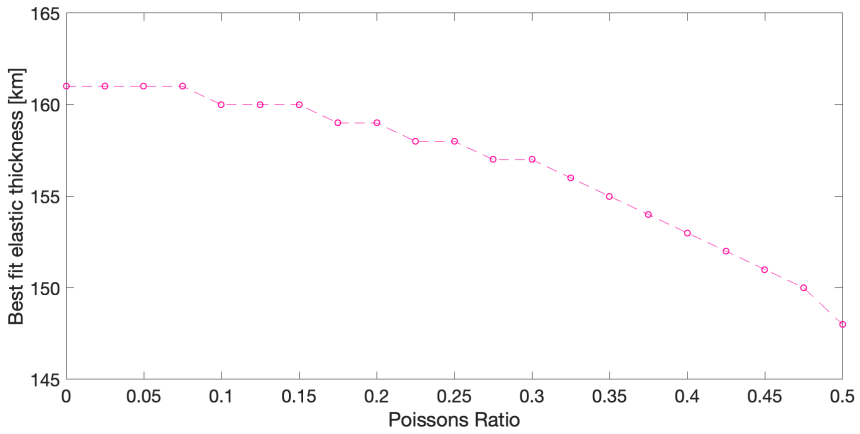

Figure 6.5: The best-fitting lithospheric thickness T_e as a function of Poisson's ratio for the thin shell model ($2 \leqq n \leqq 90$). The value of Poisson's ratio ranges from 0 to 0.5.

The range of the density contrast between the crust and mantle of Mars is from 400 to 900 kg/m^3 (Knapmeyer-Endrun et al., 2021). As the density contrast increases from 400 to 900 km, the best-fitting T_e also increases. The variation of T_e due to changes of density contrast in Figure 6.6 is around 60 km.

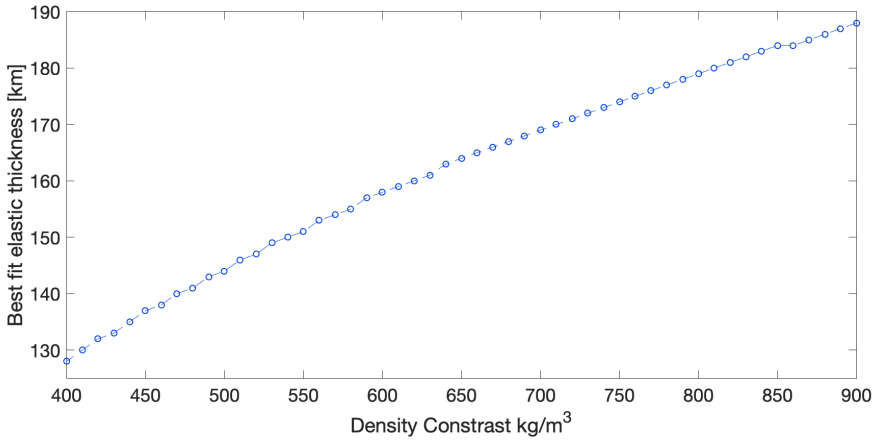

Figure 6.6: The best-fitting lithospheric thickness T_e as a function of density contrast between the crust and mantle for the thin shell model ($2 \leqq n \leqq 90$). The mantle density is assumed to be 3500 kg/m^3, and the density contrast ranges from 400 to 900 kg/m^3.

6.2. Faults Characterization

In this section, the results from the FEM models are presented for different regions of interest. Firstly, the results for the Tharsis Rise and Hellas Basin are shown because they represent regions with large positive-topography and negative-topography features, respectively. Then, the Utopia region, where both positive and negative features appear, is presented.

The principal stresses or strains together with the surface faults are plotted for the target regions. Tensional faults are likely to occur at the regions with positive maximum principal stresses. Regions with negative minimum principal stresses are in compression, where compressional faults could grow. The flat models with no compensation, Airy's compensation, Pratt's compensation, infinite plate's compensation and thin shell's compensation are all simulated. Since they yield similar results in most of the cases, only the most representative results are shown in this section. Extra figures for other models can be found in Appendix B.

6.2.1. Tharsis

Figure 6.7 shows the maximum principal stresses together with tensional faults (a) and the minimum principal stresses along with compressional faults (b). The small red arrows in the plots indicate the directions of the principal stresses. Important topographic features are marked in both plots, and the center of the region is at 0° N, 120° W. The topography of the target region is shown in Figure 4.14a, and the resulted surface stresses are quite correlated to the topography. Large compressional zones can be found under the giant Tharsis mountains (Olympus Mons and Tharsis Montes). The areas with negative topography are dominated by tensional stresses. However, only large topographic features are still recognizable in the stress field.

In Figure 6.7 (a), the tensional faults distribute radially with respect to the Tharsis Montes, Alba Mons, and Tempe Terra. But the regions, which are dominated by the tensional faults, are under large compression according to the stress analysis. Furthermore, the directions of the minimum principal stresses cannot explain the observed tensional faults. There might be some divergence between the model assumptions and the actual regional conditions in Tharsis.

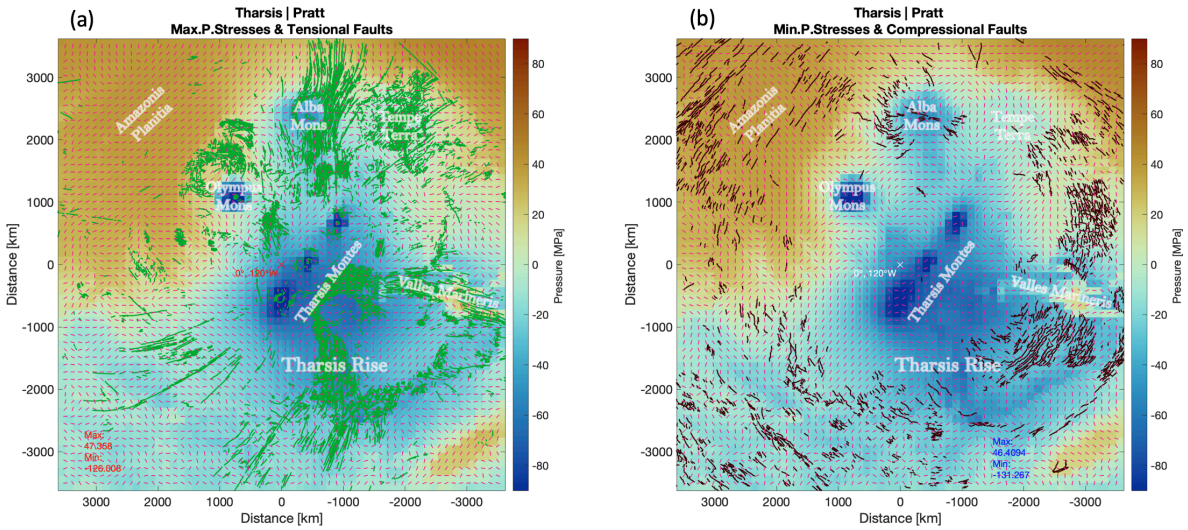

Figure 6.7: Maximum principal stresses (a) and minimum principal stresses (b) for the Tharsis Rise region with Pratt's Isostasy. Tensional (green) and compressional (brown) faults are also plotted.

The principal strain plots for the Tharsis region can be found in Figure 6.8. Since strain is related to the displacement, more detailed topographic feature can be observed in the strain plots. In Figure 6.8 (a) where the maximum principal strains and the tensional faults are shown, the locations of the large strains are quite consistent with the observed tensional faults. The radial tensional faults at the south of the Tharsis Rise, along the Valles Marineris, around the Alba Mons, and over the Tempe Terra all overlap with the deep brown color which indicates positive (tensional) large strains. The compressional strains are found where large topographic difference appears, like the surrounds of large Tharsis mountains and the Valles Marineris. Some circumferential patterns are found for the compressional strains

but they are not related to the observed compressional faults.

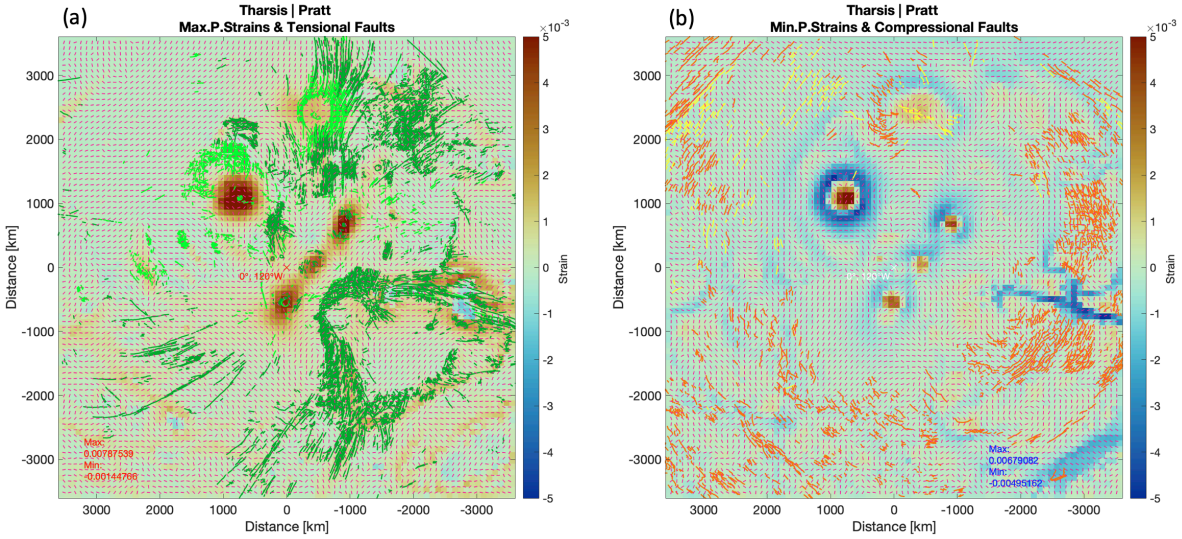

Figure 6.8: Maximum principal strains (a) and minimum principal strains (b) for the Tharsis Rise region with Pratt's Isostasy. Tensional (green) and compressional (orange) faults are also plotted. The faults younger than 3.5 Gyr are highlighted with light green and yellow in both plots.

Bottom Loading

Bottom loads with different orders of magnitude (10 MPa, 100 MPa, 1000 MPa, 10000 MPa) are applied at the crust-mantle boundary of the flat Mars model. The results for all positive (upwards) and negative (downwards) bottom loading cases are shown in Figure B.16 and Figure B.17, respectively. Both figures suggest that the effects of bottom loading would be visible with a bottom load at around 1000 MPa. A larger bottom load at the magnitude of 10000 MPa would cause too much compression or tension to the Tharsis region and serve boundary effects in the flat model.

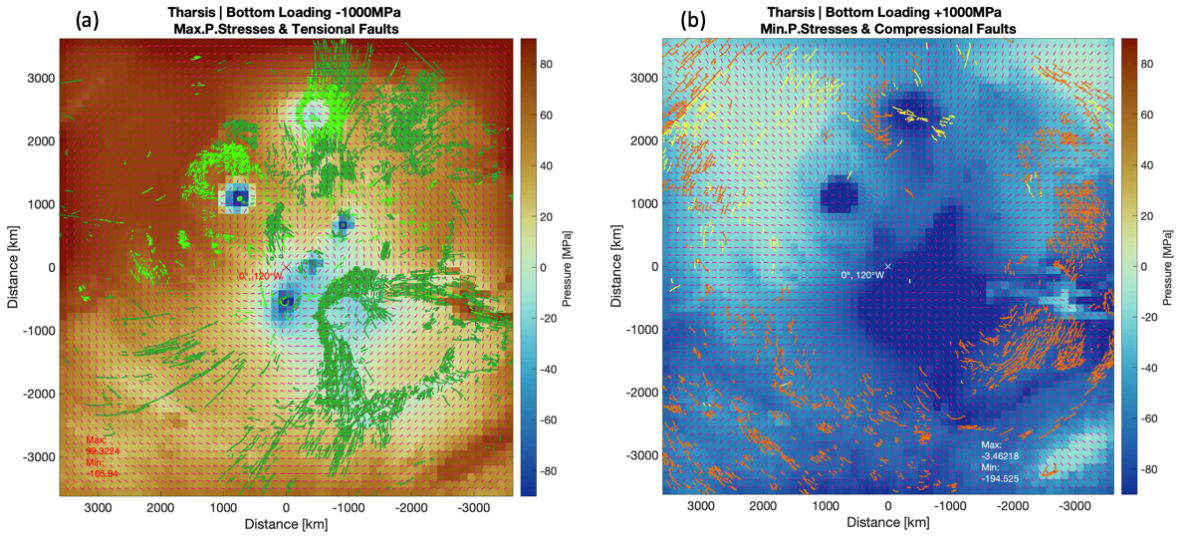

Figure 6.9: The principal stresses and observed faults for the Tharsis Rise region with negative (a:-1000 MPa) and positive (b: +1000 MPa) bottom loads.

Figure 6.9 shows the the region under negative (-1000 MPa) and positive (+1000 MPa) bottom loads, respectively. With negative bottom loading, tensional stresses dominate almost the whole region except for the mountains. Compressional stresses prevail the whole plot when the positive bottom

loading is applied. Compared to Figure 6.7, the directions of the principal stresses are different in Figure 6.9. The directions of the stresses under the bottom loading are nearly circumferential for the tensional stresses and radial for the compressional stresses, which could explain the radial tensional faults and circular compressional faults.

6.2.2. Hellas

The strain analysis for the Hellas Basin can be found in Figure 6.10 where detailed features are shown. It shows both maximum principal strains (a) and minimum principal strains (b) for the Hellas Basin region. The maximum principal strain plot Figure 6.10(a) suggests that there are nearly circumferential tensional structures around the impact basin. The inner tensional structure almost encloses the impact crater and only leaves an opening at the northeast corner where several linear tensional faults lie. The outer tensional structure depicts the boundary of the Hellas Basin and is more tensional than the inner one. The tensional faults in the northern boundary of Hellas Basin lie in the tensional-strain zone. The minimum principal strain plot Figure 6.10(b) nicely depicts the boundary of the deep impact basin and its surrounds. The large compressional strains around the impact crater are consistent with the circular comrpessional faults around the crater's boundary.

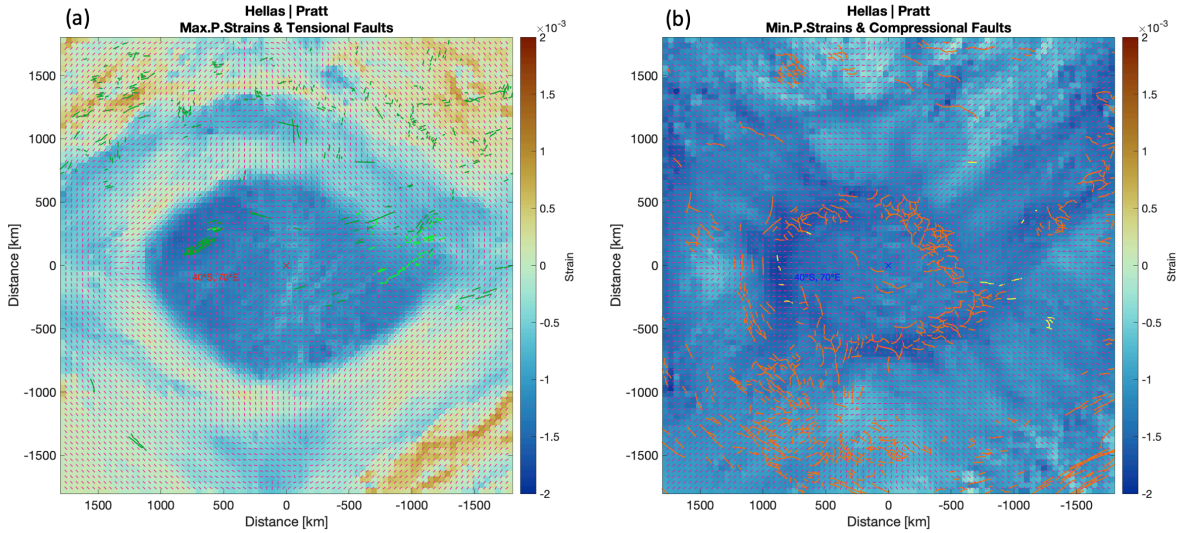

Figure 6.10: Maximum principal strains (a) and minimum principal strains (b) for the Hellas Basin region with Pratt's Isostasy. Tensional (green) and compressional (orange) faults are also plotted. The faults younger than 3.5 Gyr are highlighted with light green and yellow in both plots.

Figure 6.11 shows the maximum principal stresses (a) and minimum principal stresses (b) for the Hellas Basin region. The corresponding faults are also mapped on the plots. It is shown that the region is dominated by tensional stresses. This is what would happen when negative topography is loaded on the surface of the flat model. Though the stress analysis explains the existence of the compressional faults at the lower bottom of the model, the majority of the observed faults are not consistent with the calculated stress field.

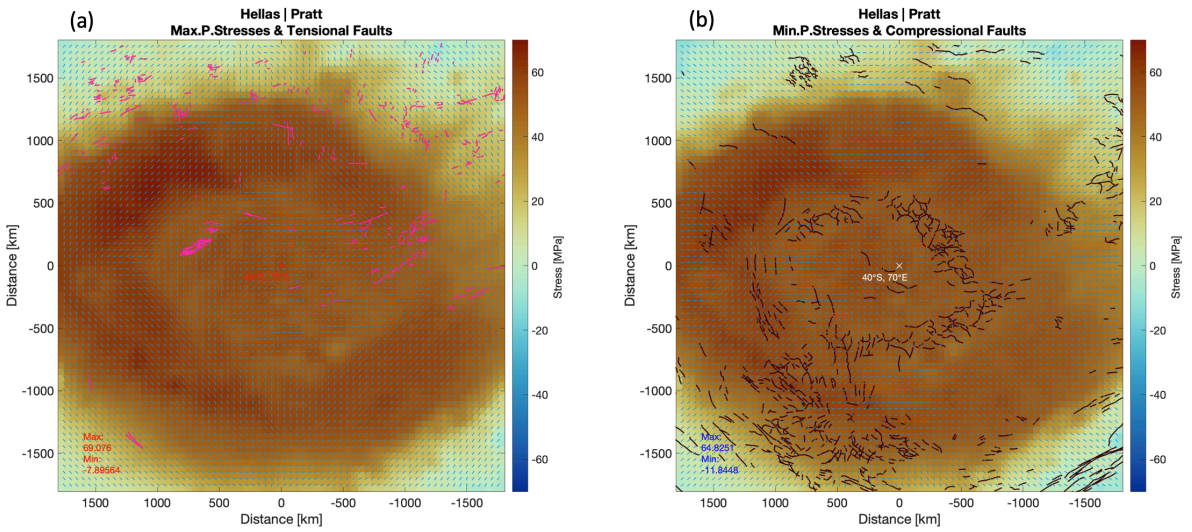

Figure 6.11: Maximum principal stresses (a) and minimum principal stresses (b) for the Hellas Basin region with Pratt's Isostasy. Tensional (green) and compressional (brown) faults are also plotted.The arrows indicate the direction of the principal stresses

6.2.3. Utopia

The strain analysis and stress analysis for the Utopia region are shown in Figure 6.12 and Figure 6.13, respectively. Utopia Basin, Isidis Basin, a part of Hellas Basin, Elysium Mons, and the dichotomy boundary can be observed in this region.

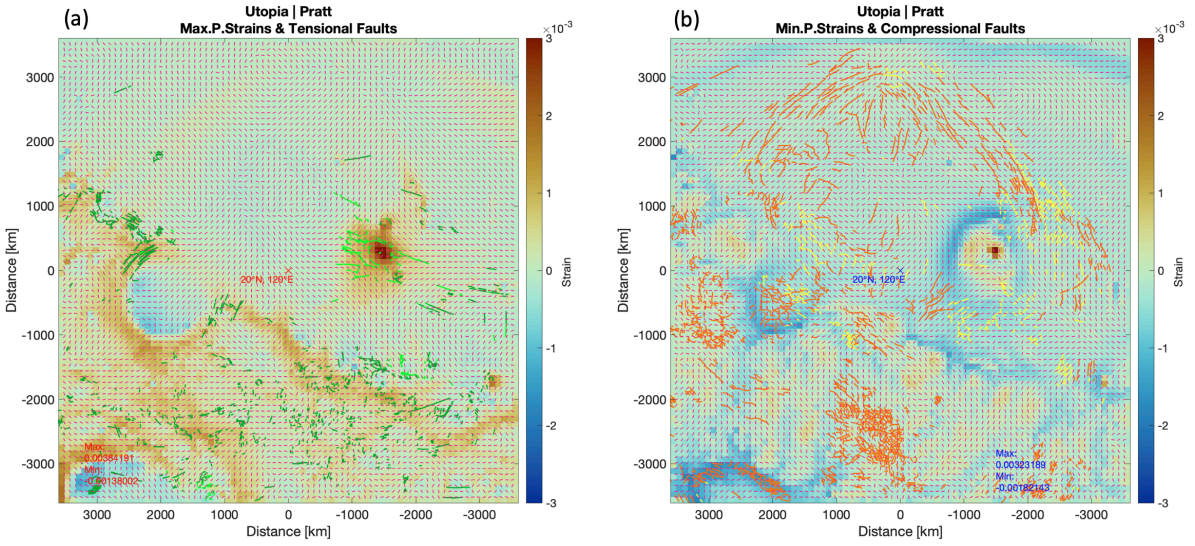

Figure 6.12: Maximum principal strains (a) and minimum principal strains (b) for the Utopia Basin region with Pratt's Isostasy. Tensional (green) and compressional (orange) faults are also plotted. The faults younger than 3.5 Gyr are highlighted with light green and yellow in both plots. Tensional strains are positive while compressional strains are negative.

Figure 6.12(a) presents the tensional strains and faults. Both the dichotomy boundary and Elysium Mons are highlighted by the tensional strains. Large tensional strains also cover the northern rims of the Hellas Basin and near continuously distributed all the way to the periphery of Isidis Basin. The Utopia Basin, which covers a large part in this region, is hardly visible in the plot. And the tensional strains which depict the boundary of the Utopia Basin have relatively low values. The distribution of the tensional strains is in harmony with the computed tensional strain field.

Compressional strains are found on the edges of the Elysium Mons, Isidis Basin, Hellas Basin, and parts of the dichotomy boundary as shown in Figure 6.12(b). But these compressive regions do not coincide with the observed compressional faults except for the Hellas. The compressive strains enclose

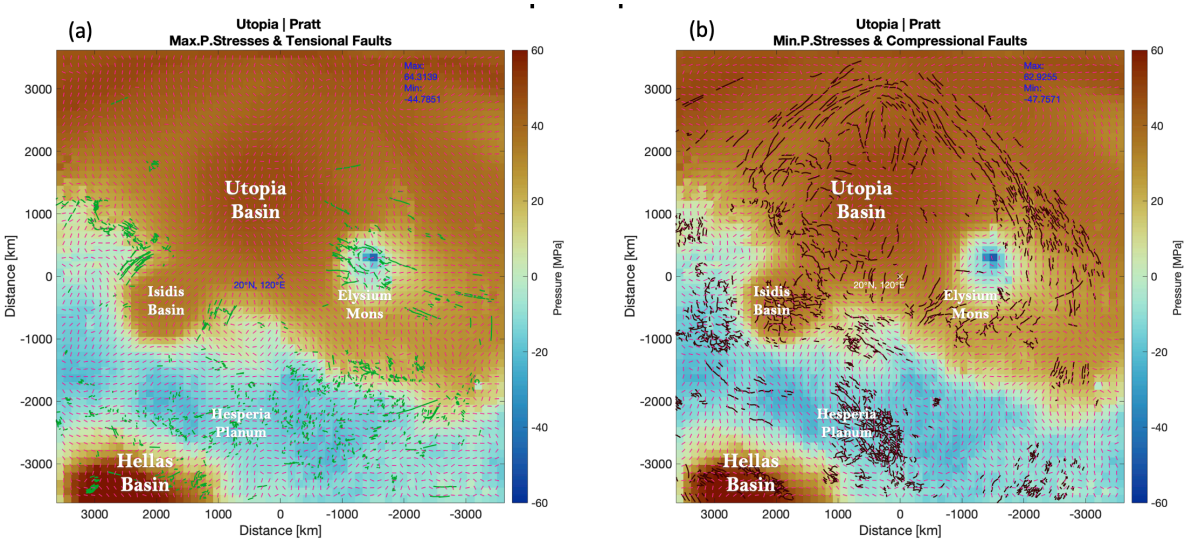

Figure 6.13: Maximum principal stresses (a) and minimum principal stresses (b) for the Hellas Basin region with Pratt's Isostasy. Tensional (green) and compressional (brown) faults are also plotted.The arrows indicate the direction of the principal stresses. Tensional stresses are positive while compressional stresses are negative.

the Utopia Basin, as well as the Elysium Mons, but no clear relationship between these compressive faults and strains are found.

Figure 6.13 shows the results from the principal stress analysis. The positive maximum principal stresses present that all basins and the regions in the north of the dichotomy are under large tensional stresses. One exception is the Elysium Mons, which causes a local compressional region by the southeast of the Utopia Basin.

The compressional faults around the Hesperia Planum and to the west of Isidis Basin lie in the compression-dominant zone. But there are a large number of compressional faults, which are likely related to the topography, can either be explained by the strains or the stresses in the north of the Martian dichotomy.

7 Discussion

In this chapter, the results obtained in this research are interpreted. Both implications and limitations of this study are discussed. Furthermore, results from other similar studies are compared. Investigations on the crustal structure and faults characterization on the regions of interest are presented in section 7.1 and section 7.2, respectively. The discussion on the results of the FEM model from section 5.3 can be found in section 7.3.

7.1. Crustal Models for Mars

This chapter discusses the results obtained for the crustal study of Mars. The outcomes from different models of isostasy are interpreted. The comparison of power spectra analysis between Mars and the Earth is included. The effect of varying Young's modulus is highlighted and compared to similar studies. In the end, the limitation of the approach used in the crustal study is discussed.

7.1.1. Power Spectra Analysis

As shown in Figure 6.1, the power spectra of the gravity effect of topography with compensation from the infinite plate and the thin shell models agree better with that of the observed FAA than the model of local isostasy. This suggests that the flexural models are decent representations of the lithosphere of Mars, and the flexural isostasy is widely operative on this red planet.

Comparisons between both flexural models in Figure 6.2 and Figure 6.3 show that the gravity effect of topography from the thin shell model better fits the observed gravity anomaly than that of the infinite plate model on a global scale ($2 \leqq n \leqq 90$). This can be visually confirmed in Figure 6.1 where the spectrum of the thin shell model is closer to the observed spectrum for $n \leqq 4$.

But when the low-degree terms ($n = 2, 3, 4$) which contain the effects of mantle dynamics are removed, the infinite plate model outperforms the thin shell model for $5 \leqq n \leqq 90$. This can be observed in Figure 6.1 where the spectrum of the infinite plate model better follows that of the observation from $n = 5$ to 15 than the thin shell model.

The different behaviors between both flexural models can be attributed to the fact that the thin shell model takes the curvature of the planet into account and introduces the membrane stresses. For lower degrees (longer wavelengths), the support from the membrane stress plays a role, and the thin shell model overestimates the gravity effect of topography than the infinite plate model. Such a difference is also illustrated in the plots of flexure response functions (Figure 3.6).

The power spectra analysis for the Earth (Figure 3.9) is different from that for Mars: while the flexural isostasy dominates the HDB ($33 < n < 400$) as well, the model of local isostasy still plays a important role between the HDB and LDB ($12 < n < 33$). The fact that the model of local isostasy does not fit with observation does not suggest that local isostasy is absent on Mars. Since the models are simplified and represent the planet as a whole, there could be some regions under local isostasy on Mars.

Comparison between the magnitude of observed spectra in both Figure 3.9 and Figure 6.1 shows that the FAA of Mars is about one or two orders of magnitude higher than that of the Earth. This may be a results of both lack of plate tectonics and active mantle convection on Mars. It also suggests Mars has a very strong lithosphere which can support all those mass anomalies on it. For both Mars and the

Earth, the observed spectra at low-degree region are not properly modeled by the models of isostasy. Because the major source of support for topographic features changes from elastic isostasy at short wavelengths to dynamics mantle at long wavelengths.

7.1.2. Varying Parameters

The best-fitting T_e is sensitive to parameters, such as Young's modulus, Poisson's ratio, and the density contrast between the crust and mantle. Results in previous chapter show that Young's modulus has the most prominent effect on the best-fitting lithospheric thickness among the above-mentioned parameters.

Young's modulus measures the stiffness of a material. Materials with a high Young's modulus are not easily deformed when forces are applying on them. Figure 6.4 shows that a higher Young's modulus yields to a lower T_e. Such a negative correlation between Young's modulus and T_e is also found by Taylor et al. (2020). It could be interpreted as that a thick lithosphere is not required when the stiffness of the crustal material is high. On the contrary, when the crustal material has lower stiffness, a thin lithosphere would not be strong enough to support the crust. In other words, the increase of lithopheric thickness compensates the effect of decreasing Young' Modulus (lower material stiffness).

Recent seismic study (Khan et al., 2021) suggests that Mars has a very thick lithosphere with a depth of around 500 km, which is much higher than the best-fitting T_e found in both Figure 6.2 (158 km) and Figure 6.3 (136 km). On the one hand, Khan et al. (2021) only used eight seismic events detected by InSight mission, and their results could contain large uncertainties. On the other hand, Figure 6.4 indicates that it is possible to obtain such a deep lithosphere in the model by lowering Young's modulus. For a T_e of 500 km, Young's modulus of around 2 GPa is found in Figure 6.4. This value is much lower than the values used in previous studies (Belleguic et al., 2005, McGovern et al., 2002, Neumann et al., 2004) where Young's modulus is around 100 GPa. But relatively lower values for Young's modulus on Mars are obtained by Heap et al. (2020) (5.4 GPa) and Taylor et al. (2020) (17.8 GPa). In addition, a lower Young's modulus (2 GPa) will result in a thicker lithosphere (500 km), which is consistent with the recent seismic study by Khan et al. (2021). It could be that the values of lithospheric Young's modulus on Mars have been overestimated.

7.1.3. Limitation

As shown in Figure 6.2, the RMS errors are higher than the results for the Earth from Watts and Moore (2017). This suggest that there are still rooms to improve the crustal models in this study. For example, the observed spectrum is higher than the calculated ones for $n > 25$ in Figure 6.1. It could be that the crustal density used does not have the optimal value. Instead of using an uniform value for the crustal density, one could derive the degree-dependent crustal density.

Figure 4.11b presents the profile of global crustal thickness with a thin shell model ($T_e = 158$ km). On the one hand, the results from Figure 4.11b agree with recent seismic findings (Knapmeyer-Endrun et al., 2021) that the mean crustal thickness of Mars ranges between 24 km and 72 km. On the other hand, comparison between Figure 4.11a and Figure 4.11b shows that detailed (short-wavelength) features are erased in Figure 4.11b.

7.2. Faults Characterization

In this section, results from the 3D flat FEM model are interpreted by regions. Similar studies are compared for three regions of interest. Implications from the results on the subsurface structure are elaborated.

7.2.1. Tharsis

The Tharsis Rise is the second largest feature on the surface of Mars, which covers around one quarter of the planet's surface. The most significant long-wavelength areoid and topographic anomalies are observed in the Tharsis region. Two competing models were proposed to explain the formation of the giant rise (Zhong, 2002): one depends on the dynamic support from an upwelling mantle plume (bottom loading), and the other rely on volcanic construction and its associated lithosphere flexure (top loading). These two models are not contradicting to each other, and the combination of both models

could provide a better explanation to the origin of the Tharsis rise (Redmond and King, 2004). By loading the topography on the surface of the model and searching for the state of equilibrium with geostatic step in Abaqus, this study takes the idea of top loading to obtain a lithosphere that supports the Tharsis Rise.

Figure 6.7 shows that the calculated surface principal stresses and observed faults do not quite match in terms of both location and direction. This inconsistency may come from the assumption that the 3D FEM model only calculates the state of equilibrium while such an equilibrium state has not been reached in the Tharsis region. This implies that the Tharsis region might still be active.

The values of the principal strains obtained for the Tharsis region are at the same order of magnitude of that found by Golombek and Phillips (2010). While the observed tensional faults quite match the calculated strain map, the computed minimum principal strains do not yield much information about the compressional faults. This suggests the tensional faults might be geologically younger than the compressional faults in the Tharsis region as they can be explained by the strain analysis with recent topography data. This is further supported by the minimum principal strains plot (Figure 6.8) which shows that circumferential compressional strains are found around large mountains. In the early stage of the Tharsis Rise when the whole region was rising, such circumferential compressional strains could dominate the region and the related compressional faults may form at that time. But with only a volcanically constructed lithosphere, it is insufficient to explain the distribution of both tensional and compressional faults in the Tharsis region.

By including the bottom loading in the model, the effects of both volcanic construction and the mantle plume are taken into account and more insights about the formation of the region can be obtained. The observed faults fit quite well with both the positive bottom load (upwelling) and the negative bottom load (downwelling) in terms of direction and location (Figure 6.9). This suggests that the dynamic support played an important role in the formation of the Tharsis Rise in the perspective of stresses and faults formation.

Putting the pieces together, a theory to explain the formation of the Tharsis Rise is formulated. In the early stage, the upwelling mantle plume (positive bottom loading) brings the uplift on the Tharsis region. Such a positive bottom load would also bring large compressional stresses on the surface, which would induce circumferential compressional faults around the giant bulge. The lithosphere and the upwelling mantle plume support the Tharsis together. But as time goes, the mantle plume would lose heat and cool down. In the later stage, an downwelling mantle plume may replace the upwelling plume. This cooler plume may have a lower wavelength than the initial hotter one. But it would significantly change the stress condition from compressional to extensional around the Tharsis Montes, Alba Mons, and Mons Olympus. As a result, radial-distributed extensional faults replace the compressional faults at the center of the Tharsis region. However, there are some old circumferential compressional faults that remain at the rim of the Tharsis bulge, which explains why extensional faults dominate the inner of Tharsis Rise.

7.2.2. Hellas

The Hellas Basin is a huge impact crater which is estimated to have formed 4 billion years ago[1]. As shown in Figure 4.14c, the impact crater itself has a diameter of 2300 km and a depth of over 7 km. It would only occupy about 40% of the surface of the flat model. But over 80% of the flat model is under tensional stresses when the equilibrium is reached. This shows how large one impact crater can affect its surrounding areas.

The strain analysis is consistent with the distribution of both tensional and compressional faults. This suggests that the calculated equilibrium state for the Hellas Basin fits well with its current state. So, for Hellas, local isostasy plays an important role in its formation and evolution. This is line with the finding from Neumann et al. (2004) that the Moho relief under the Hellas Basin is close to be in the state of isostatic equilibrium.

The reasons why the stress analysis for Hellas does not work well with the faults could be: firstly, the modeled state does not match the actual situation for the target region; secondly, the model itself could not handle the negative topography well. Thirdly, stress may not be a good parameter to analyze the faults. The first reason is dismissed as the strain analysis yields decent results about the faults.

To elaborate the second point, one should recall the model settings which is introduced in chapter 4.

[1] https://sci.esa.int/web/mars-express/-/55575-craters-within-the-hellas-basin [15-07-2021]

The flat Mars FEM model uses the geostatic step which ensures a state of equilibrium between the surface loads and lithosphere stress is reached. In this case, the way how the geostatic works does not bring the issue but the way to load the topography might do. The surface topography is loaded as pressure on the surface of the flat Mars model. Positive topography, like a mountain, is converted into positive pressure which points downwards. In this way, the compression brought by the extra masses is simulated in the model. But when this approach is applied to the negative topography, it would convert the negative topography into negative (upward) pressure to simulate the tension coming from the mass dispossession. As a results, the surface tensional stresses are overestimated in the flat Mars model for regions with negative topography. Blank (2015) also confronted the issue of negative topography in the FEM model, and he set the load height to zero at the negative-topography region to avoid the issue.

The third point is raised because the large tensional stresses are also found under the Hellas Basin by Batov et al. (2019) as shown in Figure 7.1. Even higher tensional stresses are expected at the surface as shown in Figure 7.2, which is consistent with the results in this study. This suggests that the inconsistency between the stress states and faults distribution is not due to the errors in stress calculation. The real problem could be the fact that faults are linked to the displacements while the stresses are not. This also explains why the elastic strain is a more direct parameter to compare with the faults than the stress because the strain reflects displacement (Banerdt and Golombek, 2000).

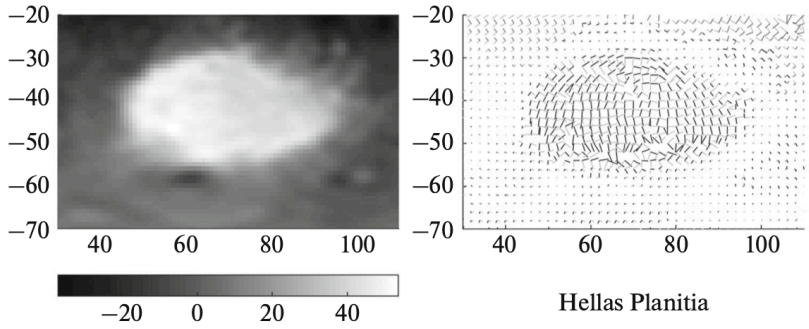

Figure 7.1: Tensile(positive)-compressive(negative) stresses and axes projections of stress tensor for Hellas Basin (Batov et al., 2019). The stress state at the depth of 10km is shown. Lengths of principal stress axes projections are proportional to stress magnitudes.

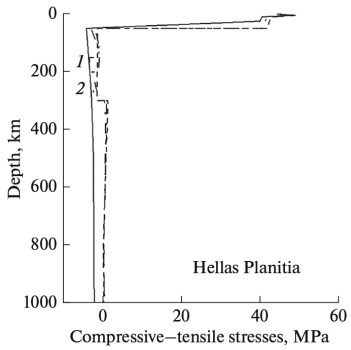

Figure 7.2: Distribution of compressive-tensile stresses along depth beneath the Hellas (Batov et al., 2019). Compressive stresses are with negative values while tensile stresses are positive.)

7.2.3. Utopia

The Utopia region selected in this study contains a variety of topographic features like the boundary of the global dichotomy, Utopia Basin, Isidis Basin, Elysium Mons, Hesperia Planum, and a part of Hellas Basin. Hellas Basin has been discussed previously and is thought to be in isostatic equilibrium. This is confirmed by the compressional strains plot in Figure 6.12 (b) where the compressional faults coincide with calculated compressive strains.

The situations are different for the other basins. The edges of the Isidis Basin are depicted by compressive strains. However, the compressional faults around the Isidis Basin do not follow the edges but go through the basin. Although the Utopia Basin is surrounded by large circumferential compressional faults, no evidence from the perspective of either strain or stress is found to support the formation of those faults. Compared to the Hellas Basin, different relationship between the observed faults and calculated strains/stresses shows that the basins of the Isidis and Utopia are not in the state of isostatic equilibrium. Figure 7.3 presents the surface height and calculated Moho depth for several large topographic features on Mars by Neumann et al. (2004). It shows that the crustal profile of the Hellas Basin closely follows the result of local isostasy but those of the Isidis and Utopia basins are higher than the dashed curve. This means that the Isidis Basin and Utopia Basin are currently over compensated by the lithosphere. Since the flat Mars model only simulates the region with local compensation, it is not surprising that the calculated results for the Utopia and Isidis do not match to the observations.

To model the super-isostatic uplift under Utopia and Isidis, one could apply positive bottom loading as tested for the Tharsis Rise. It is expected that the bottom loading would generate compressive stress fields under the basins, which could support the formation of the observed compressional faults.

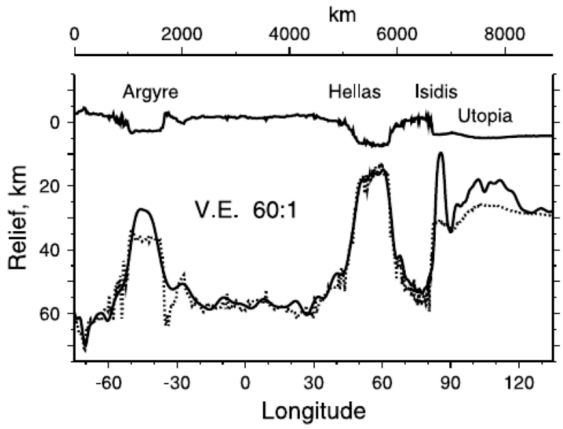

Figure 7.3: The profiles of surface height and model depth of Moho along a great circle through Argyre, Hellas, Isidis, and Utopia by Neumann et al. (2004). The dashed curve shows the Moho with local isostasy.

7.3. The FEM model

In this section, results of applying simple loads to the FEM model are elaborated. Results from the PN-load case (subsection 5.3.1) shows how different models of local isostasy are implemented to the FEM model and respond to the loads. The LDP-load case (subsection 5.3.2) shows how different flexural isostatic models behave in the FEM model.

7.3.1. Implementation of Local Isostasy

In subsection 5.3.1, models of Airy's and Pratt's isostasy are implemented in Abaqus with the approaches discussed in section 4.3. Figure 5.6 shows that under the loads, which would only result in radial faults with respect to the centers of the loads. This does agree with the fact that complex faulting patterns are observed on the surface of Mars because it only shows the faults induced by surface loading. The formation of faults is not only affected by loading from the surface but also influenced by loading underneath (mantle dynamics), volcanism, regional tectonics, and other factors. This study only focuses on the influence from surface loads, isostatic compensation, and mantle dynamics (for Tharsis only).

Figure 5.7 compares the behaviors of the FEM model with no compensation, Airy's compensation and Pratt's compensation. When there is no compensation, the FEM model generates larger stresses in the crust to support the loads. The deviatoric buoyancy induced by local isostasy partially supports the loads, so the models with isostatic compensations do not require as much stresses as the non-compensated model.

It's important to note that local isostasy cannot be strictly modeled in Abaqus. Local isostasy ignores the interaction between neighboring columns, and the loads are purely supported by buoyancy. However, shear stresses between elements are always modeled in Abaqus, and they support the loads to maintain the equilibrium in the model.

7.3.2. Implementation of Flexural Isostasy

The effects of flexural isostasy on Mars have been discussed in subsection 3.1.2. By applying the flexural response functions of the thin shell or the infinite plate model, long-wavelength features can be preserved while short-wavelength ones are erased. This is illustrated in Figure 5.13 where the differences in crustal thickness between local and flexural isostasy are lower (about 5 km) under the long-wavelength load ($d2$=2000 km) but higher (about 18 km) under the short-wavelength load ($d1$=708 km).

Similar patterns in differences between the local and flexural models can be seen in Figure 5.14. However, the ratio between difference in stress and total stress at the centers of loads in Figure 5.14 is not as large as the ratio between the thickness difference and total thickness in Figure 5.13. In other words, a certain percentage of buoyancy difference at the crust-mantle boundary does not yield to the same amount (but a lower percentage) of stress difference in the FEM model. This may be caused by the shear stresses between elements in Abaqus (which eases the difference in buoyancy).

The difference between the thin shell model and the infinite plate model in the FEM model is also illustrated in subsection 5.3.2. Results from analytical models in both Figure 5.11 and Figure 5.13 suggest that the crustal thickness from the infinite plate model is over 10% higher than that of the thin shell model at the center of the large load ($d2$=2000 km). This results in about 10% higher deviatoric buoyancy in the infinite plate model than the thin shell model.

However, stress results from FEM model in Figure 5.15 show less than 1.25% (0.5/40) of difference in stresses between the infinite plate model and the thin shell model. This difference is so small that it is not visible in the faults characterization for the regions of interest. The reason could be that the flat geometry of the FEM model fits the infinite plate but does not simulate the thin shell properly.

7.3.3. Limitation

The flat Mars FEM model has several limitations. One is its geometry. Since it is flat, the model could not simulate the behavior of an elastic thin shell under long-wavelength loads. That is why only a little difference is observed between the stress states from the infinite plate and the thin shell. Another limitation concerns the choice of step in the model. The use of the geostatic step in Abaqus makes it easy to obtain a state of equilibrium and neglects geological time in the model. But such an equilibrium state may not apply to all selected regions. What is more, the geostatic step ensures the minimum deformation in all finite elements. If the deformation is too low, no useful information of strain can be derived from the model output.

8

Conclusion

In this thesis, the main research question is:

What information about the subsurface crustal structure of Mars can be revealed from the surface faults?

To answer this question, this thesis starts by comparing different crustal models for Mars and then implements the crustal models into a flat FEM model for Mars. After that, the modeled stress and strain are compared with the observed faults.

In the first part, different models of isostasy are studied. The difference in the flexural response functions between the models of local isostasy and the infinite plate model shows the effect of bending stresses. The divergence in the flexural response functions between the infinite plate model and the thin shell model comes from the membrane stresses.

Both infinite plate model and the thin shell model act like low-pass filters to Airy's isostasy which allow the local compensation at low degree remain. But the degree of compensation at low degree is even lower in the thin shell model than the infinite plate because the former one also considers the curvature of the planet. This would enable the lithosphere to partially support the large wavelength load.

Applying the thin shell model to both Mars and Earth results in different shapes of the flexural response function. Mars appears to have a relatively more rigid lithosphere than the Earth. The major reasons behind it could be: firstly, Mars is smaller than Earth and has a larger curvature; secondly, Mars is thought to have one single plate while Earth's lithosphere is consisted of multiple pieces.

The power spectrum of the gravity signal of Martian topography with flexural compensations nicely explains the observed spectrum of the FAA. From the power spectrum analysis, the thin shell model with a T_e of 158 km is found to be the best crustal model globally for $2 \leqq n \leqq 90$. For $5 \leqq n \leqq 90$ where the degrees affected by mantle dynamics are excluded, the infinite plate model with a T_e of 136 km outperforms the thin shell model. Compared to the value of 34 km found by Watts and Moore (2017) for Earth, the value of T_e for Mars suggests that Mars has a more rigid lithosphere than Earth.

Varying Young's modulus, Poisson's ratio and the density contrast also change the best-fitting T_e. By decreasing Young's modulus from 100 GPa to 1 GPa, the corresponding best-fitting T_e increases from around 120 km to 580 km. A recent seismic study (Khan et al., 2021) indicates that Mars has a 500 km-thick lithosphere. This corresponds to a Young's modulus of about 2 GPa in Figure 6.4. Compared to a typical value of 100 GPa in previous studies (Belleguic et al., 2005, McGovern et al., 2002, Neumann et al., 2004), the lower value estimated in this study suggests that the values of Young's modulus have been overestimated.

In the second part, FEM models are constructed to investigate the regions of interest. Several simple loading cases are studied to check the performance of the FEM model. They show that proposed approaches are able to implement isostasy into the FEM model. It is found that Abaqus cannot strictly simulate the models of local isostasy due to the presence of shear stresses between neighboring elements.

The target regions are the Tharsis Rise, Hellas Basin and Utopia Basin. For the Tharsis Rise, both the volcanic constructed lithosphere and the support from the deep mantle plume played a role in the formation of the region and the surface faults. It is found that the underneath mantle plume may experience a reversal from upwelling to downwelling. Such a reversal from the bottom changes the property of the surface stress and results in the surface faults distribution today.

It is found that the Hellas Basin is under large tensional stresses. These stresses could not explain the presence of surface faults but the corresponding surface strains are consistent with the faults distribution around Hellas Basin. The calculated strains match the observed faults so well that it could support the claim that the Hellas Basin is in isostatic equilibrium.

Unlike the Hellas Basin, the surface faults on the Utopia Basin can not be explained by results from a flat isostatic-equilibrium FEM model. Neumann et al. (2004) suggest that, instead of isostatic equilibrium, the Utopia Basin is overcompensated and experiences a super-isostatic lift in its crust. Such an extra support from mantle plume also explains the observed compressional faults around the Utopia.

In summary, both isostatic compensation and dynamic mantle support could affect the faults formation on the surface of Mars. The amount of isostatic compensation and the state of the mantle plume (upwards or downwards, strong or weak) are region-dependent.

9

Recommendation

Based on the research conducted in this thesis, the following recommendations are established for future research.

Firstly, a spherical FEM model which incorporates the crustal structure of Mars is desired. With a spherical geometry, the model could better simulate the planet, especially in the long-wavelength. Many spherical models have been developed to study the GIA on Earth (Casteren, 2018, Nield et al., 2020, Van der Wal, 2009), and Blank (2015) developed a spherical FEM model for Mars. These spherical models can be adapted for Mars or other planets. The challenge of building a realistic spherical FEM model for Mars is how to incorporate the complex crustal structure and load the topography in a spherical geometry. The practices from the flat model cannot be used directly because the flat model is in Cartesian coordinates not spherical coordinates, and the state of isostatic equilibrium might also be different in the spherical coordinates (Hemingway and Matsuyama, 2017).

Secondly, it would be interesting to further investigate bottom loading of the Tharsis Rise in the FEM Mars model. In this study, the effects of some roughly estimated super-plumes under the Tharsis region are studied. The bottom loading on the crust-mantle boundary together with topography loading on the surface could reveal useful information about the evolution of the Tharsis bulge. More information about this topic can be found in the MSc thesis of Van der Tang (2021).

Thirdly, the effects of varying crustal thickness and density could be further investigated. This study takes the deviatoric buoyancy approach and neglect the variations in crustal thickness and density. Nield et al. (2018) investigated a flat FEM Earth model with lateral variations in lithospheric thickness. And they found that these variations are important if one wants to capture short-wavelength deformation on Earth. So, applying the spatial variations in crustal thickness or density could improve the accuracy of the FEM model.

Lastly, the geostatic step could be replaced by time-dependent steps in the FEM model. The geostatic step only yields to a state of equilibrium. By using time-dependent steps, such as the visco step, one could investigate the evolution of target regions. The challenge of this recommendation is how to obtain the loading history on Mars.

A

Supplement Equations

The Laplacian operator is given by

$$\nabla^2 \equiv \frac{\partial^2}{\partial \phi^2} + \cot\phi \frac{\partial}{\partial \phi} + \csc^2\phi \frac{\partial^2}{\partial \psi^2} \tag{A.1}$$

where ϕ and ψ are the colatitude and longitude, respectively. And $\left(\nabla^2\right)'$ is defined as (Beuthe, 2008)

$$\left(\nabla^2\right)' = \nabla^2 + 2. \tag{A.2}$$

The Laplacian operator in spherical harmonic domain for a given function $Y_{\ell m}(\Omega)$ is (Audet, 2014)

$$\nabla^2 Y_{\ell m}(\Omega) = -\ell(\ell+1) Y_{\ell m}(\Omega). \tag{A.3}$$

The loading height h in Equation 3.12 is defined by

$$h = h_0 - \frac{\rho_m}{\rho_c} h_g \tag{A.4}$$

where h_0 is the original height of topography, h_g is displacement of the geoid caused by extra mass from topography.

The flexural response function of the thin shell models (Equation 3.27) can be rewritten into a similar format to that of the infinite plate (Equation 3.7) in three steps. Firstly, replacing both τ and σ in Equation 3.27 with Equation 3.14 and 3.15 and inverting both sides. This would change origin equation into

$$\frac{1}{\Phi(n)_{shell}} = 1 + \frac{\frac{ET_e^3}{12(1-v^2)}[n^3(n+1)^3 - 4n^2(n+1)^2 + 4n(n+1)] + ET_eR^2[n(n+1)-2]}{R^4(\rho_m - \rho_c)g[n(n+1)-(1-v)]}. \tag{A.5}$$

Secondly, substituting relevant terms with the flexural parameter D (Equation 3.8) in Equation A.5, this yields

$$\frac{1}{\Phi(n)_{shell}} = 1 + \frac{D}{(\rho_m - \rho_c)g}\left(\frac{1}{R^4}\frac{[n(n+1)-2]^2}{1-\frac{1-v}{n(n+1)}} + \frac{12(1-v^2)}{T_e^2R^2}\frac{1-\frac{2}{n(n+1)}}{1-\frac{1-v}{n(n+1)}}\right). \tag{A.6}$$

Lastly, inverting both sides in the Equation A.6, one can have Equation 3.28.

Spherical Harmonics $Y_{nm}(\theta,\phi)$ is the spherical harmonic function for degree n and order m, which is expressed as (Wieczorek, 2015)

$$Y_{nm}(\theta,\phi) = \begin{cases} \bar{P}_{nm}(\cos\theta)\cos m\phi & \text{if } m \geq 0 \\ \bar{P}_{n|m|}(\cos\theta)\sin|m|\phi & \text{if } m < 0 \end{cases} \tag{A.7}$$

where $\bar{P}$ is the Legendre functions after normalisation

$$\bar{P}_{nm}(\mu) = \sqrt{(2-\delta_{0m})\,(2n+1)\frac{(n-m)!}{(n+m)!}}P_{nm}(\mu) \tag{A.8}$$

in which δ_{ij} represents the Kronecker delta function.

The de-normalised Legendre functions are associated with the Legendre polynomials by

$$P_{nm}(\mu) = \left(1-\mu^2\right)^{m/2}\frac{\mathrm{d}^m}{\mathrm{d}\mu^m}P_n(\mu) \tag{A.9}$$

$$P_n(\mu) = \frac{1}{2^n n!}\frac{\mathrm{d}^n}{\mathrm{d}\mu^n}\left(\mu^2-1\right)^n. \tag{A.10}$$

B

Supplement Figures

Boundary effect studies for the Hellas Basin

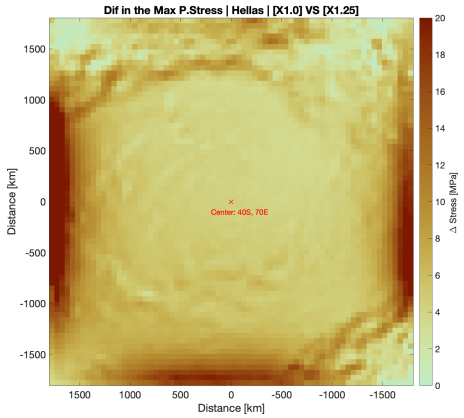

(a) Difference in the magnitude.

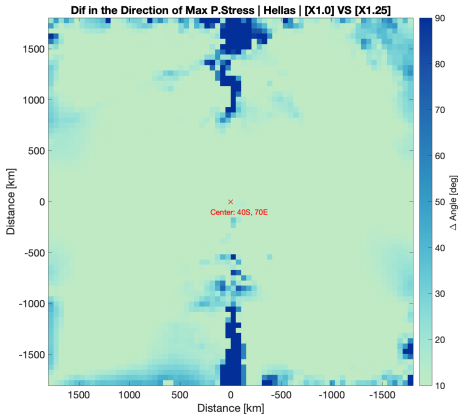

(b) Difference in the direction.

Figure B.1: The difference in the magnitude and direction of the maximum principal stresses between the ×1 and ×1.25 models.

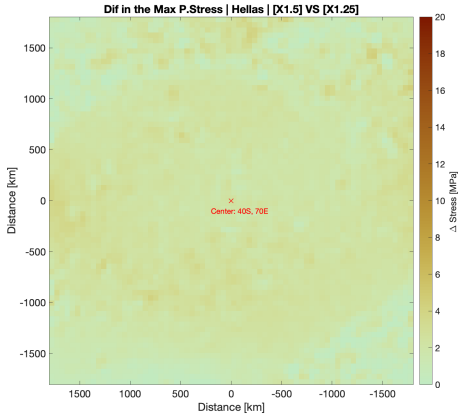

(a) Difference in the magnitude.

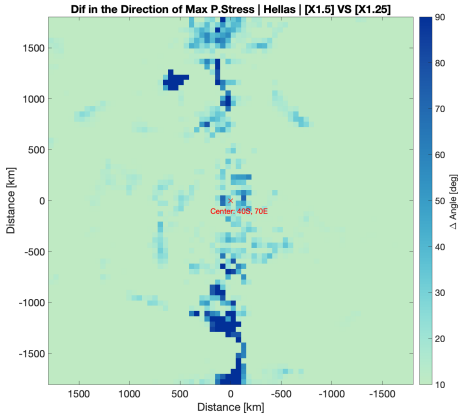

(b) Difference in the direction.

Figure B.2: The difference in the magnitude and direction of the maximum principal stresses between the ×1.25 and ×1.5 models.

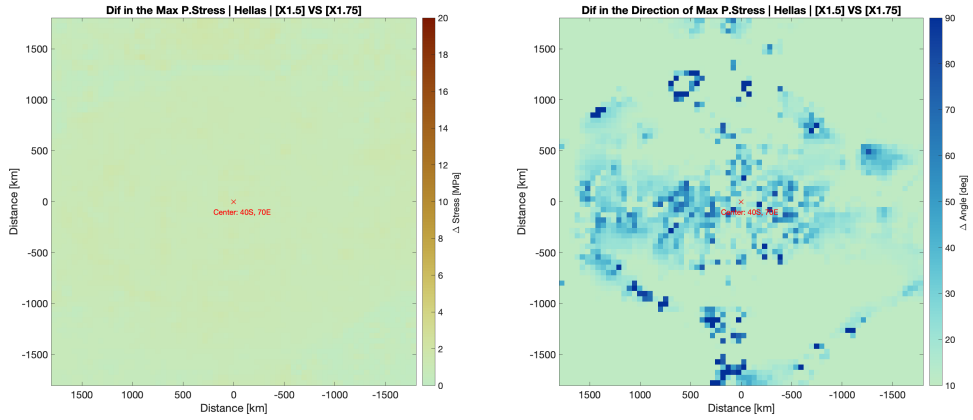

(a) Difference in the magnitude. (b) Difference in the direction.

Figure B.3: The difference in the magnitude and direction of the maximum principal stresses between the ×1.5 and ×1.75 models.

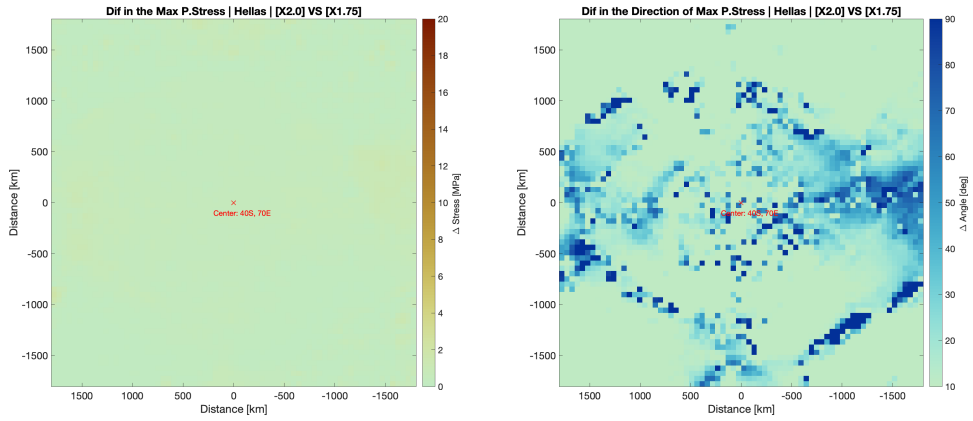

(a) Difference in the magnitude. (b) Difference in the direction.

Figure B.4: The difference in the magnitude and direction of the maximum principal stresses between the ×1.75 and ×2 models.

Boundary effect studies for the Utopia Basin

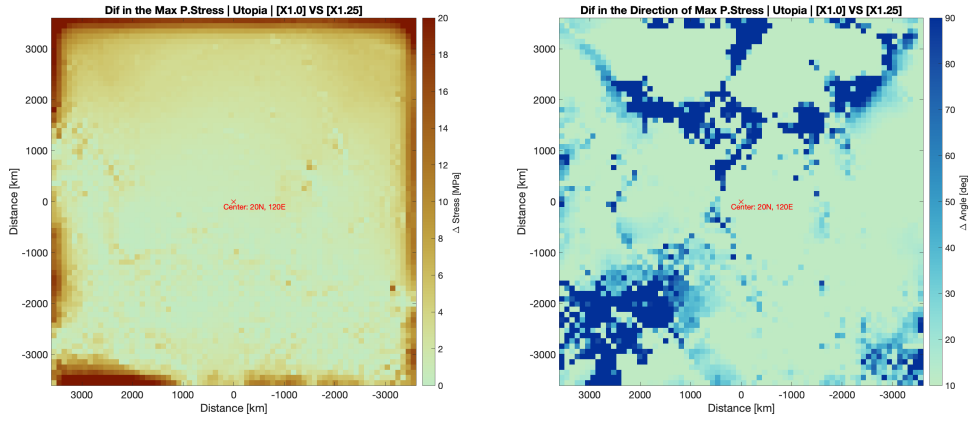

(a) Difference in the magnitude. (b) Difference in the direction.

Figure B.5: The difference in the magnitude and direction of the maximum principal stresses between the ×1 and ×1.25 models.

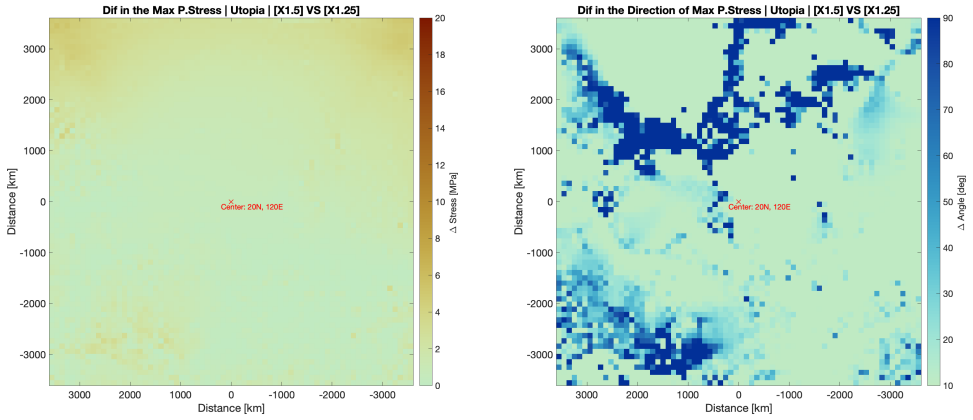

(a) Difference in the magnitude. (b) Difference in the direction.

Figure B.6: The difference in the magnitude and direction of the maximum principal stresses between the ×1.25 and ×1.5 models.

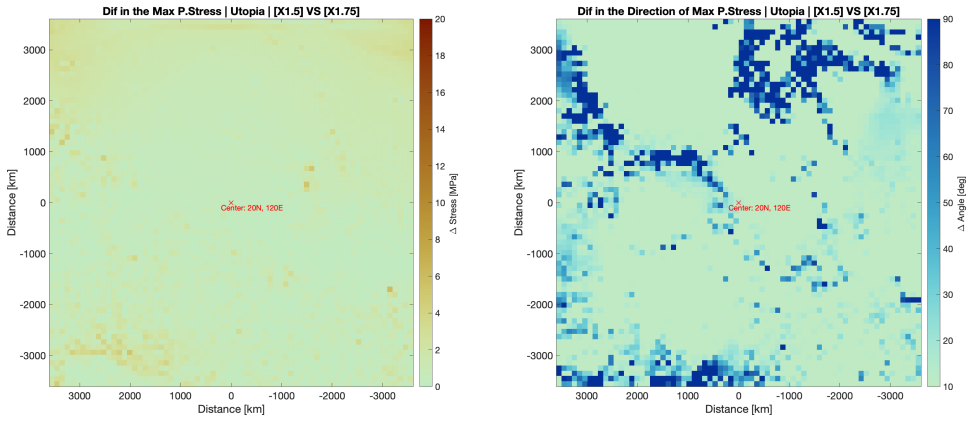

(a) Difference in the magnitude. (b) Difference in the direction.

Figure B.7: The difference in the magnitude and direction of the maximum principal stresses between the ×1.5 and ×1.75 models.

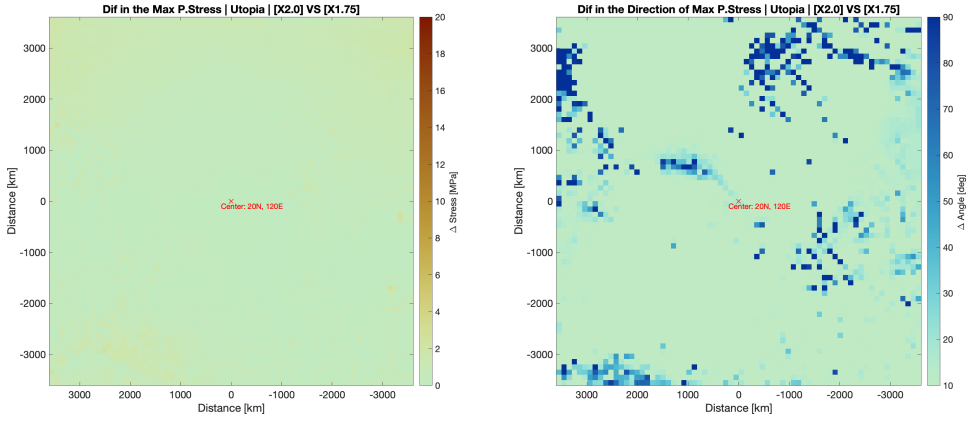

(a) Difference in the magnitude. (b) Difference in the direction.

Figure B.8: The difference in the magnitude and direction of the maximum principal stresses between the ×1.75 and ×2 models.

Results from FEM models:

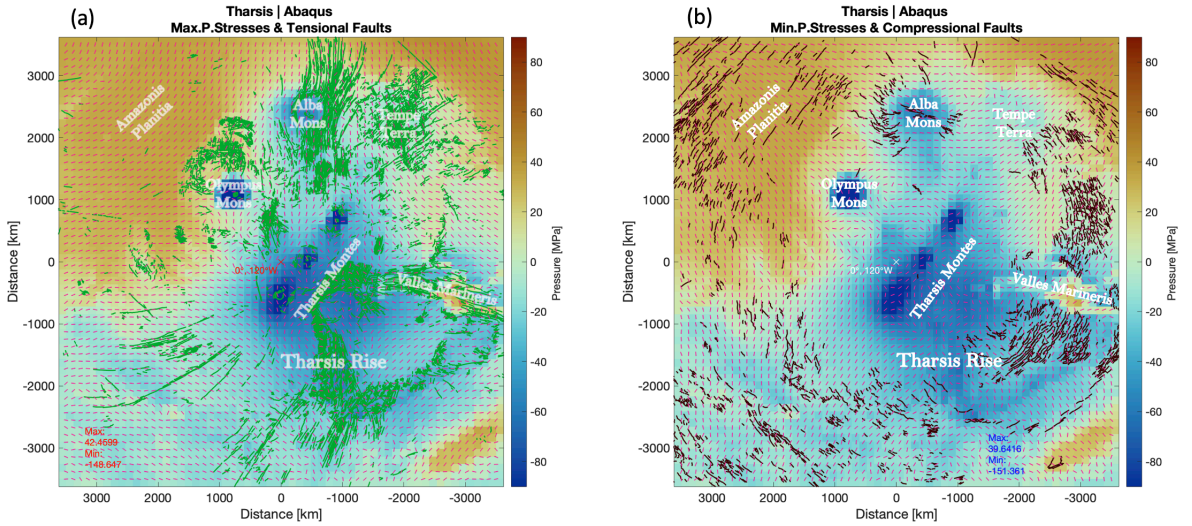

Figure B.9: Maximum principal stresses (a) and minimum principal stresses (b) for the Tharsis Rise region with no isostatic compensation (pure Abaqus). Tensional (green) and compressional (brown) faults are also plotted. The arrows indicate the direction of the principal stresses.

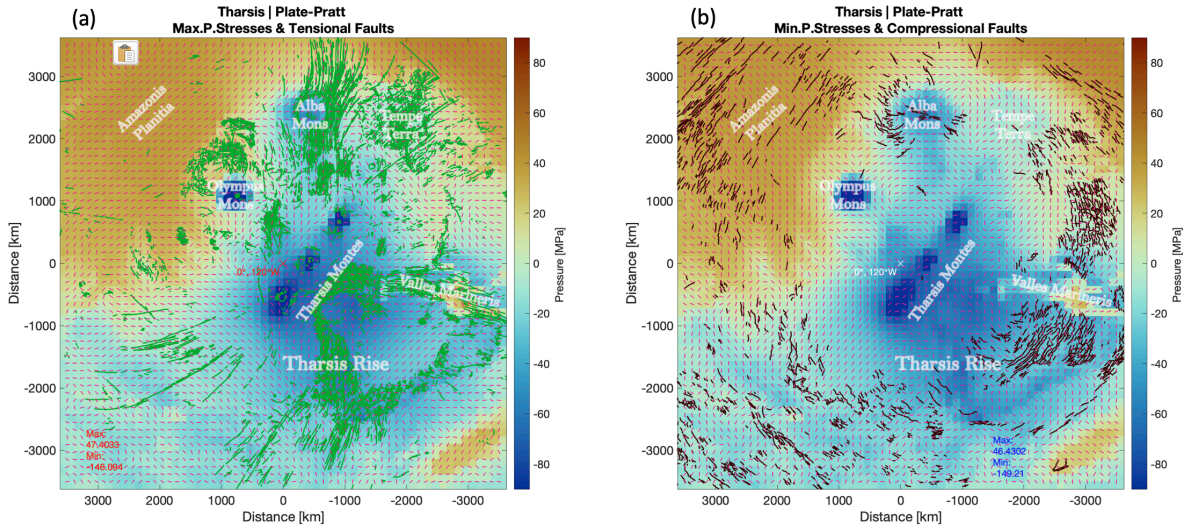

Figure B.10: Maximum principal stresses (a) and minimum principal stresses (b) for the Tharsis Rise region with Flexural Isostasy. Tensional (green) and compressional (brown) faults are also plotted.

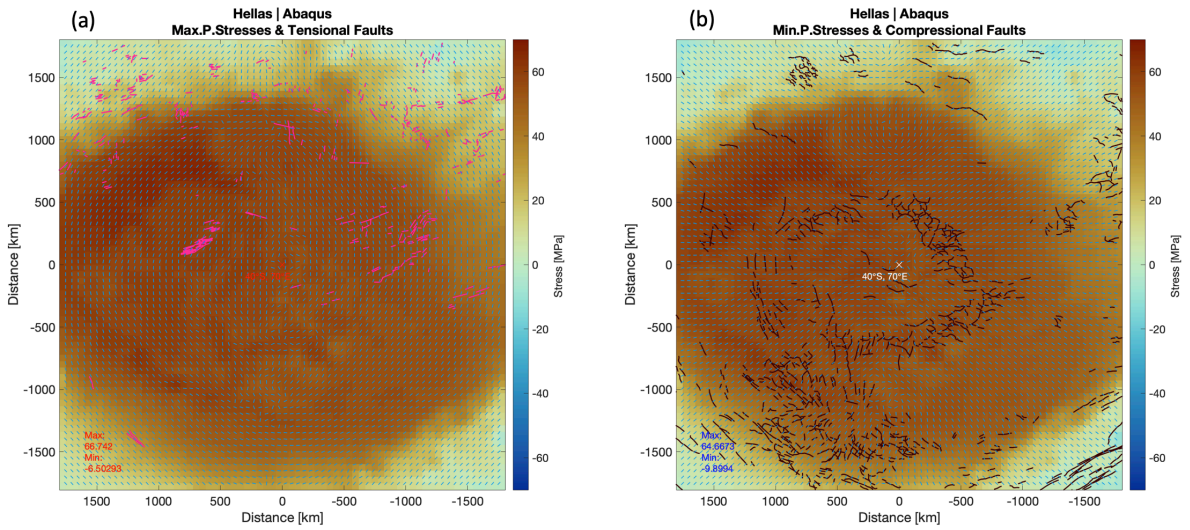

Figure B.11: Maximum principal stresses (a) and minimum principal stresses (b) for the Hellas Basin region with no isostatic compensation (pure Abaqus). Tensional (green) and compressional (brown) faults are also plotted. The arrows indicate the direction of the principal stresses.

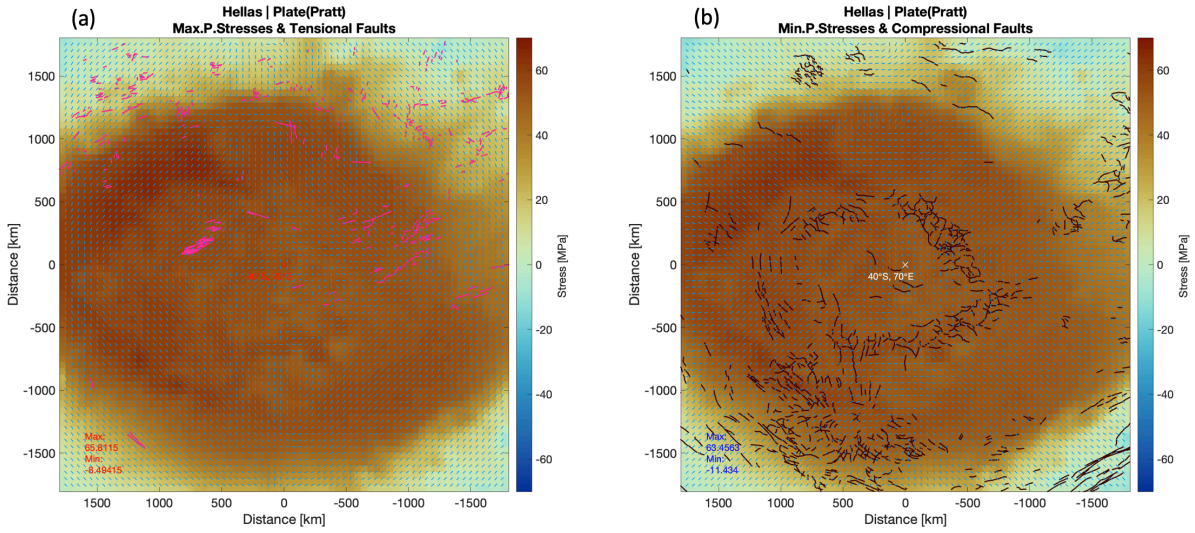

Figure B.12: Maximum principal stresses (a) and minimum principal stresses (b) for the Hellas Basin region with Flexural Isostasy. Tensional (green) and compressional (brown) faults are also plotted.

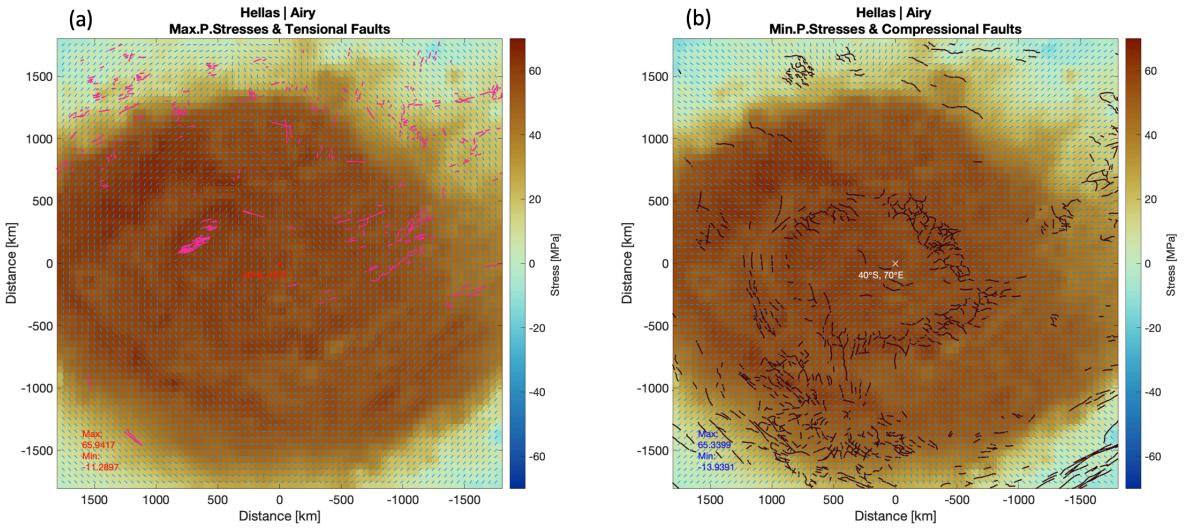

Figure B.13: Maximum principal stresses (a) and minimum principal stresses (b) for the Hellas Basin region with Airy's Isostasy. Tensional (green) and compressional (brown) faults are also plotted.

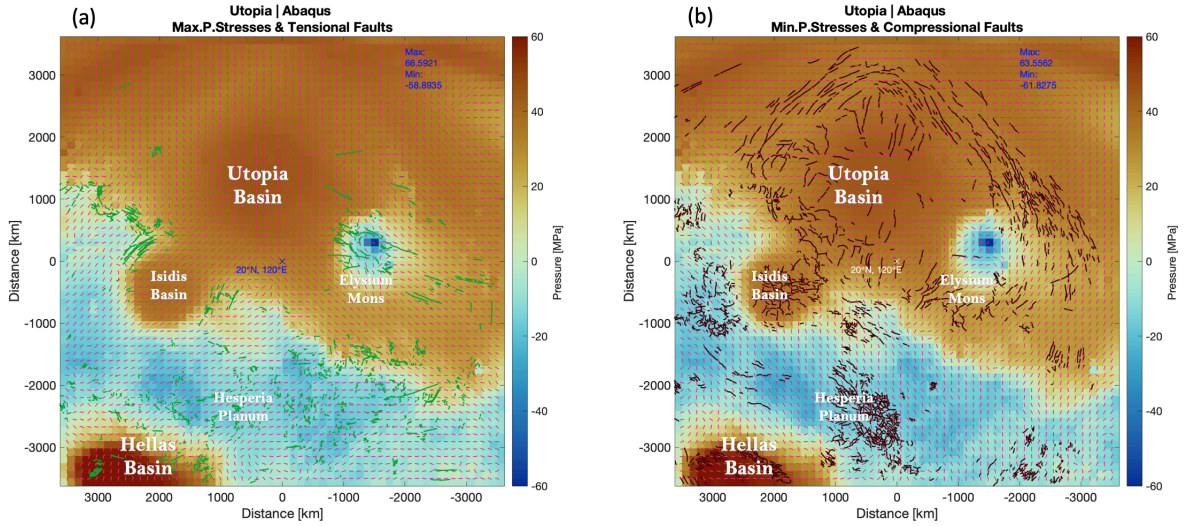

Figure B.14: Maximum principal stresses (a) and minimum principal stresses (b) for the Hellas Basin region with no isostatic compensation (pure Abaqus). Tensional (green) and compressional (brown) faults are also plotted. The arrows indicate the direction of the principal stresses.

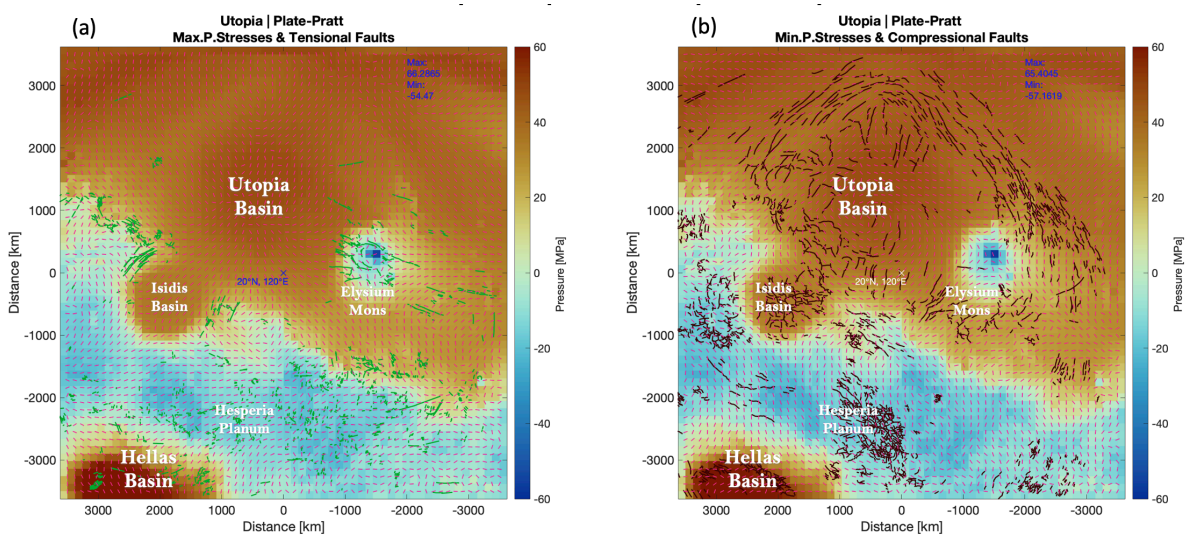

Figure B.15: Maximum principal stresses (a) and minimum principal stresses (b) for the Hellas Basin region with Flexural Isostasy. Tensional (green) and compressional (brown) faults are also plotted.

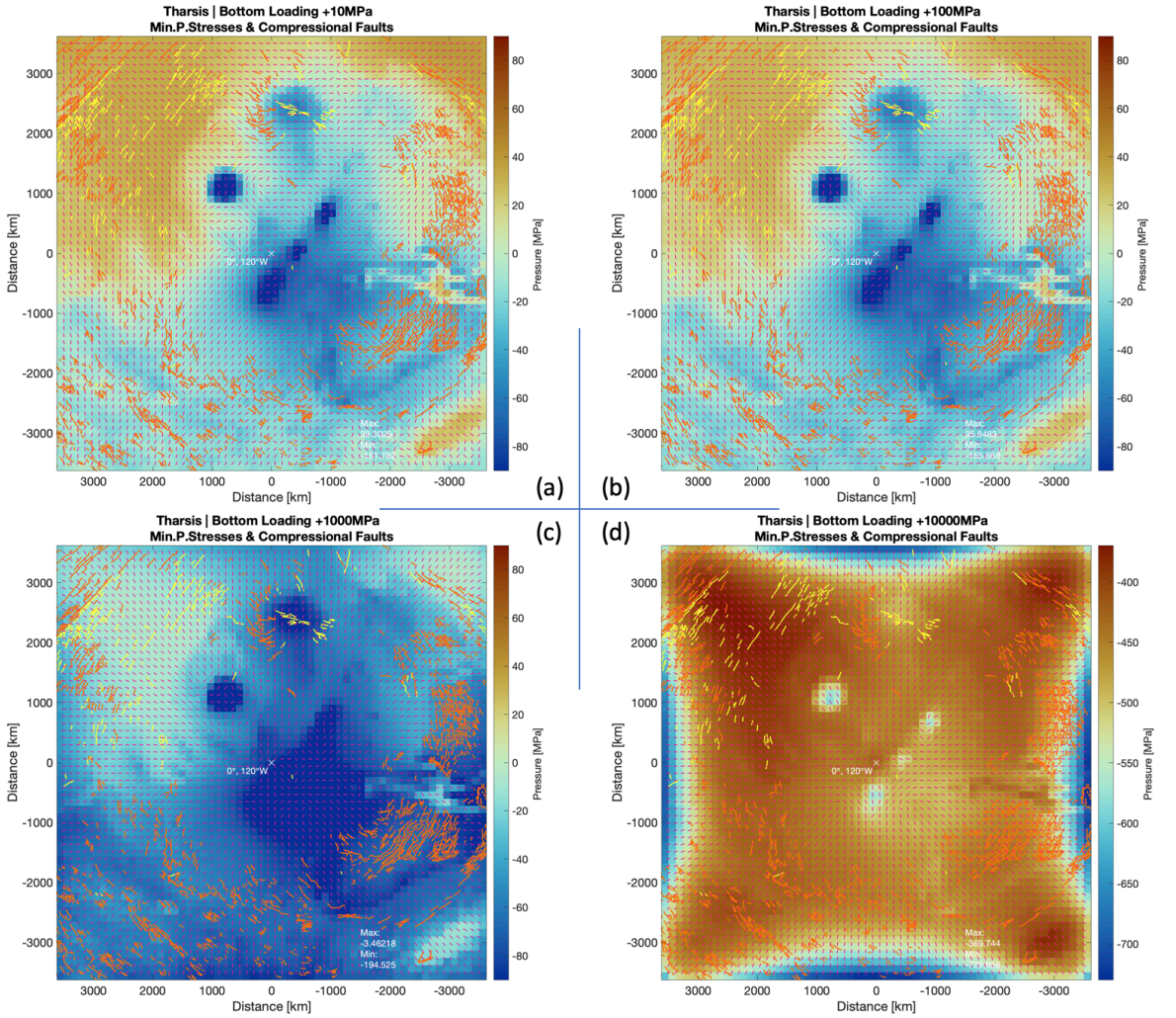

Figure B.16: Minimum principal strains and compressional faults for the Tharsis Rise region with positive bottom loads (a:+10MPa, b:++100MPa, c:+1000MPa, d:+10000MPa).

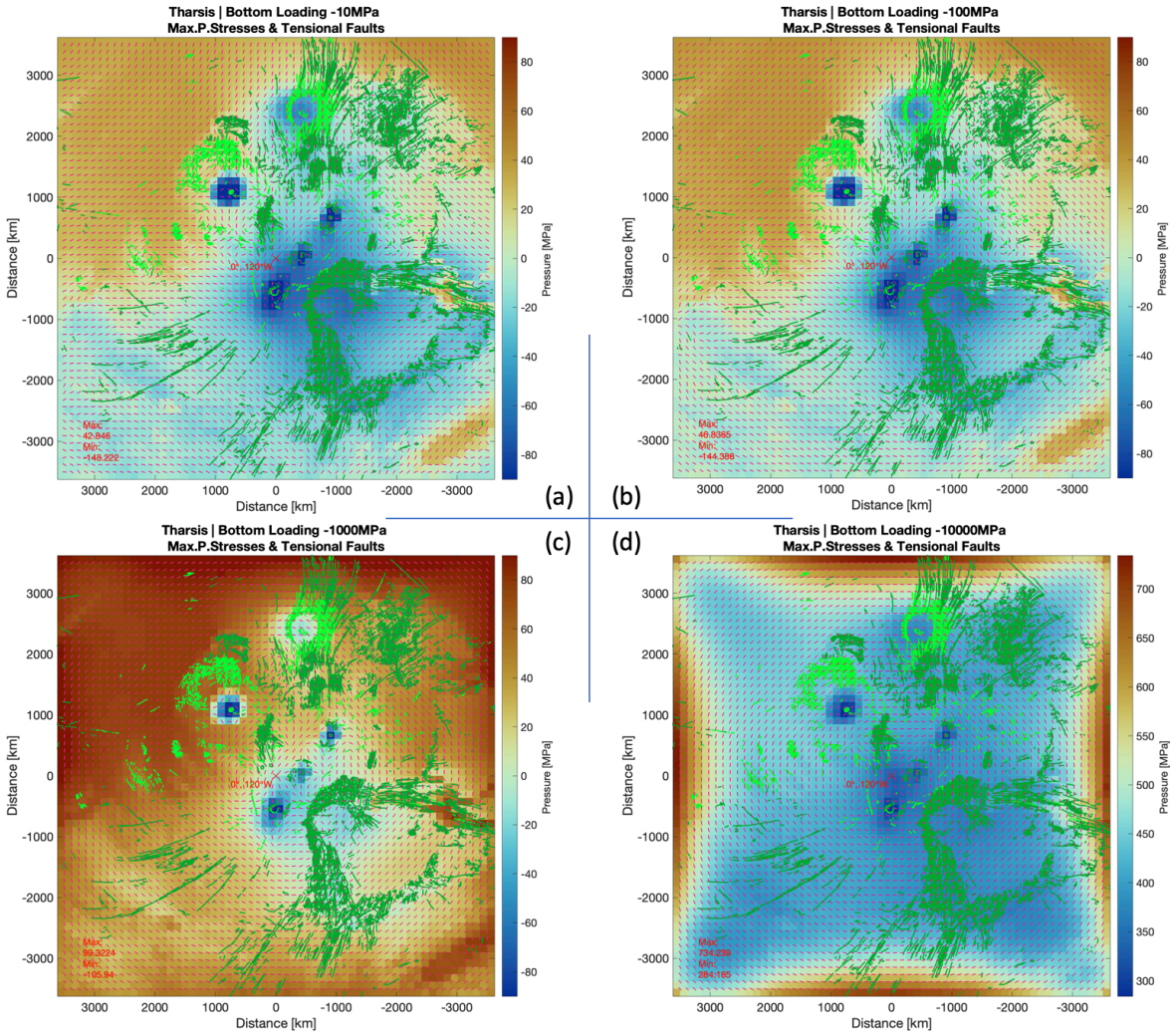

Figure B.17: Maximum principal strains and tensional faults for the Tharsis Rise region with negative bottom loads (a:-10MPa, b:-100MPa, c:-1000MPa, d:-10000MPa).

Bibliography

Airy, G. On the computation of the effect of the attraction of mountain-masses, as disturbing the apparent astronomical latitude of stations in geodetic surveys. *Philosophical Transactions*, 145:101–105, 1855. doi: 10.1098/rstl.1855.0003. URL https://royalsocietypublishing.org/doi/10.1098/rstl.1855.0003.

Anderson, R. C., J. M. Dohm, M. P. Golombek, A. F. C. Haldemann, B. J. Franklin, K. L. Tanaka, J. Lias, and B. Peer. Primary centers and secondary concentrations of tectonic activity through time in the western hemisphere of Mars. *Journal of Geophysical Research: Planets*, 106(E9):20563–20585, September 2001. ISSN 01480227. doi: 10.1029/2000JE001278. URL http://doi.wiley.com/10.1029/2000JE001278.

Andrews-Hanna, J. C., M. T. Zuber, and S. A. Hauck. Strike-slip faults on Mars: Observations and implications for global tectonics and geodynamics. *Journal of Geophysical Research*, 113 (E8):E08002, August 2008. ISSN 0148-0227. doi: 10.1029/2007JE002980. URL http://doi.wiley.com/10.1029/2007JE002980.

Audet, P. Toward mapping the effective elastic thickness of planetary lithospheres from a spherical wavelet analysis of gravity and topography. *Physics of the Earth and Planetary Interiors*, page 35, 2014.

Backer, D. L. Seismic analysis of Mars using gravitational potential stresses - InSight. Master's thesis, TU Delft, 2018. URL https://repository.tudelft.nl/islandora/object/uuid%3A9b62bef7-b3a0-4dd3-8a84-462bdd07b720.

Banerdt, W. B. Support of long-wavelength loads on Venus and implications for internal structure. *Journal of Geophysical Research*, 91(B1):403–419, 1986. doi: 10.1029/JB091iB01p00403.

Banerdt, W. and M. Golombek. Tectonics of the tharsis region of mars: Insights from mgs topography and gravity. *Lunar and Planetary Science*, 2000.

Batov, A. V., T. V. Gudkova, and V. N. Zharkov. Nonhydrostatic Stress State in the Martian Interior for Different Rheological Models. *Izvestiya, Physics of the Solid Earth*, 55(4):688–700, July 2019. ISSN 1069-3513, 1555-6506. doi: 10.1134/S1069351319040025. URL http://link.springer.com/10.1134/S1069351319040025.

Belleguic, V., M. Wieczorek, and P. Lognonne. WHAT CAN BE LEARNED ABOUT THE MARTIAN LITHOSPHERE FROM GRAVITY AND TOPOGRAPHY DATA?. page 2, 2004.

Belleguic, V., P. Lognonné, and M. Wieczorek. Constraints on the Martian lithosphere from gravity and topography data. *Journal of Geophysical Research*, 110(E11), 2005. ISSN 0148-0227. doi: 10.1029/2005JE002437. URL http://doi.wiley.com/10.1029/2005JE002437.

Beuthe, M., S. Le Maistre, P. Rosenblatt, M. Pätzold, and V. Dehant. Density and lithospheric thickness of the Tharsis Province from MEX MaRS and MRO gravity data: DENSITY AND LITHOSPHERE OF THARSIS. *Journal of Geophysical Research: Planets*, 117(E4):n/a–n/a, April 2012. ISSN 01480227. doi: 10.1029/2011JE003976. URL http://doi.wiley.com/10.1029/2011JE003976.

Beuthe, M. Thin elastic shells with variable thickness for lithospheric flexure of one-plate planets. *Geophysical Journal International*, 172(2):817–841, February 2008. ISSN 0956540X, 1365246X. doi: 10.1111/j.1365-246X.2007.03671.x. URL http://arxiv.org/abs/0704.1627. arXiv: 0704.1627.

Beuthe, M. Isostasy with Love: I Elastic equilibrium. *arXiv:2011.15097 [astro-ph, physics:physics]*, November 2020. URL http://arxiv.org/abs/2011.15097. arXiv: 2011.15097.

Blank, B. Finding faults with FEM. Master's thesis, TU Delft, 2015.

Cain, D. L., A. Kliore, B. Seidel, and M. Sykes. The Shape of Mars from the Mariner 90ccultations. *Icarus*, 17(2):517–524, 1972.

Carr, M. H. and J. W. Head. Geologic history of mars. *Earth and Planetary Science Letters*, 294 (3-4):185–203, June 2010. ISSN 0012821X. doi: 10.1016/j.epsl.2009.06.042. URL https://linkinghub.elsevier.com/retrieve/pii/S0012821X09003847.

Casteren, R. v. A 3d glacial isostatic adjustment model for northwestern europe. Master's thesis, TU Delft, 2018.

Cottaar, S. and P. Koelemeijer. The interior of Mars revealed. *Science*, 373(6553):388–389, July 2021. ISSN 0036-8075, 1095-9203. doi: 10.1126/science.abj8914. URL https://www.sciencemag.org/lookup/doi/10.1126/science.abj8914.

Dahlen, F. A. Isostatic geoid anomalies on a sphere. *Journal of Geophysical Research*, 87(B5):3943–3948, 1982. doi: 10.1029/JB087iB05p03943.

David, C. Isostasy and Gravity Modelling: Integrating Potential Field Data in Interpretation Workflows. *Recorder*, 35(60), 2010. URL https://csegrecorder.com/articles/view/isostasy-and-gravity-modelling-integrating-potential-field-data.

Downs, G. S., P. J. Mouginis-Mark, S. H. Zisk, and T. W. Thompson. New radar-derived topography for the northern hemisphere of Mars. *Journal of Geophysical Research*, 87(B12):9747, 1982. ISSN 0148-0227. doi: 10.1029/JB087iB12p09747. URL http://doi.wiley.com/10.1029/JB087iB12p09747.

Fowler, C. M. R. *The solid earth: an introduction to global geophysics*. Cambridge University Press, Cambridge, UK ; New York, 2nd ed edition, 2005. ISBN 978-0-521-89307-7 978-0-521-58409-8.

Gaianauta. Isostatic vertical motions of the lithosphere, 2015. URL https://en.wikipedia.org/wiki/Isostasy.

Genova, A., S. Goossens, F. G. Lemoine, E. Mazarico, G. A. Neumann, D. E. Smith, and M. T. Zuber. Seasonal and static gravity field of Mars from MGS, Mars Odyssey and MRO radio science. *Icarus*, 272:228–245, July 2016. ISSN 00191035. doi: 10.1016/j.icarus.2016.02.050. URL https://linkinghub.elsevier.com/retrieve/pii/S0019103516001287.

Gere, J. and B. Goodno. *Mechanics of Materials*. Cengage Learning, 2012. ISBN 9781111577735. URL https://books.google.nl/books?id=VQDAsEHAH-AC.

Golombek, M. P. and R. J. Phillips. Mars tectonics. In *Planetary Tectonics*. Cambridge University Press., 2010.

Heap, M. J., M. Villeneuve, F. Albino, J. I. Farquharson, E. Brothelande, F. Amelung, J.-L. Got, and P. Baud. Towards more realistic values of elastic moduli for volcano modelling. *Journal of Volcanology and Geothermal Research*, 390:106684, January 2020. ISSN 03770273. doi: 10.1016/j.jvolgeores.2019.106684. URL https://linkinghub.elsevier.com/retrieve/pii/S0377027319304044.

Helwa, O. Components stress tensor cartesian, 2009. URL https://commons.wikimedia.org/wiki/File:Components_stress_tensor_cartesian.svg.

Hemingway, D. J. and I. Matsuyama. Isostatic equilibrium in spherical coordinates and implications for crustal thickness on the Moon, Mars, Enceladus, and elsewhere: ISOSTASY ON A SPHERE. *Geophysical Research Letters*, 44(15):7695–7705, August 2017. ISSN 00948276. doi: 10.1002/2017GL073334. URL http://doi.wiley.com/10.1002/2017GL073334.

Hirt, C., S. J. Claessens, and W. Featherstone. Kilometer-resolution gravity field of mars: Mgm2011. *Planetary and Space Science*, 67:147–154, 2012. doi: 10.1016/j.pss.2012.02.006.

Jeffreys, H. The stress-differences in the earth's shell. *Geophysical Journal International*, 5:101–105, 1943. doi: 10.1111/j.1365-246X.1943.tb00344.x. URL https://doi.org/10.1111/j.1365-246X.1943.tb00344.x.

Jeffreys, H. *The Earth*. Cambridge University Press, Cambridge, United Kingdom, 4th edition edition, 1959.

Kalousová, K., O. Souček, and O. Čadek. Deformation of an elastic shell with variable thickness: a comparison of different methods: Deformation of an elastic shell. *Geophysical Journal International*, 190(2):726–744, August 2012. ISSN 0956540X. doi: 10.1111/j.1365-246X.2012.05539.x. URL https://academic.oup.com/gji/article-lookup/doi/10.1111/j.1365-246X.2012.05539.x.

Kaula, W. M. Geophysical implications of satellite determinations of the earth's gravitational field. *Space Science Reviews*, 7(5-6):769–794, December 1967. ISSN 0038-6308, 1572-9672. doi: 10.1007/BF00542895. URL http://link.springer.com/10.1007/BF00542895.

Khan, A., S. Ceylan, M. van Driel, D. Giardini, P. Lognonné, H. Samuel, N. C. Schmerr, S. C. Stähler, A. C. Duran, Q. Huang, D. Kim, A. Broquet, C. Charalambous, J. F. Clinton, P. M. Davis, M. Drilleau, F. Karakostas, V. Lekic, S. M. McLennan, R. R. Maguire, C. Michaut, M. P. Panning, W. T. Pike, B. Pinot, M. Plasman, J.-R. Scholz, R. Widmer-Schnidrig, T. Spohn, S. E. Smrekar, and W. B. Banerdt. Upper mantle structure of Mars from InSight seismic data. *Science*, 373 (6553):434–438, July 2021. ISSN 0036-8075, 1095-9203. doi: 10.1126/science.abf2966. URL https://www.sciencemag.org/lookup/doi/10.1126/science.abf2966.

Knapmeyer, M., J. Oberst, E. Hauber, M. Wählisch, C. Deuchler, and R. Wagner. Working models for spatial distribution and level of Mars' seismicity. *Journal of Geophysical Research*, 111(E11):E11006, November 2006. ISSN 0148-0227. doi: 10.1029/2006JE002708. URL http://doi.wiley.com/10.1029/2006JE002708.

Knapmeyer, M., S. Schneider, M. Misun, M. Wahlisch, and E. Hauber. An extended global Inventory of Mars Surface Faults. *Geophysical Research Abstracts*, 10, 2008.

Knapmeyer-Endrun, B., M. P. Panning, F. Bissig, R. Joshi, A. Khan, D. Kim, V. Lekić, B. Tauzin, S. Tharimena, M. Plasman, N. Compaire, R. F. Garcia, L. Margerin, M. Schimmel, □. Stutzmann, N. Schmerr, E. Bozdağ, A.-C. Plesa, M. A. Wieczorek, A. Broquet, D. Antonangeli, S. M. McLennan, H. Samuel, C. Michaut, L. Pan, S. E. Smrekar, C. L. Johnson, N. Brinkman, A. Mittelholz, A. Rivoldini, P. M. Davis, P. Lognonné, B. Pinot, J.-R. Scholz, S. Stähler, M. Knapmeyer, M. van Driel, D. Giardini, and W. B. Banerdt. Thickness and structure of the martian crust from InSight seismic data. *Science*, 373(6553):438–443, July 2021. ISSN 0036-8075, 1095-9203. doi: 10.1126/science.abf8966. URL https://www.sciencemag.org/lookup/doi/10.1126/science.abf8966.

Konopliv, A. S., S. W. Asmar, W. M. Folkner, O. Karatekin, D. C. Nunes, S. E. Smrekar, C. F. Yoder, and M. T. Zuber. Mars high resolution gravity fields from MRO, Mars seasonal gravity, and other dynamical parameters. *Icarus*, 211(1):401–428, January 2011. ISSN 00191035. doi: 10.1016/j.icarus.2010.10.004. URL https://linkinghub.elsevier.com/retrieve/pii/S0019103510003830.

Kraus, H. *Thin elastic shells : an introduction to the theoretical foundations and the analysis of their static and dynamic behavior*. John Wiley & Sons, New York, 1967.

Laskar, J., A. C. M. Correia, M. Gastineau, F. Joutel, B. Levrard, and P. Robutel. Long term evolution and chaotic diffusion of the insolation quantities of Mars. *Icarus*, 170(2):343–364, 2004.

Lindal, G., H. Hotz, D. Sweetnam, Z. Shippony, J. Brenkle, and G. Hartsell. Viking radio occultation measurements of the atmosphere and topography of Mars: Data acquired during 1 Martian year of tracking. *Journal of Geophysical Research*, 84(B14):8443–8456, 1979.

McGovern, P. J., S. C. Solomon, D. E. Smith, M. T. Zuber, M. Simons, M. A. Wieczorek, R. J. Phillips, G. A. Neumann, O. Aharonson, and J. W. Head. Localized gravity/topography admittance and correlation spectra on Mars: Implications for regional and global evolution: LOCALIZED ADMITTANCE

ON MARS. *Journal of Geophysical Research: Planets*, 107(E12):19–1–19–25, December 2002. ISSN 01480227. doi: 10.1029/2002JE001854. URL http://doi.wiley.com/10.1029/2002JE001854.

McGovern, P. J., S. C. Solomon, and D. E. Smith. Correction to "Localized gravity/topography admittance and correlation spectra on Mars: Implications for regional and global evolution". *Journal of Geophysical Research*, 109(E7):E07007, 2004. ISSN 0148-0227. doi: 10.1029/2004JE002286. URL http://doi.wiley.com/10.1029/2004JE002286.

Moore, P. The Mapping of Mars. *Journal of the British Astronomical Association*, 94(2):45–54, 1984.

Mussini, J. An anisotropic flexural isostasy method for investigating the Martian lithosphere. Master's thesis, TU Delft, 2020. URL https://repository.tudelft.nl/islandora/object/uuid%3A5d77cc6e-a4c5-433e-b898-d5e8b9f4d58d.

Neumann, G. A., M. T. Zuber, and M. A. Wieczorek. Crustal structure of Mars from gravity and topography. *Journal of Geophysical Research*, 109(E8):E08002, 2004. ISSN 0148-0227. doi: 10.1029/2004JE002262. URL http://doi.wiley.com/10.1029/2004JE002262.

Neumann, G. A., D. D. Rowlands, F. G. Lemoine, D. E. Smith, and M. T. Zuber. Crossover analysis of Mars Orbiter Laser Altimeter data. *Journal of Geophysical Research: Planets*, 106(E10): 23753–23768, October 2001. ISSN 01480227. doi: 10.1029/2000JE001381. URL http://doi.wiley.com/10.1029/2000JE001381.

Nicks, O. *A review of the Mariner IV results*. Number 130 in SP. National Aeronautics and Space Administration, Scientific and Technical Information Division, Office of Technology Utilization„ 1967.

Nield, G. A., P. L. Whitehouse, W. van der Wal, B. Blank, J. P. O'Donnell, and G. W. Stuart. The impact of lateral variations in lithospheric thickness on glacial isostatic adjustment in West Antarctica. *Geophysical Journal International*, 214(2):811–824, August 2018. ISSN 0956-540X, 1365-246X. doi: 10.1093/gji/ggy158. URL https://academic.oup.com/gji/article/214/2/811/4980921.

Nield, G. A., M. A. King, R. Steffen, and B. Blank. A global,spherical,finite-element model for post-seismic deformation using ABAQUS. preprint, Solid Earth, June 2020. URL https://gmd.copernicus.org/preprints/gmd-2020-107/.

Pavlis, N. K., S. A. Holmes, S. C. Kenyon, and J. K. Factor. The development and evaluation of the Earth Gravitational Model 2008 (EGM2008): THE EGM2008 EARTH GRAVITATIONAL MODEL. *Journal of Geophysical Research: Solid Earth*, 117(B4), April 2012. ISSN 01480227. doi: 10.1029/2011JB008916. URL https://onlinelibrary.wiley.com/doi/10.1029/2011JB008916.

Peters, W. The Appearance of Venus and Mars in 1610. *Journal for the History of Astronomy*, 15(3): 211–214, 1984.

Redmond, H. L. and S. D. King. A numerical study of a mantle plume beneath the Tharsis Rise: Reconciling dynamic uplift and lithospheric support models. *JOURNAL OF GEOPHYSICAL RESEARCH*, 109(E09008):14, 2004. doi: 10.1029/2003JE002228.

Rexer, M. and C. Hirt. Spectral analysis of the earth's topographic potential via 2D-DFT: a new data-based degree variance model to degree 90,000. *Journal of Geodesy*, 89(9):887–909, September 2015. ISSN 0949-7714, 1432-1394. doi: 10.1007/s00190-015-0822-4. URL http://link.springer.com/10.1007/s00190-015-0822-4.

Robinson, C. The crustal dichotomy of Mars. *Earth, Moon, and Planets*, (69):249–269, 1995. URL https://link.springer.com/article/10.1007/BF00643787.

Root, B., P. Novák, D. Dirkx, M. Kaban, W. van der Wal, and L. Vermeersen. On a spectral method for forward gravity field modelling. *Journal of Geodynamics*, 97:22–30, July 2016. ISSN 02643707. doi: 10.1016/j.jog.2016.02.008. URL https://linkinghub.elsevier.com/retrieve/pii/S0264370715300533.

Rossi, A. P. and S. v. Gasselt. Geology of Mars after the first 40 years of exploration. *Research in Astronomy and Astrophysics*, 10(7):621–652, July 2010. ISSN 1674-4527. doi: 10.1088/1674-4527/10/7/003. URL https://iopscience.iop.org/article/10.1088/1674-4527/10/7/003.

Schultz, R. A. and H. V. Frey. A new survey of multiring impact basins on Mars. *Journal of Geophysical Research*, 95(B9):14175, 1990. ISSN 0148-0227. doi: 10.1029/JB095iB09p14175. URL http://doi.wiley.com/10.1029/JB095iB09p14175.

Seidelmann, P. K., V. K. Abalakin, M. Bursa, M. E. Davies, C. D. Bergh, J. H. Lieske, J. Oberst, J. L. Simon, E. M. Standish, P. Stooke, and P. C. Thomas. Report of the IAU/IAG Working Group on Cartographic Coordinates and Rotational Elements of the Planets and Satellites: 2000. *Celestial Mechanics and Dynamical Astronomy*, 82:83–110, 2002.

Simons, M., S. C. Solomon, and B. H. Hager. Localization of gravity and topography: constraints on the tectonics and mantle dynamics of Venus. *Geophysical Journal International*, 131 (1):24–44, October 1997. ISSN 0956540X, 1365246X. doi: 10.1111/j.1365-246X.1997.tb00593.x. URL https://academic.oup.com/gji/article-lookup/doi/10.1111/j.1365-246X.1997.tb00593.x.

Smith, D. E., M. T. Zuber, and S. C. Solomon. The Global Topography of Mars and Implications for Surface Evolution_1999.pdf, 1999. URL https://science.sciencemag.org/content/284/5419/1495/tab-pdf.

Snyder, C. and V. Moroz. Spacecraft exploration of Mars. *Mars*, A93-27852(09-91):71–119, 1992.

Stähler, S. C., A. Khan, W. B. Banerdt, P. Lognonné, D. Giardini, S. Ceylan, M. Drilleau, A. C. Duran, R. F. Garcia, Q. Huang, D. Kim, V. Lekic, H. Samuel, M. Schimmel, N. Schmerr, D. Sollberger, E. Stutzmann, Z. Xu, D. Antonangeli, C. Charalambous, P. M. Davis, J. C. E. Irving, T. Kawamura, M. Knapmeyer, R. Maguire, A. G. Marusiak, M. P. Panning, C. Perrin, A.-C. Plesa, A. Rivoldini, C. Schmelzbach, G. Zenhäusern, E. Beucler, J. Clinton, N. Dahmen, M. van Driel, T. Gudkova, A. Horleston, W. T. Pike, M. Plasman, and S. E. Smrekar. Seismic detection of the martian core. *Science*, 373(6553):443–448, July 2021. ISSN 0036-8075, 1095-9203. doi: 10.1126/science.abi7730. URL https://www.sciencemag.org/lookup/doi/10.1126/science.abi7730.

Tanaka, K. L. Tanaka, K.L. (1986). The Stratigraphy of Mars.pdf, 1986.

Taylor, N. C., J. H. Johnson, R. A. Herd, and C. E. Regan. What can Olympus Mons tell us about the Martian lithosphere? *Journal of Volcanology and Geothermal Research*, 402:106981, September 2020. ISSN 03770273. doi: 10.1016/j.jvolgeores.2020.106981. URL https://linkinghub.elsevier.com/retrieve/pii/S0377027320302523.

Tenzer, R., E. Mehdi, and S. Jin. Martian sub-crustal stress from gravity and topographic models. *Earth and Planetary Science Letters*, page 9, 2015.

Thor, R. Mapping the thickness of the Martian elastic lithosphere using maximum likelihood estimation. Master's thesis, TU Delft, 2016. URL https://repository.tudelft.nl/islandora/object/uuid%3Aca2a860f-a78e-4517-a829-eb03a7254f45.

Turcotte, D. L., R. J. Willemann, W. F. Haxby, and J. Norberry. Role of membrane stresses in the support of planetary topography. *Journal of Geophysical Research*, 86(B5):3951, 1981. ISSN 0148-0227. doi: 10.1029/JB086iB05p03951. URL http://doi.wiley.com/10.1029/JB086iB05p03951.

Turcotte, D. L. and G. Schubert. *Geodynamics*. Cambridge University Press, Cambridge, United Kingdom, third edition edition, 2014. ISBN 978-1-107-00653-9 978-0-521-18623-0.

Van der Tang, Y. The origin of tharsis - a deep mantle gravity study. Master's thesis, TU Delft, 2021.

Van der Wal, W. *Contributions of Space Gravimetry to Postglacial Rebound Modeling with Different Rheologies*. PhD thesis, University of Calgary, 01 2009.

Wang, H., P. Wu, and W. van der Wal. Using postglacial sea level, crustal velocities and gravity-rate-of-change to constrain the influence of thermal effects on mantle lateral heterogeneities. *Journal of Geodynamics*, 46(3-5):104–117, October 2008. ISSN 02643707. doi: 10.1016/j.jog.2008.03.003. URL https://linkinghub.elsevier.com/retrieve/pii/S0264370708000227.

Watts, A. B. and J. D. P. Moore. Flexural Isostasy: Constraints From Gravity and Topography Power Spectra. *Journal of Geophysical Research*, page 14, 2017.

Watts, A. *Isostasy and Flexure of the Lithosphere*. Cambridge University Press, Cambridge, United Kingdom, 2001.

Wieczorek, M. Gravity and topography of the terrestrial planets. In *Treatise on Geophysics*, pages 153–193. Elsevier, 2015. ISBN 978-0-444-53803-1. doi: 10.1016/B978-0-444-53802-4.00169-X. URL https://linkinghub.elsevier.com/retrieve/pii/B978044453802400169X.

Wieczorek, M. A. and F. J. Simons. Localized spectral analysis on the sphere. *Geophysical Journal International*, 162(3):655–675, September 2005. ISSN 0956540X, 1365246X. doi: 10.1111/j.1365-246X.2005.02687.x. URL https://academic.oup.com/gji/article-lookup/doi/10.1111/j.1365-246X.2005.02687.x.

William, S. *The Planet Mars: A History of Observation and Discovery*. University of Arizona Press, 1996. ISBN 0-8165-1641-3 978-0-8165-1641-4.

Williams, J.-P., F. Nimmo, W. B. Moore, and D. A. Paige. The formation of Tharsis on Mars: What the line-of-sight gravity is telling us. *Journal of Geophysical Research*, 113(E10):E10011, October 2008. ISSN 0148-0227. doi: 10.1029/2007JE003050. URL http://doi.wiley.com/10.1029/2007JE003050.

Wu, P. Using commercial finite element packages for the study of earth deformations, sea levels and the state of stress. *Geophysical Journal International*, 158(2):401–408, August 2004. ISSN 0956540X, 1365246X. doi: 10.1111/j.1365-246X.2004.02338.x. URL https://academic.oup.com/gji/article-lookup/doi/10.1111/j.1365-246X.2004.02338.x.

Wu, S., P. Garcia, R. Jordan, F. Schafer, and B. Skiff. Topography of the shield volcano, Olympus Mons on Mars. *Nature*, 309(5967):432–435, May 1984. ISSN 0028-0836, 1476-4687. doi: 10.1038/309432a0. URL http://www.nature.com/articles/309432a0.

Yuen, D. A., M. Shigenori, K. Shun-ichiro, and F. Brian, editors. *Superplumes: beyond plate tectonics*. Springer, Dordrecht, 2007. ISBN 978-1-4020-5749-6. OCLC: 255428883.

Zhong, S. Effects of lithosphere on the long□wavelength gravity anomalies and their implications for the formation of the Tharsis rise on Mars. *Journal of Geophysical Research*, 107(E7 5054):13, 2002.